Low-Dimensional Modeling of Two-Phase Flow in Pipelines

A Dissertation

Presented to

the Faculty of the Department of Mechanical Engineering

University of Houston

In Partial Fulfillment

of the Requirements for the Degree

Doctor of Philosophy

in Mechanical Engineering

by

Amine Meziou

May 2017

Low-Dimensional Modeling of Two-Phase Flow in Pipelines

Amine Meziou

Approved:

Chair of the Committee
Matthew A. Franchek, Professor,
Mechanical Engineering

Committee Members:

Karolos Grigoriadis, Professor,
Mechanical Engineering

Gangbing Song, Professor,
Mechanical Engineering

Michael Nikolaou, Professor,
Chemical and Biomolecular Engineering

Robert Provence, Lecturer,
Electrical and Computer Engineering

Suresh K. Khator, Associate Dean,
Cullen College of Engineering

Pradeep Sharma, Professor and Chair,
Mechanical Engineering

Acknowledgments

I wish to express my sincere appreciation to those who have contributed to this dissertation and supported me in one way or the other during this amazing journey.

First and foremost, I would like to express my special gratitude to my supervisor, Dr. Mathew Franchek, for his continuous support, patience and guidance. His knowledge, and advice helped me completing my research and writing this thesis. I would like to express my sincere appreciation to my committee members, Dr. Karolos Grigoriadis, Dr. Gangbing Song, Dr. Michael Nikolaou, and Dr. Robert Provence, for accepting to serve as my committee members and for reviewing my research work.

I thank my fellow labmates for their support, stimulating discussions, and all the fun we have had in the past years. This work would not have been completed without your presence.

A special thanks to my mother Serra and my father Hedi for all the sacrifices they have made throughout my life. I would not be here if it not for you. To my beloved sisters Mariam and Mayssa, and my family in Houston, thank you for your love and support. To a special person in my life, my wife and best friend, Nada, you unconditional love and encouragement have been a constant source of strength and inspiration. Finally, thank you God for making this possible.

Low-Dimensional Modeling of Two-Phase Flow in Pipelines

An Abstract

of a

Dissertation

Presented to

the Faculty of the Department of Mechanical Engineering

University of Houston

In Partial Fulfillment

of the Requirements for the Degree

Doctor of Philosophy

in Mechanical Engineering

by

Amine Meziou

May 2017

Abstract

Multiphase flow in pipelines is an ubiquitous part of any oil and gas production system. Developing fast, yet accurate multiphase flow models having utility in system design, control design, and system health-monitoring is therefore an important engineering and scientific challenge, particularly when the pipelines are parts of a complex subsea architecture.

Presented in this dissertation are multi-physics reduced-order fluid and thermal models of one-dimensional transient two-phase flow in pipelines. The proposed fluid model is comprised of a steady state multiphase flow mechanistic model in series with a transient reduced-order single-phase flow model. The low-dimensional model parameters are realized by developing equivalent fluid properties (i.e., viscosity, density and bulk modulus) that are a function of the flow pattern, steady-state pressure gradient, and liquid holdup identified through the mechanistic model. The fluid model is then coupled with a two-phase flow heat transfer model via a multi-physics integration block used to update the fluid properties along the pipeline based on the predicted pressure and temperature conditions. The model ability to reproduce the dynamics of multiphase flow in pipes is first evaluated upon comparison to OLGA. The two models show a good agreement of the steady-state response and the period of oscillation indicating a similar estimation of the pipeline natural frequency. However, they present a discrepancy in the overshoot values and the settling time due to a difference in the calculated damping ratio. Both models are then compared to transient two-phase flow data collected at the National University of Singapore flow loop. It is concluded that the low-dimensional model is

characterized by a superior overall performance when compared to OLGA. The developed model accuracy improves when considering a higher order but is associated with a higher simulation time. The established multi-physics models are used for the design, modeling, simulation, and optimization of multiple-wells subsea architectures with a High Integrity Pressure Protection System (HIPPS) as an alternative to reduce the subsea capital expenditure (CAPEX).

The utility of the developed low-dimensional models is the reduced computational burden of estimating transient multiphase flow in pipelines, thereby enabling real-time estimation of pressure, temperature, and flow rate.

Table of Contents

List of Figures

List of Tables

Nomenclature

A = Pipe Cross Section Area

C = Pipe Capacitance

C_p = Heat Capacity

c = Speed of sound in the fluid

D = Pipe diameter

f = Darcy friction factor

GVF = Gas Volume Fraction

G_Z = Graetz number

g = Acceleration due to gravity

h = Convection heat transfer coefficient

I = Pipe Inertance

K = Thermal conductivity

L = Pipe length

Nu = Nusselt number

P = Pressure

Pr = Prandt Number

Q = Flow rate

R = Pipe resistance

r = Pipe internal radius

Re = Reynolds number

s = Laplace operator

V = Velocity

Z_c = Characteristic impedance

α = Ratio of the length of the gas bubble and liquid film

β = Bulk modulus

μ = Dynamic viscosity

γ = Specific heat ratio

Γ = Propagation operator

ε = Pipe roughness

ξ = Damping ratio

ν = Kinematic viscosity

ρ = Density

ω_n = Natural frequency

Subscripts

eq = Equivalent fluid

G = Vapor phase

in = Pipeline inlet

L = Liquid phase

Lam = Laminar

out = Pipeline outlet

ss = Steady-state condition

Tur = Turbulent

0 = Reference condition

Chapter 1

Introduction

Two-phase flow refers to the simultaneous flow of two phases or components (i.e., gas, liquid, and/or solid). This category of flow has a wide range of applications. Two-phase flow is omnipresent in the human environment ranging from rain, snow, fog, wave breaking, tide, particle dispersion or sediment transport. It is considered as a fundamental element in understanding the interactions at the interface between the earth surface and the atmosphere [1]. Two-phase flow is also widely studied for medical and biological applications including blood flow [2, 3], diseases propagation [4] and drug delivery systems [5]. It constitutes a crucial part of the automotive, aerospace and power generation industries where the efficiency of the fuel injection systems [6], engines combustion [7], exhaust systems [8] and turbines [9] relies heavily on multiphase flow phenomena. In addition, two-phase flows are a ubiquitous part of the chemical, processing and petroleum industry, observed in multiple areas such as oil and gas wells [10], pipelines and chemical reactors [11].

In most of these applications, gathering experimental or field data is often very difficult, as some of the processes are carried out at high pressure and temperature conditions or involve the use of hazardous substances. Multiphase flow metering may even be impossible due to technology, safety or cost limitations. Furthermore, the installation of measuring devices can disturb flow, reducing substantially the components efficiency.

Understanding the mechanics that govern this type of flow and developing reliable computer models to simulate its behavior is therefore a key engineering and scientific challenge.

Depending on the physical states of the constituent components, two-phase flows can be classified into gas/solids flows, liquid/solids flows or gas/liquid flows. Similarly, using the topology of the phases interface, two-phase flows can be categorized into: (i) dispersed flows, where particles, droplets or bubbles are distributed into a continuous phase; (ii) separated flows, consisting of two continuous phases; and (iii) transitional or intermediate flows.

Due to the two-phase flows large scope of applications and the specificities of each one of them, one cannot develop a unified modeling approach tailored to the required degree of accuracy or the available computational power for all industries. Although extendible for different other applications, the scope of this study is to develop low-dimensional transient two-phase gas-liquid flow models for oil and gas (O&G) applications.

At the heart of any oil and gas drilling, production or transportation system, pipelines are responsible of carrying out the production fluids from the wells into a hosting facility and are considered as the O&G industry "venous system".

Multiphase flow in pipes has drawn a particular interest in the O&G industry for decades. Extensive efforts have been focused at gaining an understanding of the phenomena that drive this complicated flow. Specifically focusing on oil and gas drilling/production applications, commercial codes were developed including Pipesim, OLGA and LedaFlow. In general, commercially available codes are built on simplified

physics-based models calibrated using empirical correlations, in-field data and smoothing techniques. These computational codes set the industry gold standard for predicting multiphase flow dynamics. Despite the advancements of multiphase flow, there is an important need to develop transient multiphase flow models that are built mostly on multi-physics principles.

In the remainder of this chapter, the background leading to the development of the proposed two-phase flow models is discussed. Early work on single-phase and two-phase steady-state and transient flow in pipelines are described. Next, the crucial subsea engineering challenges motivating the elaboration of the proposed reduced-order models are outlined before concluding with the present research objectives and the thesis outline.

1.1. Background

1.1.1. Early work on Single-Phase Flow Pipeline Dynamic Modeling

The interest in the dynamic modeling of flow in pipelines started since the early nineteenth century, when Young [12] established the speed of a pressure-wave in an incompressible liquid through an elastic tube. In 1878, Korteweg [13] derived the fluid velocity field in a pipeline as a function of the speed of sound. This work was extended by Lamb [14] to include the effect of wall elasticity. Those developments provided an insight on transient single-phase flow by the means of one-dimensional lossless wave models. However, second-order effects such as viscosity effects, heat transfer losses (known as dissipation effects) and complex boundary conditions were neglected.

Modeling transient single-phase flow in pipelines requires solving the Navier-Stokes equations (i.e., continuity, momentum, and energy equations). To date, closed-form solutions for those three-dimensional partial differential equations (PDE) are still to

be derived. As an alternative, paralleling electrical and mechanical systems, the lumped-parameter modeling technique was used to relate the pressure and flow at the pipeline inlet and outlet [15]. In this method, the three physical parameters characterising the flow in the pipeline, namely the resistance, inertance, and capacitance are assumed to be located in one or more discrete locations along the pipeline (Figure 1.1). This results in a system of linear ordinary differential equations.

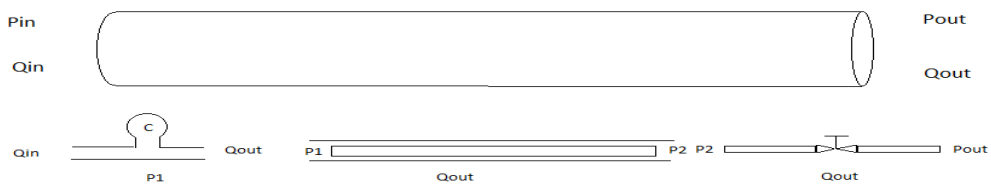

Figure 1.1: Lumped Parameter Model Diagram

The governing equations are as follows:

Fluid Capacitance: $$Q_{in} - Q_{out} = C\dot{P}_{in}, \tag{1.1}$$

Fluid Inertance: $$P_{in} - P_2 = I\dot{Q}_{out}, \ and \tag{1.2}$$

Fluid Resistance $$P_2 - P_{out} = RQ_{out}, \tag{1.3}$$

where

$$C = \frac{AL}{\beta}, \tag{1.4}$$

$$I = \frac{\rho L}{A}, \tag{1.5}$$

$$c = \sqrt{\frac{\beta}{\rho_0}}, \; and \tag{1.6}$$

$$R = \frac{f \rho Q L}{2DA^2}. \tag{1.7}$$

The Darcy friction factor f is calculated for both laminar and turbulent flow conditions. Solving the above equations in the Laplace domain gives

$$Q_{out} = \frac{1}{CIs^2 + RCs + 1} Q_{in} + \frac{Cs}{CIs^2 + RCs + 1} P_{out} \; and \tag{1.8}$$

$$P_{in} = \frac{1}{CIs^2 + RCs + 1} P_{out} - \frac{Is + R}{CIs^2 + RCs + 1} Q_{in}. \tag{1.9}$$

Note that the resistance, inertance and capacitance can be arranged into 6 different configurations. Summarized in Table 1.1 are the different inputs, outputs and models corresponding to each configuration.

The lumped parameter modeling approach of flow in pipelines are used to study the transient behavior of single-phase flow in both frequency and time domains. In addition, this method provides the effect of the fluid and pipe characteristics on the pipeline's dynamic response. However, as second-order systems, the established transfer functions in Table 1.1 are not able to describe the higher-order dynamics.

Table 1.1: Lumped Parameter Models Configurations

Capacitance/Resistance/Inertance Capacitance/Inertance/Resistance	$\begin{bmatrix} Q_{out} \\ P_{in} \end{bmatrix} = \begin{bmatrix} \frac{1}{CIs^2+RCs+1} & \frac{Cs}{CIs^2+RCs+1} \\ \frac{Cs}{CIs^2+RCs+1} & \frac{1}{CIs^2+RCs+1} \end{bmatrix} \begin{bmatrix} Q_{in} \\ P_{out} \end{bmatrix}$
Resistance/Inertance/Capacitance Inertance/Resistance/Capacitance	$\begin{bmatrix} P_{out} \\ Q_{in} \end{bmatrix} = \begin{bmatrix} \frac{1}{CIs^2+RCs+1} & -\frac{Is+R}{CIs^2+RCs+1} \\ \frac{Cs}{CIs^2+RCs+1} & \frac{1}{CIs^2+RCs+1} \end{bmatrix} \begin{bmatrix} P_{in} \\ Q_{out} \end{bmatrix}$
Inertance/Capacitance/Resistance	$\begin{bmatrix} Q_{out} \\ Q_{in} \end{bmatrix} = \begin{bmatrix} \frac{1}{CIRs^2+Is+R} & -\frac{ICs^2+1}{CIRs^2+Is+R} \\ \frac{CRs+1}{CIRs^2+Is+R} & -\frac{1}{CIRs^2+Is+R} \end{bmatrix} \begin{bmatrix} P_{in} \\ P_{out} \end{bmatrix}$
Resistance/Inertance/Capacitance	$\begin{bmatrix} P_{out} \\ P_{in} \end{bmatrix} = \begin{bmatrix} \frac{1}{CIRs^2+Is+R} & -\frac{CRs+1}{CIRs^2+Is+R} \\ \frac{ICs^2+1}{CIRs^2+Is+R} & -\frac{1}{CIRs^2+Is+R} \end{bmatrix} \begin{bmatrix} Q_{in} \\ Q_{out} \end{bmatrix}$

In reality, the fluid resistance, inertance and capacitance are distributed along the pipeline and not just located at discrete points as suggested in Figure 1.1. To cope with the limitations of one-dimensional lossless wave models and the lumped parameter model, exact solutions of the Navier-Stokes equations for laminar flow were derived for rigid circular pipelines by Iberall [16]. The models in [16] included viscous friction and heat transfer effects. This development was then extended by Brown [17], resulting in the dissipative distributed-parameter model. Based on the work of Oldenburger [18] , Hsue and Hullender [19] performed a modal approximation of the hyperbolic transfer functions constituting the dissipative distributed-parameter model.

The resulting reduced-order models are more suitable for real-time applications, such as pressure and flow rate monitoring, analysis led design, controller adaptation and diagnostics. Furthermore, this approach is relevant when the pipelines are used as a component of a complex system (hydraulic control systems, multiple-wells subsea architectures, etc.). In addition to pipelines, those systems include other equipment like valves, regulators and actuators. Hence, using the reduced-order methodology, the interactions between the different components can be characterized and the overall system behavior can be simulated and analyzed more efficiently.

A detailed description of the derivation of the dissipative distributed parameter model, its approximation and extension to turbulent flow conditions will be discussed in Chapter 2 of this dissertation.

1.1.2. State of the Art on Steady-State Two-Phase Flow Modeling

Distinct approaches have been used to model steady state two-phase flow systems. These include: (i) Homogeneous models; where it is assumed that the two phases are travelling at the same velocity and the flow is reduced to a single-phase flow [20-24], (ii) Separated flow models; where the two phases are assumed to be traveling at different velocities which affects the overall conservation equations [25-33], (iii) Multi-fluid models; where interactions between the two-phases are described in separate conservation equations written for each phase [34-38], (iv) Drift flux models; where the flow is described in terms of a distribution parameter and an averaged local velocity difference between the two phases [39-44], and (v) Computational fluid dynamic (CFD) models; where in contrast to the aforementioned models, two or three dimensions are usually involved in an attempt to describe the full flow field.

The simplest approach for two-phase flow modeling is the homogeneous flow model wherein the relative motion between the two phases can be neglected and the flow behaves as single-phase with properties defined as weighted averages of the properties of the individual phases. The conservation laws are hence solved in their homogeneous form, which may be found in [22]. This type of models is known to be inadequate for most two-phase flows except those in which the two phases mix well, or when the mixture velocity is very high such as bubbly and misty flows.

A second approach for two-phase flow modeling is the separated flow models which require more complexity, and in which the phases are allowed to slip relatively to each other. Aiming at solving the overall conservation equations, correlations were developed to determine the shear stress at the two phases contact with the pipe wall. This method constitutes the basis of the Lockhart-Martinelli [26] correlations. These correlations were extended to the turbulent flow of steam-water mixtures by Martinelli and Nelson [25]. Levy [30], as well as Gopalakrishman and Schrock [27] developed an analytical momentum exchange model aiming at extending the range of coverage of the Martinelli closure laws, which turns to be not overly accurate. Empirical correlations, which attempt to cover all fluids and different flow directions, were also developed in [29]. The major limitation of this type of models remains their empirical nature and their incapability of dealing, in details, with the two-phase flow structure.

As more sophisticated models, the multi-fluid models do not need two-phase multipliers, and analogies between single and two-phase flows need not to be invoked. This type of models differs from separated flow in that separate conservation equations are solved for the liquid and vapor phases. Multi-fluid model equations may be found in

[34-37]. The accuracy of the two-phase models closely depends on the information about flow regimes, as well as the level of accuracy of the models used for mass, momentum, and energy exchange.

Another class of models that has been widely used is the drift flux model. Originally derived by Zuber and Findlay [39], this model uses flow parameters to determine the relative motion between the phases. Other studies have added to its development, particularly Wallis [41], where a comprehensive treatment of the basic theory can be found. Multiple works established correlations for void fraction estimation that can be applied to a wide range of flow conditions [42-44].

Finally, CFD models not only represent an alternative to the costly experimental work, but also help understand and predict multiphase flow phenomena. Nonetheless, the complexity of the physics and the nonlinear nature of the flow equations make this type of models unlikely to replace all experimental work at least in the foreseeable future.

As an alternative to the modeling approaches presented above, mechanistic models prove to be more accurate in predicting the geometric and fluid property variations. Despite being based on fundamental laws, mechanistic models still need closure relationships based on observations. The central step in a mathematical mechanistic approach is to determine the flow regime. Transitions between the different regimes were first developed by Taitel and Dukler [45]. Since then, multiple efforts have been directed towards the development of analytical procedures to predict the flow pattern and transition boundaries. However, these efforts are either incomplete in the sense they only consider flow pattern determination [46], or are only applicable to a limited range of pipe inclinations [47, 48]. Petalas and Aziz [49] proposed a model that

overcomes these limitations. Additional investigations of specific flow regimes allowed refining this model in [50]. The flow pattern, liquid holdup and steady-state pressure drop predicted by the Petalas and Aziz mechanistic model were validated against the Stanford University Multiphase Flow Database in [50] and showed the best general agreement among the other available two-phase flow steady-state models.

1.1.3. State of the Art on Transient Two-Phase Flow Modeling

Beyond steady state flow conditions, transient two-phase flow models were originally developed within the nuclear industry to simulate transient flow induced by the Loss Of Coolant Accidents (LOCA), characterized by very high heat flux through the pipeline wall and rapid transient phenomena.

Moore and Rettig [51] developed RELAP4, a computer code that describes the behavior of water-cooled nuclear reactors subject to a LOCA event. In this development, a homogeneous equilibrium method was used to perform a transient thermal-hydraulic analysis. Aiming at extending this work, Fischer [52] introduced the effect of the slip between the two phases. Lyczkowski et al. [53] and Solbrig and Hughes [54] used a more complex approach where separate continuity, momentum, and energy equations for each phase were considered. The stability of transient one-dimensional two-phase flows were then analyzed and classified using the method of characteristics.

The study of transient two-phase flow phenomena in the oil and gas industry started in the late seventies using the techniques adopted by the nuclear industry. Cunliffe [55] characterized the transient effect of an increase of the outlet gas flow rate on the inlet liquid flow rate based on the liquid holdup at steady state. This method cannot be considered as a proper transient analysis and always results in a low estimation of the

liquid flow rate. Modisette and Whaley [56] used the two-fluid model while considering different possible flow patterns. However, the accuracy of their model in the prediction of the liquid holdup and the pressure drop was not proven. Bendiksen et al. [57-59] used the two-fluid model with an additional momentum equation for the droplets and one energy equation for the two-phase mixture to simulate multiphase flow phenomena. This work is considered as the basis behind the multiphase flow transient model of the flow assurance software OLGA, the market leader among all commercial solutions. The LedaFlow model, another commercial two-phase flow transient package, is a multidimensional multi-fluid model. It is based on solving nine continuity equations, three momentum equations and three energy equations. Black et al. [60] developed the PLAC code based also on the two-fluid model. Some other computer codes have used a drift flux modeling approach to simulate transient two-phase flows like TACITE [61], TRAFLOW, and FlowManager pipe simulator.

Whether based on the two-fluid or drift flux model, the simulators developed previously and considered nowadays as the main and standard tool for modeling transient two-phase flow are based on the full set of mass, momentum and energy conservation equations for each phase. This approach is certainly relevant for the nuclear industry, where very fast transients occur. However, the oil and gas industry is usually characterized by slow transient flow conditions. Hence, solving numerically the Navier-Stokes equations is not compulsory and can be very time consuming, especially when modeling complex systems, which requires thousands of simulations. Some previous works tried to make different assumptions to simplify the problem. This approach was adopted by Taitel et al. [62] where a quasi-steady-state gas flow and a local equilibrium

momentum balance for an incompressible liquid were assumed. The resulting model was described by a single PDE. This modeling was further investigated by Minami and Shoham [63] and was found to be suitable only for a limited range of conditions. Applying this type of models without being aware of their limitations can lead to inaccurate predictions. This task can be more critical when the pipeline is part of a complex and challenging system such as oil and gas subsea architectures, where a fast, yet accurate estimation of multiphase flow phenomena is necessary.

1.2. Subsea Engineering Challenges

Offshore petroleum production is an increasingly important source of energy as well as an important driver of the global economy. Rising global demand for energy requires the production of known massive reserves located in ultra deepwater (defined as depths greater than 3,500 feet and extending to depths of over 10,000 feet). However producing ultra deepwater oil and gas presents significant engineering challenges that are completely different from regular offshore production (up to 2,000 ft). Many of these challenges are rooted in the unique and particularly harsh nature of the underwater environment: the water temperature is typically near freezing, the pressure is hundreds of times greater than at sea level (depending on the operation's depth). Many engineering challenges also come from the reservoirs, which are at high temperatures and pressures. In addition, cost effective ultra deepwater production requires that most subsea systems service multiple wells (Figure 1.2). The multi-well productions are combined through a subsea manifold that feeds a riser, which in turn carries the production to the water's surface. In many cases deepwater subsea fields have multiple risers since the reservoir wells can be spread within a 10-mile radius area.

Additional complexities arise when bringing the oil and gas to the surface. Despite the high reservoir pressures, artificial lift systems (electric motors coupled to pumps) are needed to overcome the pressure head associated with deepwater production.

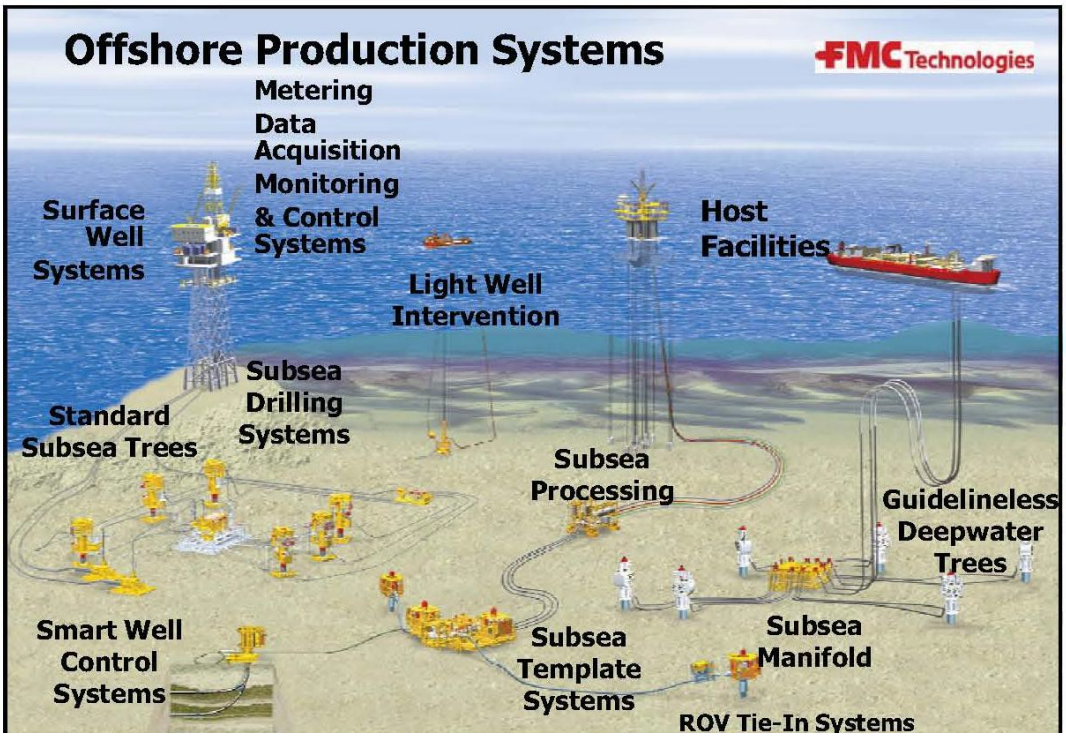

Figure 1.2: Complex Subsea System Illustration [64]

Furthermore, producing subsea reserves brings critical flow assurance challenges. This term refers to ensuring a continuous and economical flow of the hydrocarbons from the wells into the hosting facility. The flow can be disturbed by different events (Figure 1.3) such as:

- Hydrate: formed by gas molecules getting into hydrogen-bonded water cages resulting in the blockage of the production pipeline;
- Slugging: caused by the fast flow of the gas phase over a slower flowing liquid phase (hydrodynamic slugging), or by the variation in the pipe inclination (terrain slugging);

- Wax: consists of hydrocarbons depositions inducing both a restricted flow caused by a reduced inner diameter in pipelines and an increased wall roughness, and a dramatic increase in the oil viscosity;
- Erosion: caused by the flow of hydrocarbons with entrained particles at a very high speed; and
- Water hammer: consists of a pressure surge generated when a moving fluid is forced to stop or change direction suddenly.

Modeling transient multiphase flow in pipelines is crucial in predicting; mitigating; controlling or preventing all the phenomena discussed previously. It is, hence, at the basis of all flow assurance activities.

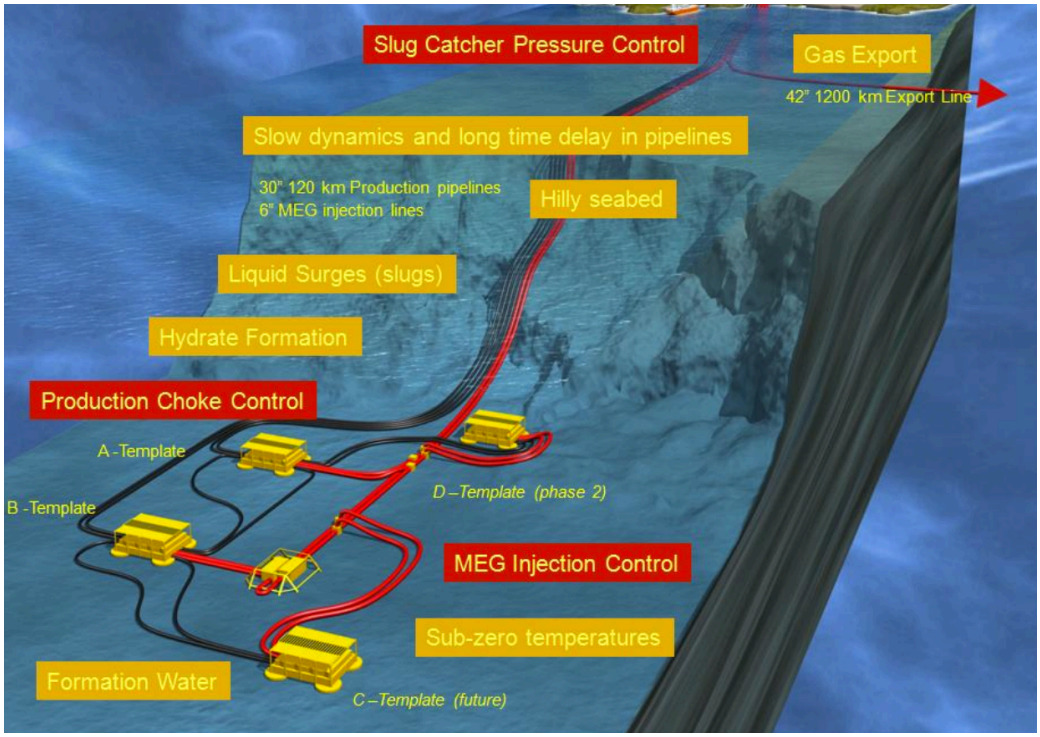

Figure 1.3: Examples of Subsea Production System Flow Assurance Challenges [64]

Collectively, subsea systems are complex system-of-systems spanning electrical, mechanical, thermal, fluid and chemical energy domains. By focusing on proposing a physics-based low-dimensional approach to modeling two-phase flow systems, the present work seeks a unifying systems theory enabling to overcome the numerous subsea engineering challenges.

1.3. Research Objectives and Significance

The objectives of the proposed research are centered on the development and integration of multi-domain reduced order models necessary for subsea systems engineering design.

At the center of any drilling or production operation, pipelines constitute a fundamental component of every subsea architecture. This work focuses, therefore, on establishing multiphase flow fluid and thermal pipeline dynamic models. The proposed Low-D pipeline multiphase flow models are derived based on process physics for flow under laminar and turbulent conditions. They are realized by coupling a mechanistic two-phase flow steady-state approach with the distributed-parameter single-phase flow transient model through the derivation of equivalent fluid properties. These Low-D fluid models are integrated with Low-D heat transfer pipeline models thus capturing the interdependence between heat transfer and fluid flow in a form that has systems design utility.

Aiming at validating the suggested modeling methodology, every constituent of the developed multiphysics model will be validated against an independent experimental dataset. The overall model performance is then accessed by comparing its prediction to commercial multiphase flow dynamic models and transient experimental results. The

obtained coupled Low-D models produce significantly more accurate multiphase flow and heat transfer predictions over traditional lumped parameter models.

The significance of this research comes from proposing a fast, yet accurate systems-based alternative to the available commercial multiphase flow packages. The newly developed low-D models can be useful for a wide range of engineering applications including hydraulic systems design and simulation, flow assurance, subsea architectures design and optimization and real-time condition monitoring.

1.4. Thesis Outline

Following is the outline of the thesis. In Chapter 2, the modeling procedure of the proposed transient two-phase flow low-dimensional model is outlined. Next, the derivation, modal approximation and extension to turbulent flow conditions of the dissipative distributed-parameter model are described. Then the mechanistic steady-state two-phase model, used to predict the two-phase flow pattern, liquid holdup and pressure drop is discussed and validated against the Stanford University multiphase flow database. These resulting estimates are used to develop the equivalent fluid properties, namely altering the fluid density, viscosity and bulk modulus. Finally, frequency and time-domain analysis are performed to evaluate the effect of the Gas Volume Fraction (GVF) level on the pipeline's dynamic response.

In chapter 3, the low-dimensional model described in Chapter 1 is integrated with a physics-based two-phase flow thermal model to account for the effect of heat transfer on the pipeline's transient behavior, resulting in a multiphysics hydraulic and thermal model. The thermal models used in this development are validated against an independent experimental dataset. At the end of this chapter, a sensitivity analysis is

presented to establish the causal effects of different fluid properties and boundary conditions on the flow within the pipeline.

The objective of Chapter 4 is to validate the proposed two-phase flow transient model. First, the model predictions are compared to OLGA simulations for different GVF levels. Both models are then compared to a transient experimental dataset gathered using the National University of Singapore multiphase flow loop. The experimental facility, instrumentation and data acquisition system used to collect the data are described before accessing how well the low-dimensional and the OLGA model capture the two-phase flow dynamic behavior at both low and high gas contents.

In Chapter 5, the resulting multiphysics models are used in a systems approach to design, simulate and optimize a subsea architecture with a High Integrity Pressure Protection System (HIPPS).

Finally, in Chapter 6, the main findings and conclusions are summarized. Various outstanding issues are identified and suggestions for future research are given.

Chapter 2

Two-Phase Flow Low-Dimensional Transient Modeling

2.1. Introduction

Offering a systems-approach alternative to the commercial transient two-phase flow models described in Chapter 1, this chapter focuses on the development of reduced-order low-dimensional fluid models of transient two-phase flow in pipelines.

The proposed modeling process is based on three major steps (Figure 2.1). First, the mechanistic steady-state model in [50] is used to determine the flow pattern, the steady-state liquid holdup and pressure drop (step 1). In step 2, these resulting estimates are used to develop equivalent single-phase fluid parameters, namely altering the fluid density, viscosity and bulk modulus as a function of the gas void fraction (GVF). The derived equivalent fluid properties are finally used as model parameters for the single-phase dissipative distributed-parameter model in [17] (step 3). Summarized in Figure 2.1 are the modeling steps.

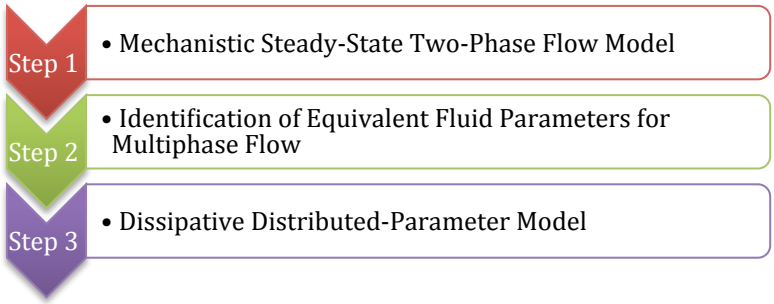

Figure 2.1: Transient Two-Phase Flow Modeling Procedure

In this Chapter, the limiting case of transient single-phase flow is first studied. The dissipative distributed parameter model derivation, approximation and extension to turbulent flow conditions are detailed. The mechanistic steady-state two-phase flow model and the identification of the equivalent fluid properties are then presented, leading to the development of the proposed low-dimensional transient two-phase flow model. Lastly, frequency and time domain analysis are performed to discuss the model's dynamic response.

2.2. Dissipative Distributed Parameter Model for Transient Single-Phase Flow

Since the early nineteenth century, considerable effort has been devoted to characterize the dynamics of the flow in pipelines [12, 16, 65]. Solutions of transient fluid flows can be obtained by solving the Navier-Stokes equations. However, closed-form solutions of these coupled partial differential equations are not known. To overcome this challenge some assumptions are considered to reduce the complexity of the problem. This section aims at presenting a simplified approach to model the transient nature of single-phase flow assuming laminar flow conditions, which will then be extended to the turbulent flow case.

2.2.1. Model Derivation

The dissipative distributed parameter model, also referred in the literature as "the exact model" is derived from the Navier-Stokes equations and the equation of state assuming a non-turbulent mean flow, Mach number much less than unity, a high length to diameter ratio, and a low normalized density variation. The governing partial differential equations for confined fluid flow are as follows:

Momentum Equation: $$\bar{\rho}\frac{\partial u}{\partial t} = -\frac{\partial P}{\partial x} + \mu\left(\frac{\partial^2 u}{\partial r^2} + \frac{1}{r}\frac{\partial u}{\partial r}\right), \tag{2.1}$$

Continuity Equation: $$\frac{\partial \rho}{\partial t} + \bar{\rho}\left(\frac{\partial u}{\partial x} + \frac{\partial v}{\partial r} + \frac{v}{r}\right) = 0, \tag{2.2}$$

Energy Equation: $$\frac{\partial T}{\partial t} + \frac{\bar{T}}{\bar{\rho}}(\gamma - 1)\frac{\partial \rho}{\partial t} = \alpha_0\left(\frac{\partial^2 T}{\partial r^2} + \frac{1}{r}\frac{\partial T}{\partial r}\right), \tag{2.3}$$

Liquid State Equation: $$\frac{\partial \rho}{\bar{\rho}} = \frac{\partial P}{\beta_e}, \textit{ and} \tag{2.4}$$

Gas State Equation: $$\frac{\partial \rho}{\bar{\rho}} = \frac{\partial P}{\bar{P}} - \frac{\partial T}{\bar{T}}. \tag{2.5}$$

As mentioned in Chapter 1, the fluid inertance, resistance and capacitance are not located in discrete locations but rather distributed along the pipeline (Figure 2.2). *Z*, the series impedance per unit length represents the inertial and resistive effects of the fluid volumetric flow on the pressure gradient (resistance and inertance). *Y*, the shunt admittance per unit length accounts for the compressibility effects of the fluid and pipe (capacitance).

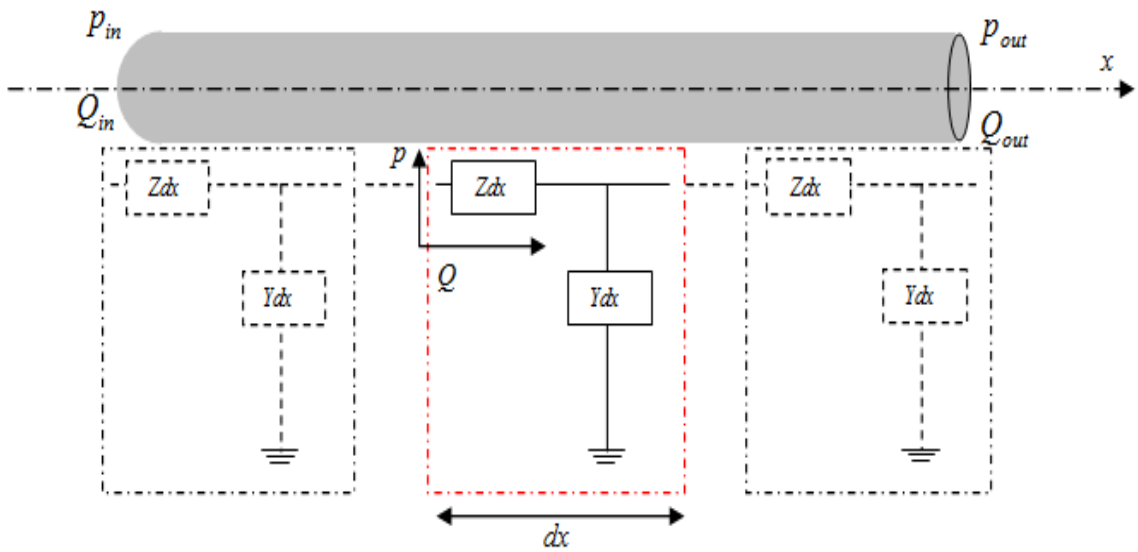

Figure 2.2: Pipeline Distributed Parameter Representation

The two parameters are related to the pressure and flowrate in the Laplace domain by the following system of equations

$$\begin{cases} Z(s)Q(x,s) = -\dfrac{\partial P(x,s)}{\partial x} \\ Y(s)P(x,s) = -\dfrac{\partial Q(x,s)}{\partial x} \end{cases}. \tag{2.6}$$

The solution of this system in (2.1) is given by

$$\begin{cases} P(x,s) = \dfrac{1}{2}\left[\left(P_{in} - Q_{in}\sqrt{\dfrac{Z}{Y}}\right)e^{\sqrt{ZY}x} + \left(P_{in} + Q_{in}\sqrt{\dfrac{Z}{Y}}\right)e^{-\sqrt{ZY}x}\right] \\ Q(x,s) = \dfrac{1}{2}\left[\left(Q_{in} - P_{in}\sqrt{\dfrac{Y}{Z}}\right)e^{\sqrt{ZY}x} + \left(Q_{in} + P_{in}\sqrt{\dfrac{Y}{Z}}\right)e^{-\sqrt{ZY}x}\right] \end{cases}. \tag{2.7}$$

The system in (2.2) can be rearranged as

$$\begin{cases} P(x,s) = \left[P_{in} \dfrac{\overbrace{\left(e^{\sqrt{ZY}x} + e^{-\sqrt{ZY}x}\right)}^{\cosh\left(\sqrt{ZY}x\right)}}{2} - Q_{in}\sqrt{\dfrac{Z}{Y}} \dfrac{\overbrace{\left(e^{\sqrt{ZY}x} - e^{-\sqrt{ZY}x}\right)}^{\sinh\left(\sqrt{ZY}x\right)}}{2} \right] \\ Q(x,s) = \left[-P_{in}\sqrt{\dfrac{Y}{Z}} \underbrace{\dfrac{\left(e^{\sqrt{ZY}x} - e^{-\sqrt{ZY}x}\right)}{2}}_{\sinh\left(\sqrt{ZY}x\right)} + Q_{in} \underbrace{\dfrac{\left(e^{\sqrt{ZY}x} + e^{-\sqrt{ZY}x}\right)}{2}}_{\cosh\left(\sqrt{ZY}x\right)} \right] \end{cases} . \tag{2.8}$$

Hence, The distributed parameter model of a rigid, one dimensional, circular pipeline may be represented in the following two-port matrix

$$\begin{bmatrix} P(x,s) \\ Q(x,s) \end{bmatrix} = \begin{bmatrix} \cosh(\Gamma) & -Z_c \sinh(\Gamma) \\ -\dfrac{\sinh(\Gamma)}{Z_c} & \cosh(\Gamma) \end{bmatrix} \begin{bmatrix} P_{in} \\ Q_{in} \end{bmatrix}, \tag{2.9}$$

where

$$\Gamma = \sqrt{ZY}x \text{ and} \tag{2.10}$$

$$Z_c = \sqrt{\frac{Z}{Y}} . \tag{2.11}$$

The propagation operator Γ characterizes the transmission time delays, attenuation and dissipation. The characteristic impedance Z_c represents the internal impedance of the transmission line.

Four different causal matrix representations of the dissipative distributed parameter model given by (2.9) are possible. Those representations differ from each other with respect to the model inputs and outputs and are given as follows:

$$\begin{bmatrix} P_{out} \\ Q_{in} \end{bmatrix} = \begin{bmatrix} \dfrac{1}{\cosh(\Gamma)} & -Z_c \dfrac{\sinh(\Gamma)}{\cosh(\Gamma)} \\ \dfrac{\sinh(\Gamma)}{Z_c \cosh(\Gamma)} & \dfrac{1}{\cosh(\Gamma)} \end{bmatrix} \begin{bmatrix} P_{in} \\ Q_{out} \end{bmatrix}, \tag{2.12}$$

$$\begin{bmatrix} P_{in} \\ Q_{out} \end{bmatrix} = \begin{bmatrix} \dfrac{1}{\cosh(\Gamma)} & Z_c \dfrac{\sinh(\Gamma)}{\cosh(\Gamma)} \\ -\dfrac{\sinh(\Gamma)}{Z_c \cosh(\Gamma)} & \dfrac{1}{\cosh(\Gamma)} \end{bmatrix} \begin{bmatrix} P_{out} \\ Q_{in} \end{bmatrix}, \tag{2.13}$$

$$\begin{bmatrix} P_{in} \\ P_{out} \end{bmatrix} = \begin{bmatrix} Z_c \dfrac{\cosh(\Gamma)}{\sinh(\Gamma)} & -Z_c \dfrac{1}{\sinh(\Gamma)} \\ -Z_c \dfrac{1}{\sinh(\Gamma)} & -Z_c \dfrac{\cosh(\Gamma)}{\sinh(\Gamma)} \end{bmatrix} \begin{bmatrix} Q_{in} \\ Q_{out} \end{bmatrix}, \text{ and} \tag{2.14}$$

$$\begin{bmatrix} Q_{in} \\ Q_{out} \end{bmatrix} = \begin{bmatrix} \dfrac{\cosh(\Gamma)}{Z_c \sinh(\Gamma)} & -\dfrac{1}{Z_c \sinh(\Gamma)} \\ \dfrac{1}{Z_c \sinh(\Gamma)} & -\dfrac{\cosh(\Gamma)}{Z_c \sinh(\Gamma)} \end{bmatrix} \begin{bmatrix} Q_{in} \\ Q_{out} \end{bmatrix}. \tag{2.15}$$

The dissipative distributed parameter model coefficients are given by:

$$\Gamma(\bar{s}) = D_n \bar{s} \left(\frac{1 + (\gamma - 1) B_\sigma}{1 - B} \right)^{\frac{1}{2}}, \tag{2.16}$$

$$Z_c(\bar{s}) = \frac{Z_0}{\sqrt{1 - B}\sqrt{1 - B_\sigma}}, \tag{2.17}$$

$$D_n = \frac{\upsilon L}{cr^2}, \tag{2.18}$$

$$\bar{s} = \frac{r^2}{\upsilon} s, \tag{2.19}$$

$$B_\sigma = \frac{2J_1(j\sqrt{\sigma \bar{s}})}{j\sqrt{\sigma \bar{s}} J_0(j\sqrt{\sigma \bar{s}})}, \tag{2.20}$$

$$B = \frac{2J_1(j\sqrt{\bar{s}})}{j\sqrt{\bar{s}} J_0(j\sqrt{\bar{s}})}, \textit{ and} \tag{2.21}$$

$$Z_0 = \frac{\rho_0 c}{\pi r^2}, \tag{2.22}$$

where J_0 and J_1 are the zero and first-order Bessel functions of the first kind; v is the kinematic viscosity; c is the speed of sound in the fluid; σ is the Prandtl number and γ is the specific heat ratio.

The formulation of the dissipative distributed-parameter model is detailed in [17] (Appendix A, B and C). The dissipative model is applicable for arbitrary boundary conditions and its accuracy has been experimentally validated for different flow conditions [66-68].

Using the dissipative model in the form given by (2.12)-(2.15), a frequency domain analysis can be performed. However, for time domain analysis or controller design purposes, a modal approximation of the fluid line dynamic model should be performed. Giving the different possible causal matrix representations, there are seven constitutive transfer functions. In this dissertation, only the three transfer functions used

in (1.12) and (2.14) are approximated. The proposed approach can be easily extended to approximate the four other transfer functions presented in (2.14) and (2.15).

2.2.2. Modal Approximation

Oldenburger [18] introduced infinite product series representations for $\cosh(\Gamma)$ as

$$\cosh(\Gamma) = \prod_{i=1}^{\infty} \left\{ 1 + \frac{\Gamma^2}{\pi^2 (i - \frac{1}{2})^2} \right\}. \tag{2.23}$$

The Bessel function ratios B_σ and B in (2.20) and (2.20) should then be expressed in the form of product series.

$$B_\sigma = \prod_{i=1}^{\infty} \left\{ \frac{1 + \frac{\sigma \bar{s}}{\alpha_{1,i}^2}}{1 + \frac{\sigma \bar{s}}{\alpha_{0,i}^2}} \right\} \; and \tag{2.24}$$

$$B = \prod_{i=1}^{\infty} \left\{ \frac{1 + \frac{\bar{s}}{\alpha_{1,i}^2}}{1 + \frac{\bar{s}}{\alpha_{0,i}^2}} \right\}, \tag{2.25}$$

where $\alpha_{0,i}$ and $\alpha_{1,i}$ are the ith zeros of the zero and first-order Bessel functions respectively.

Substituting (2.24) and (2.25) in (2.16) gives

$$\Gamma(\bar{s}) = \left[\frac{1 + (\gamma - 1)\prod_{i=1}^{\infty} \left\{ \frac{1 + \frac{\sigma \bar{s}}{\alpha_{1,i}^2}}{1 + \frac{\sigma \bar{s}}{\alpha_{0,i}^2}} \right\}}{1 - \prod_{i=1}^{\infty} \left\{ \frac{1 + \frac{\bar{s}}{\alpha_{1,i}^2}}{1 + \frac{\bar{s}}{\alpha_{0,i}^2}} \right\}} \right]. \tag{2.26}$$

The product in (2.26) is truncated to the order *m* and replaced in (2.23) giving

$$\cosh(\Gamma) = \prod_{i=1}^{\infty} \left\{ \frac{\left(\frac{\bar{s}}{Z_1} + 1\right)\left(\frac{\bar{s}}{Z_2} + 1\right)\ldots\left(\frac{\bar{s}}{Z_{m-2}} + 1\right)\left(\frac{\bar{s}^2}{\omega_{ni}^2} + \frac{2\bar{s}\zeta_i}{\omega_{ni}} + 1\right)}{\left(\frac{\bar{s}}{p_1} + 1\right)\left(\frac{\bar{s}}{p_2} + 1\right)\ldots\left(\frac{\bar{s}}{p_{m-1}} + 1\right)} \right\}. \tag{2.27}$$

For moderate viscous fluids, the real poles and zeros exactly cancel each other leaving only the complex zeros. The degree of cancellation varies for viscous fluid depending on the magnitude of D_n.

After calculating the residue of 1/cosh(Γ) at each of its complex poles, the modal approximation is of the form

$$\frac{1}{\cosh(\Gamma)} = \sum_{i=1}^{n} \frac{a_{ci}\bar{s} + b_{ci}}{\bar{s}^2 + 2\zeta_i \omega_{mi} \bar{s} + \omega_{mi}^2}, \tag{2.28}$$

where *n* is the number of second-order modes to be included in the approximation.

Using the same procedure, Z_c sinh(Γ)/cosh(Γ) and sinh(Γ)/ Z_c cosh(Γ) can be expressed in the form of rotational transfer function with identical denominators as

$$\frac{Z_c \sinh(\Gamma)}{\cosh(\Gamma)} = \sum_{i=1}^{n} \frac{a_{zi}\bar{s} + b_{zi}}{\bar{s}^2 + 2\zeta_i \omega_{mi}\bar{s} + \omega_{mi}^2} \quad \textit{and} \tag{2.29}$$

$$\frac{\sinh(\Gamma)}{Z_c \cosh(\Gamma)} = \sum_{i=1}^{n} \frac{a_{si}\bar{s} + b_{si}}{\bar{s}^2 + 2\zeta_i \omega_{mi}\bar{s} + \omega_{mi}^2} \,. \tag{2.30}$$

For all the hyperbolic functions of interest, the low-frequency magnitude is different from that of the corresponding modal approximation. Thus, a correction has been introduced by Hsue and Hullender [19] to rescale the D.C. gain of the modal approximation. In the present work, the approach introduced in [19] was validated for different pipe characteristics and liquid/gas properties. In some cases, this approach proves to be inappropriate and, hence, an alternate approach leading to a more accurate approximation is introduced.

While 1/cosh(Γ) has a low-frequency magnitude of unity, the corresponding modal approximation given in (2.28) has a low-frequency magnitude of $\sum_{i=1}^{n} \frac{b_{ci}}{\omega_{mi}^2}$. The approach of Hsue and Hullender [19] consists in dividing the Right Hand Side (RHS) of (2.28) by its low-frequency value to yield

$$\frac{1}{\cosh(\Gamma)} = \left[\sum_{i=1}^{n} \frac{b_{ci}}{\omega_{mi}^2} \right]^{-1} \sum_{i=1}^{n} \frac{a_{ci}\bar{s} + b_{ci}}{\bar{s}^2 + 2\zeta_i \omega_{mi}\bar{s} + \omega_{mi}^2} \,. \tag{2.31}$$

This approach leads to shifting the frequency response for all the frequencies to match the low-frequency values. An alternate approach for the low-frequency magnitude correction consists in matching the low-frequency magnitude of both the exact function and the modal approximation, through modifying b_1 in (2.28) to

$$b_{c1}^{'} = \omega_{m1}^{2}\left[1 - \sum_{i=1}^{n}\frac{b_{ci}}{\omega_{mi}^{2}} - \frac{b_{c1}}{\omega_{m1}^{2}}\right]. \tag{2.32}$$

Unlike the approach proposed in [19], this new approach will correct only the first zero of the approximated transfer function. To illustrate the correction effectiveness, both approaches are examined for a natural gas system represented in Table 2.1.

Table 2.1: System Properties for Correction Illustration

Pipe Length	914.4m
Pipe Diameter	0.0508 m
Gas Density	122.9
Gas Dynamic	0.011251e-
Gas Bulk Modulus	13789500

Given in Figure 2.3 is a comparison between the frequency response of the uncorrected modal approximation and the corrected ones using the approach in [19] given by (2.31) and the proposed approach given by (2.32).

Shown in Figure 2.3 (a) is an offset at low frequency between the exact and the approximate frequency responses. Both corrections are comparable in this case as shown in Figure 2.3(b) and Figure 2.3(c).

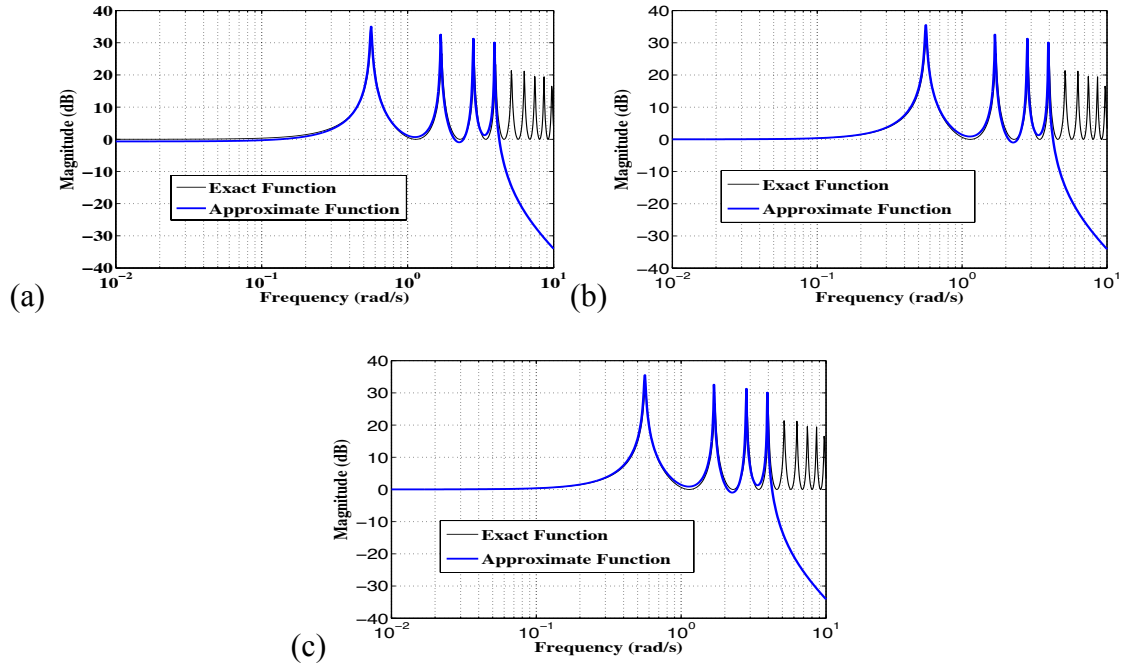

Figure 2.3: Modal Approximation of 1/Cosh(Γ): (a) Uncorrected, (b) Hullender's Correction, and (c) Alternate Correction

The modal approximation of Z_c sinh(Γ)/cosh(Γ) is of the form given by the RHS of (2.29). This transfer function is equivalent to $8D_n$ at steady state, where D_n is the pipeline dissipation number given by

$$D_n = \frac{\upsilon L}{cr^2}. \tag{2.32}$$

Hence, the RHS of (2.29) must be corrected using the same approach as for 1/cosh(Γ). Illustrated in Figure 2.4 is the difference between the pipeline frequency response using the two correction approaches. It is clear from Figure 2.4(b) that Hullender's correction shifts the approximation curve down to match the actual curve at low frequency resulting in an inaccurate approximation. However, the alternate

correction successfully matches the actual curve at low frequency while accurately capturing the dynamics.

The modal approximation for $\sinh(\Gamma)/Z_c \cosh(\Gamma)$ is of the form given by the RHS of (2.30). Hullender [19] does not propose any correction for this function whose mismatch to the actual function at low frequency is shown in Figure 2.4. An alternate approach is used to calculate the modal approximation. It consists of approximating the function divided by s and then multiplying the approximation by s. This approach proves to be more accurate as shown by the frequency response in Figure 2.5(b).

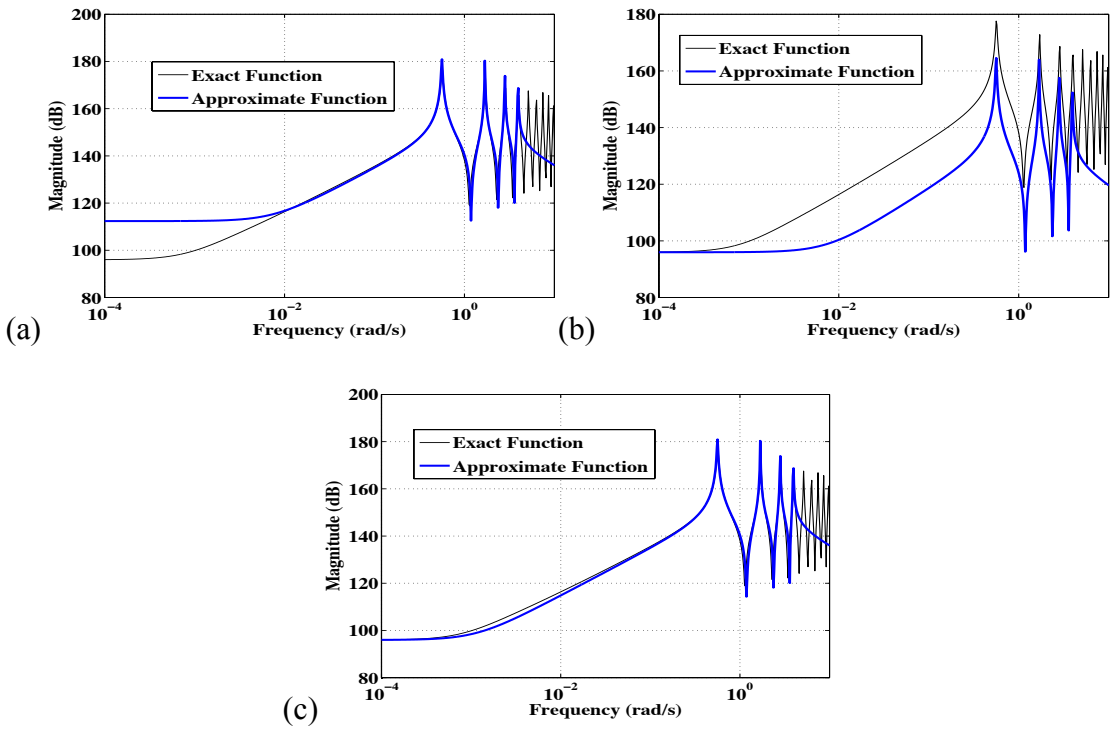

Figure 2.4: Modal Approximation of Z_c Sinh(Γ)/Cosh(Γ): (a) Uncorrected, (b) Hullender's Correction, and (c) Alternate Correction

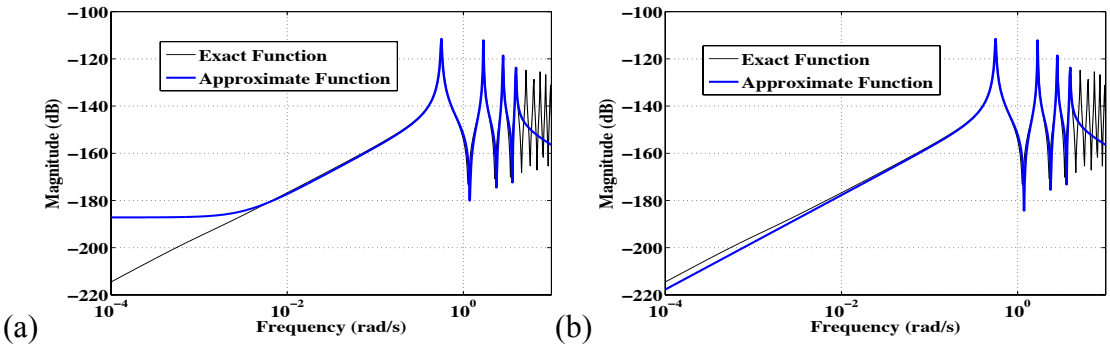

Figure 2.5: Modal Approximation of Sinh(Γ)/Z_c Cosh(Γ): (a) Uncorrected, and (b) Alternate Approach

2.2.3. Turbulent Flow Condition Modeling

In the lumped parameter model the resistance, inertance, and capacitance are located in one or more discrete locations along the pipeline. It is assumed that the inertance and capacitance of the line do not change with the flow being laminar or turbulent but only that the resistance will change with an increase in the Reynolds number. This part aims at modifying the dissipative distributed parameter model by adding a resistance at the end of the pipeline as shown in Figure 2.6. The additional resistance recovers the total steady flow resistance for turbulent flow through the pipeline.

Figure 2.6: Distributed Parameter Model with Lumped Turbulent Resistance

The steady-state pressure drop in the pipeline is given by

$$P_{in} - P_{out} = R_{Tot}Q = \frac{f_D \rho L Q^2}{2DA^2}, \tag{2.33}$$

where f_D is the Darcy friction factor. The lumped turbulent frictional resistance R_{Tur} is then defined by the following equation

$$P_{in} - P_{out} = (R_{Lam} + R_{Tur})Q, \tag{2.34}$$

where R_{Lam} is the steady state frictional resistance of the pipeline assuming laminar flow. Using (2.33) and (2.34) the lumped turbulent frictional resistance is given by

$$R_{Tur} = \frac{f_D \rho L Q}{2DA^2} - R_{Lam}. \tag{2.35}$$

Using the pipeline representation given by Figure 2.6, the fluid dynamic model will be given by the following system

$$\begin{cases} P_{in} = \dfrac{1}{\cosh(\Gamma)} P_2 + \dfrac{Z_c \sinh(\Gamma)}{\cosh(\Gamma)} Q_{in} \\ Q_{out} = \dfrac{-\sinh(\Gamma)}{Z_c \cosh(\Gamma)} P_2 + \dfrac{1}{\cosh(\Gamma)} Q_{in} \\ P_2 - P_{out} = R_{Tur} Q_{out} \end{cases}. \tag{2.36}$$

Solving this system will give the following matrix form

$$\begin{bmatrix} P_{in} \\ Q_{out} \end{bmatrix} = \begin{bmatrix} \dfrac{Z_c}{Z_c \cosh(\Gamma) + R_{Tur} \sinh(\Gamma)} & \dfrac{Z_c^2 \sinh(\Gamma) + R_{Tur} Z_c \cosh(\Gamma)}{Z_c \cosh(\Gamma) + R_{Tur} \sinh(\Gamma)} \\ \dfrac{-\sinh(\Gamma)}{Z_c \cosh(\Gamma) + R_{Tur} \sinh(\Gamma)} & \dfrac{Z_c}{Z_c \cosh(\Gamma) + R_{Tur} \sinh(\Gamma)} \end{bmatrix} \begin{bmatrix} P_{out} \\ Q_{in} \end{bmatrix}. \tag{2.37}$$

It can be noticed that substituting the lumped turbulent resistance by zero will result in recovering the dissipative transmission line model. A reduced-order approximation of the transfer functions in (2.12) is carried out using the same procedure detailed in the case of the laminar flow modeling.

Shown in Figures 2.7-2.9 is the frequency response of a four-modes approximation of the different transfer functions in (2.12) when varying the Reynolds number using the parameters presented in Table 2.2.

Table 2.2: System Properties for Turbulent Flow Dynamic Modeling

Pipe Length	500 m
Pipe Diameter	0.1 m
Oil Density	870 kg/m^3
Oil Dynamic Viscosity	0.0087Pa.s
Oil Bulk Modulus	2.54e^8 Pa

It is shown in Figures 2.7-2.9 that the developed model predicts that increasing the Reynolds number within the considered range does not affect significantly the system natural frequencies. In fact, the approximations of the transfer functions in (2.12) are characterized by a lower natural frequency equal to 1.637, 1.636, 1.635 and 1.624 rad/s for Reynolds numbers equal respectively to 1e3, 3e3, 1e4 and 1e5. Figures 2.7-2.9 show also that a higher Reynolds number results in a higher damping ratio due to the increase

in the lumped turbulent resistance term R_{Tur} in (2.12). Furthermore, the increase in the lumped turbulent resistance term results in a more significant pressure drop across the pipeline (2.34). Those conclusions are similar to the ones given by the lumped parameter model, where the increase in the Reynolds number affects only the resistance term resulting in a higher damping and pressure loss but does not affect the natural frequency which is function only of the system inertance and capacitance. However those conclusions need to be confronted to experimental data to assess their validity.

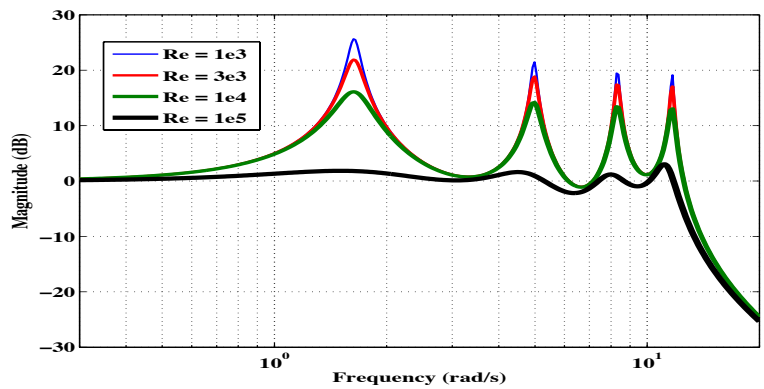

Figure 2.7: Frequency Response of the TF relating P_{in} to P_{out} and Q_{out} to Q_{in} for Different Reynolds Numbers

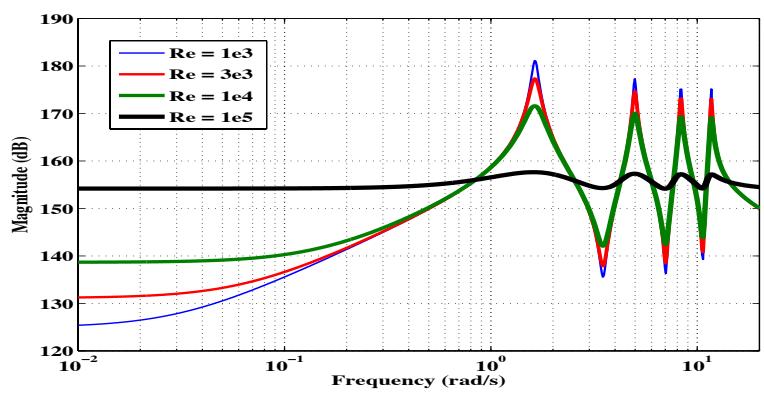

Figure 2.8: Frequency Response of the TF relating P_{in} to Q_{in} for Different Reynolds Numbers

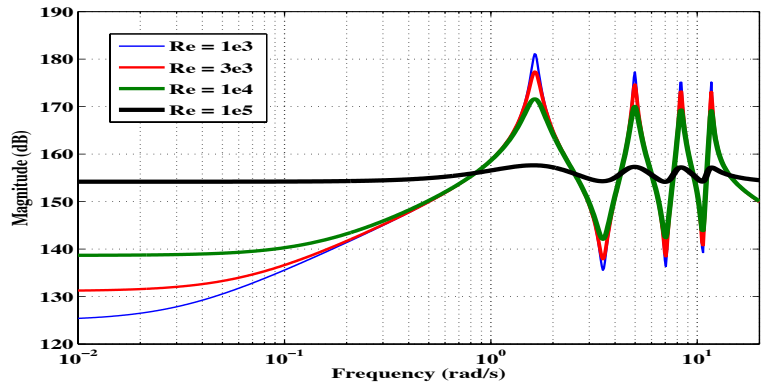

Figure 2.9: Frequency Response of the TF relating Q_{out} to P_{out} for Different Reynolds Numbers

To further evaluate its accuracy, the developed model is compared to the numerical and experimentally validated model of Johnston [69] for unsteady turbulent flow. Presented in Figure 2.10 is the frequency response of the two models for a laminar and a turbulent flow case.

Shown by Figure 2.10 is a good agreement between the two models in predicting the system natural frequency and damping ratio in the laminar flow case. However they present a slight discrepancy in the estimation of damping in the turbulent flow case. It is important to note that the Johnston model [69] is only valid for smooth-walled pipelines while the developed low-D model is equally applicable for turbulent flow in smooth and rough pipelines.

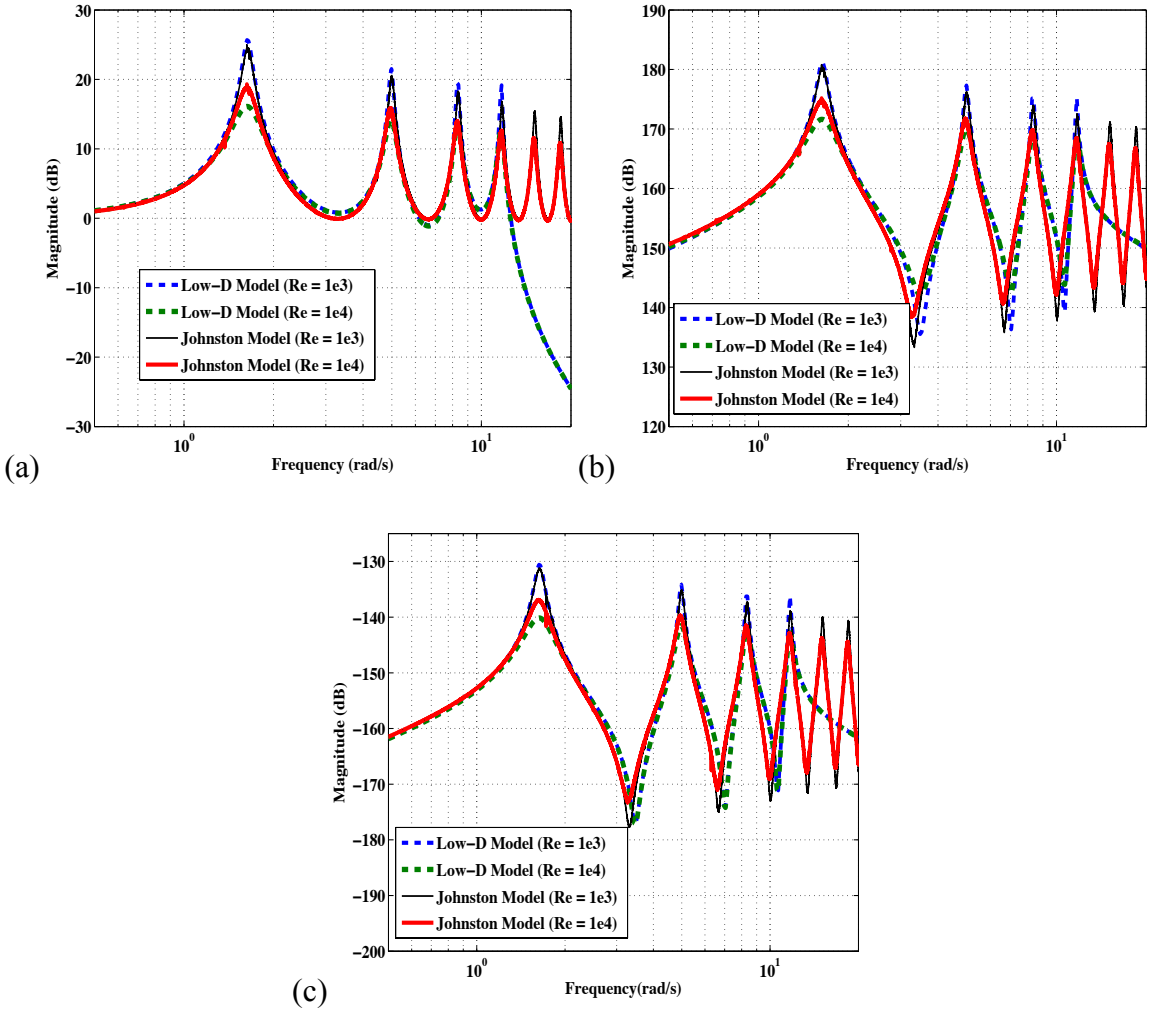

Figure 2.10: Frequency Response of the TF Relating: (a) P_{in} to P_{out} and Q_{out} to Q_{in}, (b) P_{in} to Q_{in}, and (c) Q_{out} to P_{out}

In sections 2.3 and 2.4 of this dissertation, the modified single-phase flow dissipative distributed parameter model is integrated with a mechanistic two-phase flow steady state approach through the derivation of equivalent fluid parameters. This approach results in a two-phase low-dimensional fluid model of transient two-phase flow in pipelines.

2.3. Two-Phase Flow Steady-State Mechanistic Modeling

Presented in this section is a mechanistic steady-state model for pressure gradient and liquid holdup prediction. This model assumes an incompressible liquid; ideal gas and no mass transfer between the two phases.

2.3.1. Model Philosophy

Based on fundamental laws of fluid mechanics, a mechanistic model for pressure gradient and liquid holdup estimation involves the momentum balance equations, which differ according to the gas and liquid configuration in a horizontal or inclined pipe. A distinction between different possible flow regimes is thus essential. As illustrated in Figure 2.11, the model distinguishes between 6 different flow patterns (regimes), namely:

- Bubble flow occurs when one fluid moves as small, dispersed bubbles through a continuous fluid. This regime normally occurs at low flow rate and low holdup of the bubbly fluid.
- Dispersed bubble flow occurs when the velocity of the continuous fluid increases. The bubbles are dispersed into smaller, more widely separated bubbles.
- Stratified flow occurs when the fluids are separated into different layers, with lighter fluids flowing above heavier fluids. This regime is more likely to occur at low rates and in flat or downhill sections of horizontal wells.
- Annular-mist flow occurs when the lighter fluid flows in the center of the pipe with small droplets of the heavier fluid, which itself, is contained in a thin film on the pipe wall.

- Intermittent flow is composed of plug (also referred to as elongated bubble), and slug flow regimes. In plug flow, liquid plugs are separated by elongated gas bubbles. In slug flow, the diameters of elongated bubbles become similar in size to the channel height.
- Froth flow occurs at a relatively high gas velocity, this flow is a transition between dispersed bubble flow and annular-mist flow and between slug flow and annular-mist flow. As the gas velocity increases, it changes into annular-mist flow.

For flow pattern determination, the steady state two-phase flow model in [45] presupposes the existence of a particular flow pattern and then examines various criteria that establish the stability of the flow regime. When the regime is determined to be unstable, a new flow pattern is assumed and the procedure is repeated. This procedure is illustrated in Figure 2.12.

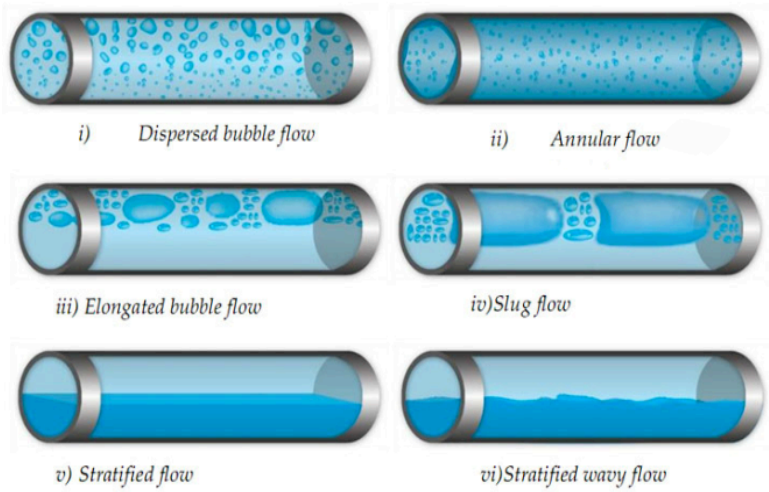

Figure 2.11: Two-Phase Flow Patterns [70]

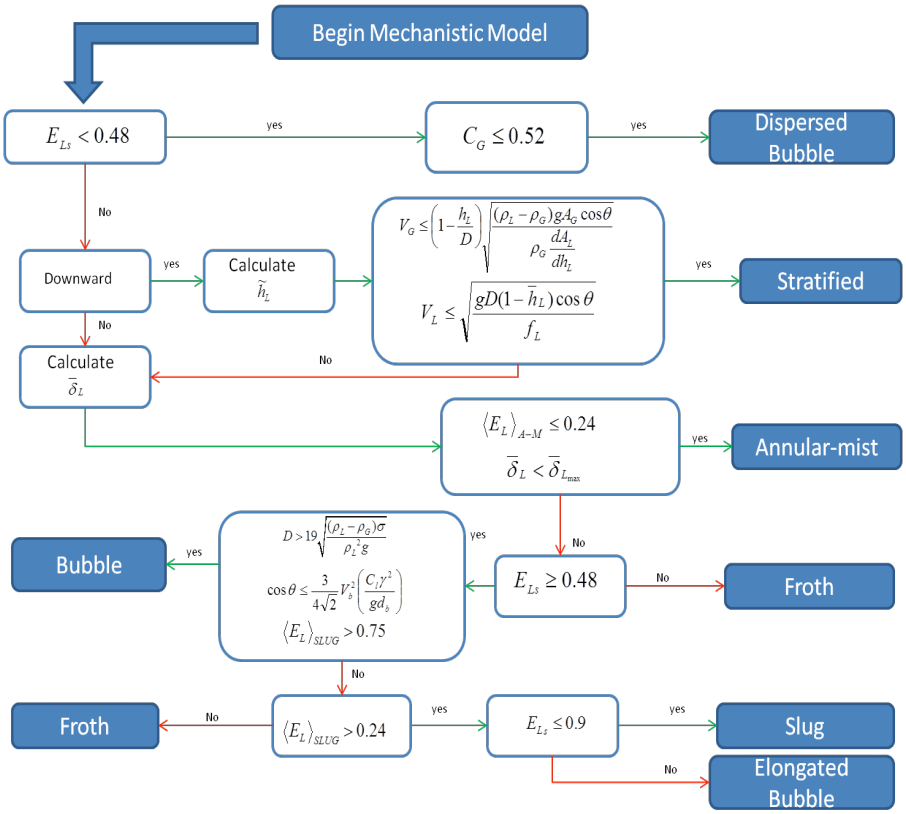

Figure 2.12: Flow Pattern Determination Procedure in Petalas and Aziz [50]

The first flow regime to be considered is the dispersed bubble, whose stability requires that the liquid fraction in the slug E_{Ls} to be less than 0.48 and the volumetric packing density of the dispersed bubbles to be less than 0.52. The next flow regime to be examined is stratified, in which the liquid height has to be calculated to make sure the waves at the liquid surface do not bridge the pipe. The approach of the annular-mist flow regime is similar to the one used for stratified flow. The liquid film height at which the minimum interfacial shear stress occurs has to be calculated to make sure the velocity profile remains positive. Also, the *in situ* volume fraction of liquid has to be less than one half of the value associated with the maximum volumetric packing density of uniformly sized gas bubbles in order to avoid bridging the pipe. When E_{Ls} is greater than 0.48 and

the stratified, annular and dispersed bubble flow regimes are proven to be unstable; the flow pattern will be either intermittent, bubble or froth. Bubble flow is stable when the Taylor bubble velocity exceeds the bubble velocity and the angle of inclination is large enough to prevent migration of the bubbles to the top wall of the pipe. Intermittent flow is stable when E_{Ls} is greater than 0.48 and the liquid volume fraction is greater than 0.24. Finally, when none of the transition criteria are met, the flow pattern is designated as Froth, implying a transitional state between the other flow regimes.

2.3.2. Aside: Comments on Parameter Selection

In this section, some comments, not included in [50] original work, are provided that help implementing the mechanistic model.

<u>Comment 1</u>: Froth flow is defined as a transition regime between the dispersed bubble, intermittent and annular-mist flow patterns. The calculation of the liquid holdup and the pressure gradient follows an interpolation approach between the three flow regimes. An iterative procedure is used to determine the values of the superficial gas velocity at the transitions and a log-log interpolation between these values is made as follows. If the superficial gas velocity at the transition from dispersed bubble flow $(V_{SG})_{DB}$ is greater than that from intermittent $(V_{SG})_S$ $(V(V_{SG})_{DB\ SG})_S$, the following relationships are used:

$$E_L = (E_L)_{AM}^{A}(E_L)_{DB}^{1-A} \ \ and \tag{2.38}$$

$$-\frac{dp}{dL} = \left[-\frac{dp}{dL}_{AM}\right]^{A} \times \left[-\frac{dp}{dL}_{DB}\right]^{1-A}, \tag{2.39}$$

with

$$A = \frac{\ln \dfrac{V_{SG}}{(V_{SG})_{DB}}}{\ln \dfrac{(V_{SG})_{AM}}{(V_{SG})_{DB}}}. \tag{2.40}$$

Otherwise, $(V_{SG})_{dB}$ is replaced by $(V_{SG})_S$ in the above equations.

Where E_L is the liquid holdup; V_{SL} is the superficial liquid velocity; V_{SG} is the superficial gas velocity; *AM* refers to the Annular Mist flow pattern and *DB* refers to the Dispersed Bubble flow pattern.

Comment 2: Determining the stability of the stratified and annular-mist flow regimes requires the calculation of the dimensionless liquid height and the dimensionless liquid film thickness. This is achieved by eliminating the pressure gradient by combining the momentum balance equations and solving a highly nonlinear equation using an iterative scheme. One non-negligible issue is the presence of multiple roots. Hence, it is essential to determine which one to use. Some authors assumed that the lowest root is the physical one [47]. It can be shown that the selection of one root over another affects the value of the gas superficial velocity at which a transition to another flow pattern occurs. Hence, it is necessary to ensure that, whether the lowest or the highest root is considered, the same root is used in all calculations so that discontinuities are prevented. In the present work, the lowest root is selected as suggested by Petalas and Aziz [50]. This is done by reducing the nonlinear equation to the form $f(x)=0$, evaluating the sign of f at the lower bound of the solution range of validity, and recording the value of x as soon as the sign of f changes. Another important comment relates to the friction factor. It is first

necessary to precise that in all the above equations, the Fanning friction factor is used. Moreover, in this model, the turbulent friction factor is used wherever it is greater than the laminar flow value. This helps preventing discontinuities that arise when the flow changes from laminar to turbulent.

2.3.3. Flow Pattern Map Discussion

Petalas and Aziz [50] included flow pattern maps for both an air/water system at standard conditions and an oil/gas system at reservoir conditions (Table 2.3). This was performed for different pipe inclinations, namely, horizontal, 10° upward, vertical upflow (+90°), and 10° downward. The maps cover a range of gas superficial velocity of 0.01 ft/sec to 500 ft/sec and a liquid superficial velocity of 0.01 ft/sec to 100 ft/sec.

Table 2.3: System Properties for Flow Pattern Maps

	Air/Water System	Oil/Gas System
Pipe Diameter	0.052 m	0.157 in.
Gas Density	1.28 kg/m^3	130.37 kg/m^3
Liquid Density	999.5 kg/m^3	841.45 kg/m^3
Gas Viscosity	0.01e-3 Pa.s	0.018 e-3 Pa.s
Liquid Viscosity	1.0 e-3 Pa.s	2.757 e-3 Pa.s
Interfacial Tension	72.4e-3 N/m	20 e-3 N/m
Absolute Pipe Roughness	4.57e-5m	30.48e-3m

Flow pattern maps were generated as described above and compared to those given in [50]. The generated flow pattern maps for both air/water and oil/gas systems are very similar to those given in [50] except for upward inclinations (10° and 90°). The only differences reside at the transitions from froth flow to annular-mist flow. This can be explained by the transition from the annular-mist regime, which is relevant only during uphill flow.

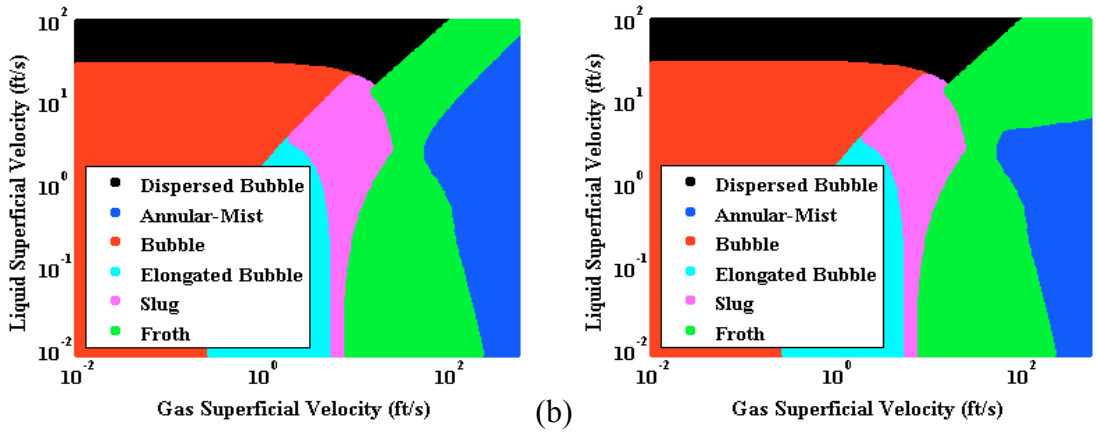

Figure 2.13: Flow Pattern Map for an Air/Water System at 90° Upward Inclination: (a) Petalas and Aziz Model (2000), and (b) Proposed Implementation

Aiming at understanding the inaccuracies between the generated flow pattern maps and those given in [50], the particular transition criterion was ignored and the maps generated again. The discrepancies between the flow pattern maps disappeared and the generated maps for both air/water and oil/gas systems at upward pipe inclinations matched exactly those given in [50]. This suggests that, for upward pipe inclinations, Petalas and Aziz [50] may not have included the transition criterion from annular-mist flow associated with the minimum interfacial shear stress when generating the flow pattern maps. Provided in Figure 2.13 is an example of a flow pattern map.

2.3.4. Model Validation

To evaluate the model overall performance, Petalas and Aziz [50] used the Stanford University Oil & Gas Database. This database contains pressure gradient, liquid holdup and flow pattern observations for a wide range of liquid and gas flow rates, fluid properties, and pipe inclinations. The database includes a total of 5,951 measurements spanning different fluid properties, pipe diameters, and upward as well as downward inclinations. The database, made available through Stanford University, contains 5,658

multiphase flow measurements. Detailed in Table 2.4 is the experimental data distribution according to the angle of inclination.

Table 2.4: Distribution of Experimental Data by Angle of Inclination

Angle of Inclination	-90° to -30°	-30° to 0°	0°	0° to +30°	+30° to +90°
Number of Data Points	601	500	2,254	937	1,366

Given in Table 2.5 is the fraction of the experimental data, contained in the Stanford University database that was predicted within 15% accuracy for both the pressure gradient and the liquid holdup.

Table 2.5: Accuracy of the Mechanistic Steady-State Model

Angle of Inclination	-90° to -30°	-30° to 0°	0°	0° to +30°	+30° to +90°
Liquid Holdup	48.42%	52.23%	54.83%	65.21%	62.88%
Pressure Drop	9.65%	32.06%	35.15%	43.44%	61.79%

It can be noticed from table 2.5 that the Steady-state model has a low accuracy for highly inclined downward flows (especially in the prediction of the pressure drop), which have limited applications in the oil and gas industry. However, the model accuracy improves significantly for the other considered inclinations.

Shown in Figure 2.14 are the predicted versus experimental values for both the pressure gradient and the liquid holdup, which exhibit a very similar trend to the results presented in Petalas and Aziz [50].

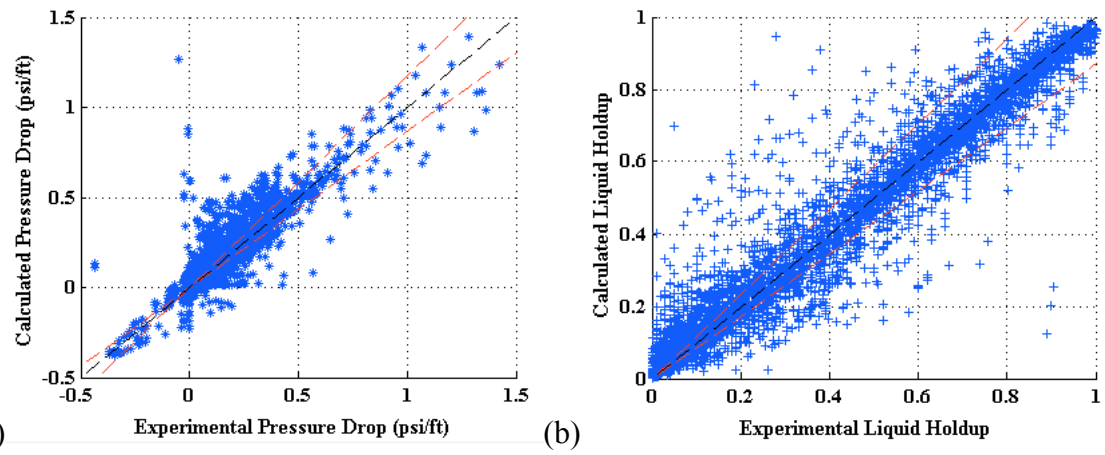

Figure 2.14: (a) Predicted vs. Experimental Pressure Gradient, and (b) Predicted vs. Experimental Liquid Holdup

2.4. Development of Equivalent Fluid Parameters

Based on the steady-state pressure drop and liquid holdup given by the mechanistic model, the equivalent fluid parameters, namely the bulk modulus, density, speed of sound, and viscosity are derived using the gas and liquid properties.

The bulk modulus describes the elasticity of a fluid as it undergoes a volumetric deformation. A problem with assigning a realistic value for the bulk modulus in the case of a two-phase flow is that even small amounts of air in the oil can substantially reduce the effective bulk modulus. To account for this phenomenon, the liquid and gas bulk moduli will be represented by two spring systems and combined in parallel with respect to their corresponding volume fractions. Hence, the following equation can be used to determine the equivalent bulk modulus of the liquid-gas mixture

$$\frac{1}{\beta_{eq}} = \frac{E_L}{\beta_L} + \frac{1-E_L}{\beta_G}, \tag{2.41}$$

where β_L is the liquid bulk modulus, β_G is the gas bulk modulus and E_L is the liquid holdup given by the steady-state model.

The stiffness of the equivalent fluid will then decrease considerably while increasing the Gas Volume Fraction (GVF) leading to lower frequencies of oscillations. However, this effect is more predominant at low GVF values due to the parallel combination of the gas and liquid bulk moduli.

The equivalent density of the two-phase fluid is calculated as

$$\rho_{eq} = E_L \rho_L + (1 - E_L)\rho_G \,, \tag{2.42}$$

where ρ_L and ρ_G are respectively the liquid and gas density.

Assuming a constant temperature inside the pipeline, the density of the equivalent fluid will be a function of the pressure only

$$\rho_{eq}(P) = \frac{\rho_0}{1 + \frac{1}{\beta_{eq}}(P_0 - P)} \,. \tag{2.42}$$

The equivalent speed of sound in the fluid is given by

$$c_{eq} = \sqrt{\frac{\beta_{eq}}{\rho_{eq}}} \,. \tag{2.43}$$

Increasing the amount of gas in the pipeline will result in a lower density and bulk modulus. However, the speed of sound is more sensitive to the bulk modulus leading to a lower speed of sound characterizing the equivalent fluid.

To calculate the equivalent viscosity, an equivalent Darcy friction factor is first calculated to match the frictional pressure gradient given by the mechanistic model.

The basic Darcy friction factor equation is

$$f_{eq} = \frac{2DA^2 \Delta P_{ss}}{\rho_{eq} Q^2}, \tag{2.44}$$

where D is the pipe diameter; A is the pipe cross-section area; Q is the flow rate and ΔP_{ss} is the steady-state pressure drop.

In the case of laminar flow, the equivalent dynamic viscosity will be given by

$$\mu_{eq} = \frac{1}{64} \rho_{eq} V_m D f_{eq}. \tag{2.45}$$

If the flow is turbulent, the Colebrook equation [71] is used to recover the equivalent viscosity. Other correlations can also be used such as Moody [72], or Goudar and Sonnad [73]. Using the Colebrook equation, the equivalent viscosity is expressed as

$$\mu_{eq} = \frac{1}{2.51} \rho_{eq} V_m D \sqrt{f_{eq}} \left[10^{-\frac{1}{2\sqrt{f_{eq}}}} - \frac{\varepsilon}{3.7D} \right], \tag{2.46}$$

where V_m is the gas and liquid mean velocity and ε is the pipe roughness.

2.5. Results and Discussion

2.5.1. Frequency Domain Analysis

The gas superficial velocity is maintained equal to *1 ft/s* and the liquid superficial velocity is increased to achieve 1%, 10%, 30%, and 60% GVF. Using those values the flow pattern will be respectively dispersed bubble, slug, elongated bubble, and stratified. The different simulation points are indicated in Figure 2.15.

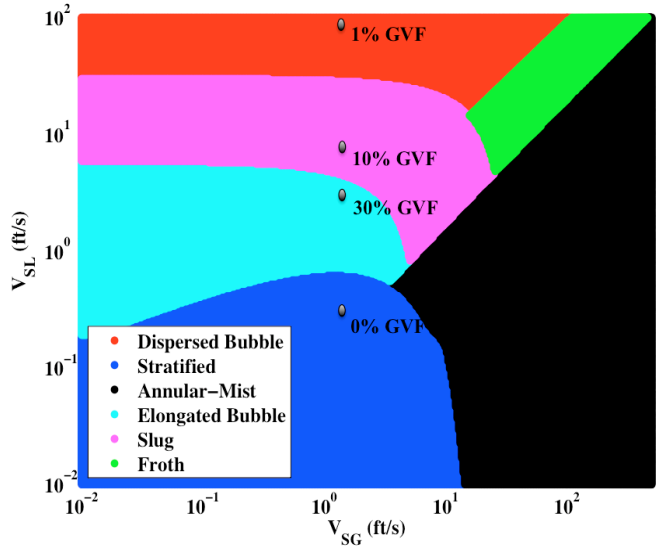

Figure 2.15: Simulation Points

Shown in Figure 2.16, is the frequency response of a 4-mode approximation of the different transfer functions using the equivalent fluid properties for different values of GVF. Increasing the gas volume fraction results in a lower equivalent bulk modulus and density. Due to entrained air in the system, the pipeline effective capacitance increases while the effective inertance decreases. However, the effect of the capacitance is dominant. This induces lower resonance frequencies associated with lower peaks as shown in Figure 2.16. Increasing the amount of entrained air also leads to a lower equivalent dynamic viscosity (lower effective resistance) resulting in a lower low-frequency gain for the transfer function Z_c sinh(Γ)/cosh(Γ), which relates the outlet pressure to the outlet flow. Decreasing the liquid velocity from a simulation point to another leads also to a lower total flow rate and consequently a lower total pressure gradient.

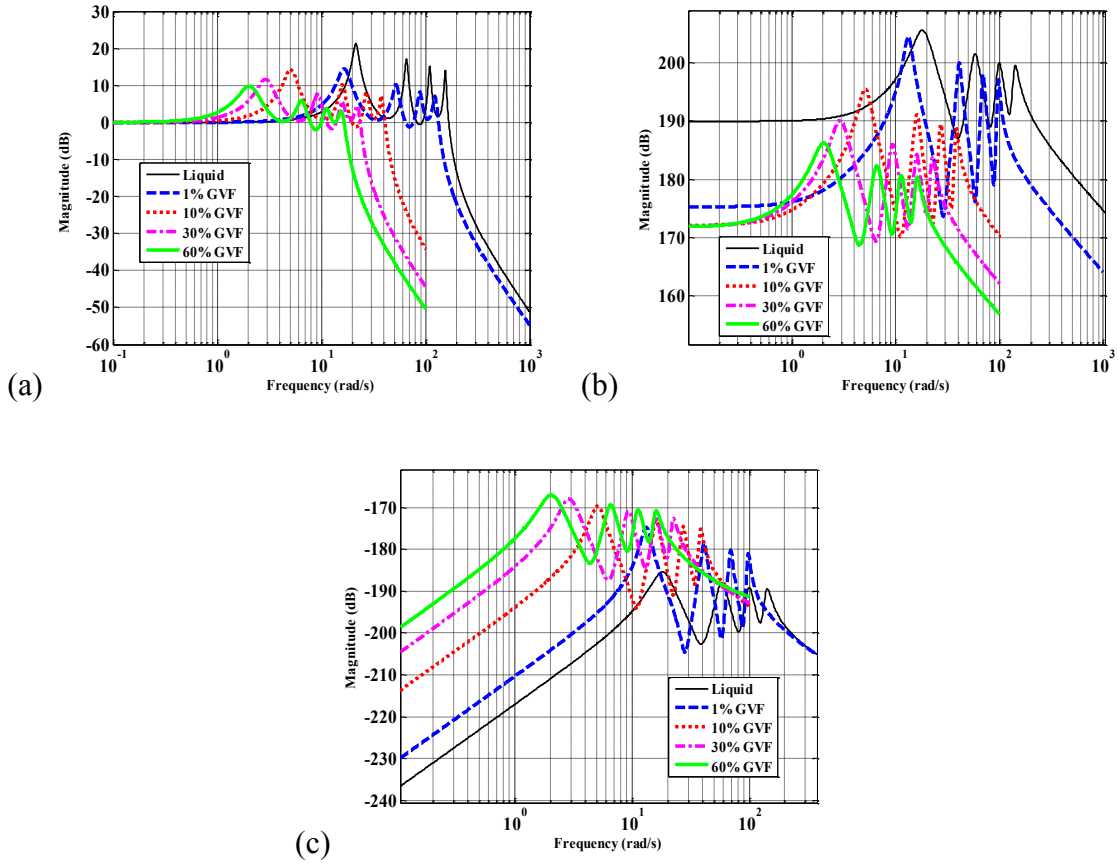

Figure 2.16: Four-Mode Frequency Response for Different GVF Levels: (a) 1/Cosh(Γ), (b) Z_c Sinh(Γ)/Cosh(Γ), and (c) Sinh(Γ)/Z_c Cosh(Γ)

2.5.2. Time Domain Analysis

Given in Figure 2.17 is the effect of the gas volume fraction level on the transient response of the two-phase system described in Tables 2.6-2.8.

Table 2.6: Pipe Characteristics

Pipe Length	Pipe Internal Diameter	Pipe Roughness	Pipe Inclination
500 m	0.1	0.0001 m	0°

Table 2.7: Gas and Liquid Properties

Liquid Density	870 kg/m^3
Liquid Viscosity	0.0087 Pa.s
Liquid Bulk Modulus	2.54e8 Pa
Gas Density	1.5 kg/m^3
Gas Viscosity	0.011251e-3 Pa.s
Gas Bulk Modulus	1e6 Pa
Surface Tension	0.02972 N/m

Table 2.8: Flow Conditions

Outlet Pressure	1e6 Pa
Inlet Flow Rate	Stepped from 0 to 0.005 m^3/s at t = 100 s
Gas Volume Fraction	0 to 30%

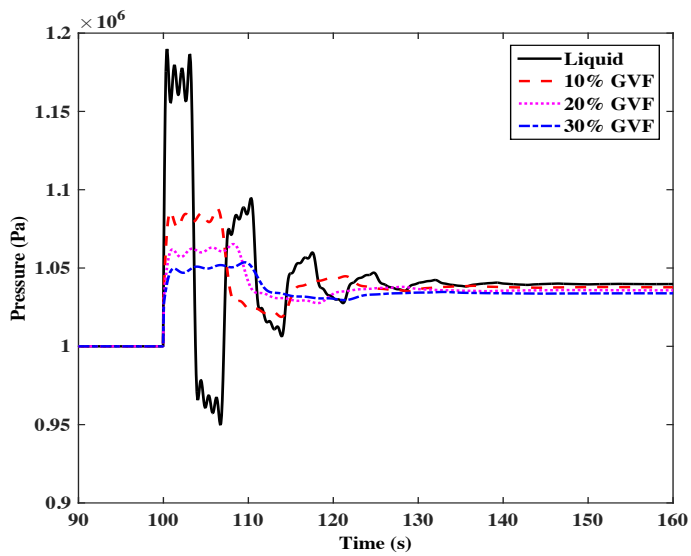

Figure 2.17: Inlet Pressure Time Response to Inlet Flow Rate Step for Different GVF

It can be noticed that a greater amount of gas in the pipeline results in less dynamic response. In fact, the greater the GVF, the lower the equivalent bulk modulus, the lower the equivalent speed of sound, the lower the natural frequencies, resulting in longer oscillations. Furthermore, increasing the amount of gas yields a smaller equivalent

viscosity resulting in a lower steady-state pressure drop. As for the damping in the pipeline, the greater the GVF, the lower the equivalent density and bulk modulus, the higher the damping ratio, which results in a lower overshoot and a lower settling time.

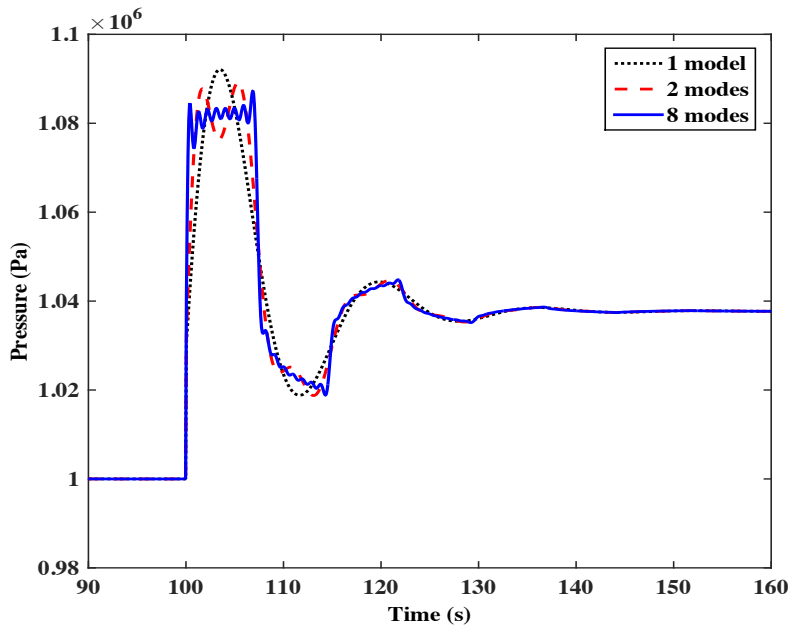

Figure 2.18: Inlet Pressure Time Response to Inlet Flow Rate Step for Different Truncation Orders

Shown in Figure 2.18 is the transient pressure at the pipeline inlet using different truncation orders of the hyperbolic transfer functions given by (2.12). Including more modes results in a more accurate approximation of the hyperbolic functions leading to a more dynamic response of the pressure, which is closer to the one experienced in actual field conditions. This effect is predominant in the first pressure peak due to the inclusion of higher frequency modes and will die out as the steady-state conditions are approached. This can be explained by the fact that the approximations using different truncation orders will all coincide at low frequency owing to the low-frequency magnitude corrections introduced earlier in this dissertation. However, including more modes will

increase the computation time, which can be critical for real-time applications and hence the trade off is essential.

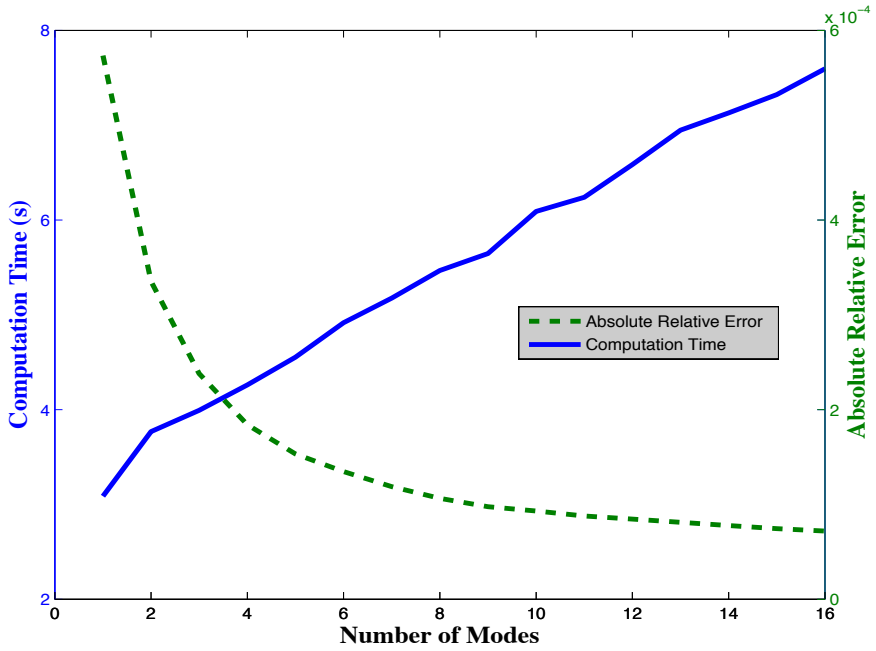

Figure 2.19: Computation Time vs. Absolute Relative Error

To illustrate this concept, the computation time and absolute relative error in predicting the inlet pressure of the two-phase system described by Tables 2.6-2.8 (using a 20-modes approximation as a reference) are plotted in Figure 2.19.

Figure 2.19 can be used to determine the minimum number of modes required to achieve the desired level of accuracy or the maximum number of modes that can be considered to maintain a computation time suitable for the real time monitoring of the flow and pressure. This step is even more critical when modeling complex systems such as multiple-well subsea architectures where the number of modes used in the approximation of (2.12) can have a considerable effect on the computation time and the simulations accuracy.

2.6. Conclusion

In this chapter, a new approach for transient two-phase flow in pipes has been presented. The model relies on a mechanistic model for steady-state pressure drop and liquid holdup estimation. Both of which are used to determine an equivalent single-phase fluid, which in turn, is fed to a distributed parameter model valid for laminar and turbulent flow conditions.

Although the developed low-D model included partially the effect of heat transfer on the pipeline's dynamic response through the propagation operator, the effect of the temperature variation on the gas and liquid properties was not accounted for. In Chapter 3, the model presented in this chapter are integrated with a two-phase flow heat transfer model resulting in a multiphysics two-phase flow pipeline model.

The frequency and time domain analysis showed that increasing the truncation order of the hyperbolic transfer functions constituting the low-D model results in a more accurate estimation of the pipeline's dynamic response but requires a higher computational power. It has been demonstrated that according to the newly developed low-D model, increasing the GVF level results in lower system's natural frequencies and damping ratios. The validity of those conclusions will be assessed in Chapter 4 of this dissertation by comparing the low-D model predictions to commercial software simulations and experimental data.

Chapter 3

Multi-Physics Two-Phase Flow: Hydraulic and Thermal Modeling

3.1. Introduction

Depending on the pipeline geometry, fluid properties and operating conditions, the gas and liquid mixture forms into a specific flow pattern (Chapter 2) making the prediction of the two-phase pressure, temperature and liquid holdup a challenging task. In the case of a slug flow, the interaction between the two-phases and the pipeline embodiment, including inclinations, creates a transient stress fluctuation resulting in a cyclic fatigue in the pipelines and riser [74]. Additionally, the produced fluids usually experience considerable heat losses to the cooler environment that could lead to pipeline blockage due to wax deposition, hydrate formation or asphaltene precipitation [75, 76]. To manage these production concerns, it is essential to accurately capture the multi-physics nature of the two-phase flow dynamics.

In Chapter 2, a low-dimensional model for transient two-phase flow in pipelines has been proposed. However, this model did not fully include the effect of the two-phase heat transfer on the pipeline dynamic response, making it not suitable to study some key problems such as wax deposition or hydrate formation where the determination of the fluid temperature is essential. Estimating the temperature of these multiphase production fluids not only avoids temperature related issues, but also contributes to a more efficient pumping of hydrocarbons from offshore sites [75-79].

To estimate the temperature of a given two-phase fluid, its heat transfer coefficient (denoted as h) needs to be determined. Efforts have been devoted to develop

different correlations to estimate h for several fluid combinations with different flow patterns. Rezkallah et al. developed a correlation to estimate h based on the GVF level [80]. Aggour [81] and Dorresteijn [82] proposed different correlations for laminar and turbulent flow. King [83] proposed correlations based on the ratio of pressure drop of two-phase fluids to single-phase liquids. Shah [84] and Knott et al. [85] developed correlations based on superficial velocities of liquids and gas present in the two-phase flow. Also, correlations based on dimensionless parameters such as Reynolds and Prandtl numbers, have been developed in [86, 87]. Kim et al. concluded that most of the empirical correlations were based on limited experimental data [88]. Thus, despite the efforts to develop comprehensive correlations, a single correlation would not be sufficient to determine the heat transfer coefficient for any two-phase flow fluid. Hence, a general model, applicable for a variety of flow types, is still required.

A holistic approach in developing correlations to estimate h of two-phase flow is necessary when employing multiphase flow mechanistic models. This form of modeling ensures that the results are applicable to most fluid combinations and flow patterns [50, 89]. While numerous efforts have been made to develop mechanistic models for h, the validity and robustness of these models have not been fully explored yet [90, 91]. Thus, there is still a need for a unified mechanistic thermal model for two-phase flow that has been successfully validated for a wide range of fluid mixtures and liquid-gas velocities combinations.

Presented in this chapter is the development of a two-phase flow pipeline multi-physics model. The mechanistic steady-state model in [50] is integrated with a mechanistic heat transfer model to determine the distribution of the steady-state pressure,

temperature, liquid holdup and fluids properties within the pipeline. Similarly to the development in Chapter 2, equivalent fluid properties are derived as a function of the GVF level and used to modify the pipeline dissipative distributed parameter model of Brown [17]. The resulting two-phase flow hydraulic and thermal fluid dynamic model constitutes a tool that can be used in a wide range of applications such as flow assurance, subsea architectures design and real-time condition monitoring. A sensitivity analysis is performed at the end of this Chapter to establish the causal effects of different parameters on the mixture flow within the pipeline.

3.2. Modeling Procedure

First, the pipeline is divided into segments. The steady-state coupling between the two-phase flow hydraulic and thermal models for each pipe segment is outlined in Figure 3.1. The mechanistic model of Petalas and Aziz [50] is used to determine the steady-state flow pattern, GVF and pressure drop. Those parameters serve as inputs to the two-phase flow thermal model allowing the temperature gradient across the pipeline's segment to be estimated. The average segment temperature and pressure are then used to determine the fluids properties through the Multiphysics Integration Block in Figure 3.1, which will be fed back to both the hydraulic and thermal models. The algebraic loops involved in this model are solved in a MATLAB® Simulink environment.

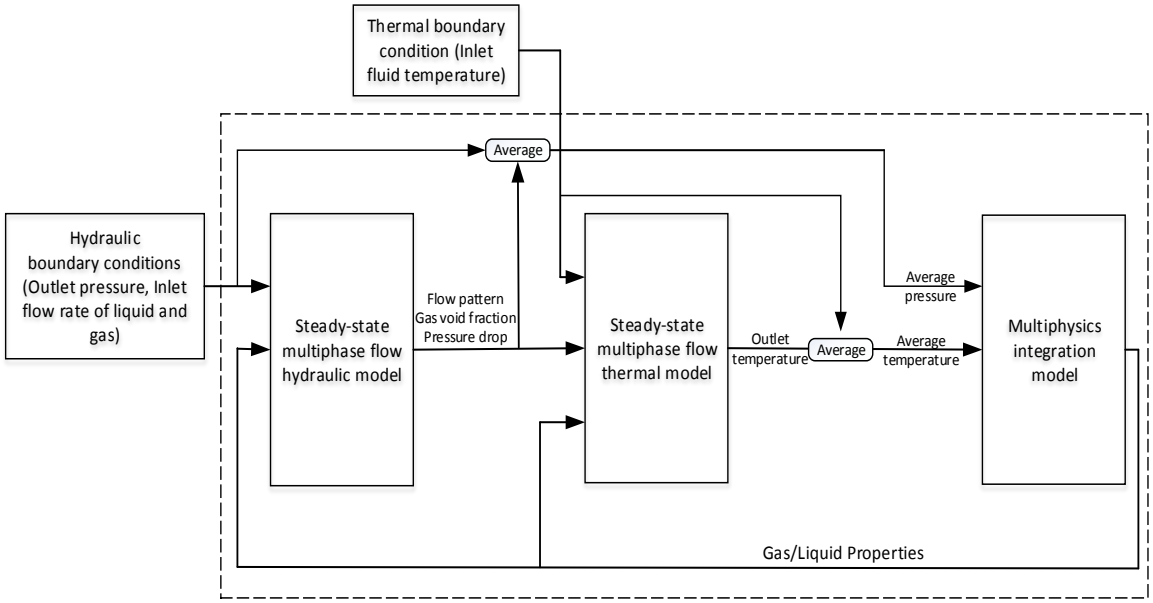

Figure 3.1: Steady-State Coupling of the Hydraulic and Thermal Models of a Pipeline Segment

In the second step, similarly to the approach adopted in Chapter 2, the steady-state flow pattern, GVF level and pressure gradient calculated in the first step are used to adjust the transient distributed parameter model. A modal approximation of the hyperbolic transfer functions capturing the mixture fluid transients are then carried out to simulate the pipeline two-phase flow dynamics for each pipeline segment (Figure 3.2).

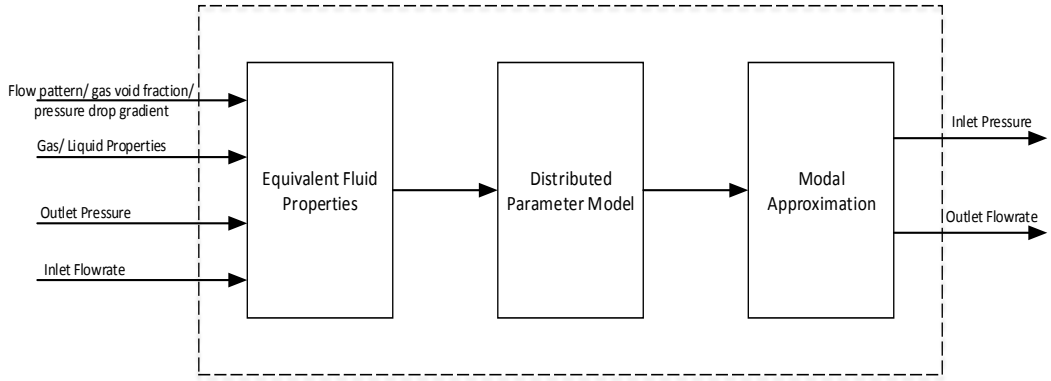

Figure 3.2: Two-Phase Flow Transient Hydraulic Model of a Pipeline Segment

As mentioned in Chapter 2, for causality considerations, the pressure and flow rate at the same location cannot be used as inputs for the pipeline mixture dynamics. Hence, either the inlet pressure and the outlet flow rate or the outlet pressure and the inlet flow rate are used as inputs for each considered pipeline segment. The different segments are combined as shown in Figure 3.3, when considering the outlet pressure and the inlet flow rate as system boundary conditions. The same procedure can be applied if the inlet pressure and outlet flow rate are used as system inputs.

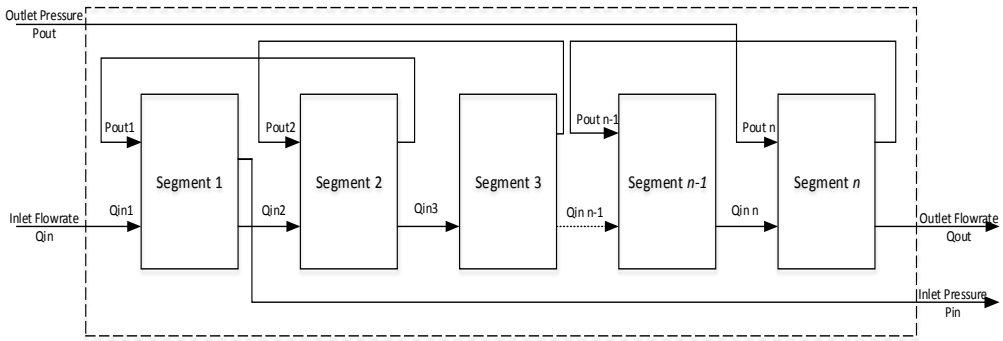

Figure 3.3: Pipeline Segmentation and Connections

For startup or shut down conditions, each considered pipeline segment would be subject to transient heat transfer phenomena that can last for hours. Coupling the two-phase flow hydraulic and thermal models only at steady state conditions (as suggested in Figure 3.1) will therefore lead to inaccurate estimations of the pipeline's pressure and temperature dynamic response. To cope with this limitation an additional transient multiphase flow thermal module is added to the proposed multi-physics model. This will allow the real time adaptation of the equivalent fluid properties based on the transient pressure and temperature conditions using the multiphysics integration block. The model

user can easily deactivate the transient thermal module if only steady-state heat transfer phenomena are of interest.

In this Chapter, we will emphasize on the derivation of the two-phase flow steady-state and transient thermal models and their integration with the hydraulic low-D models developed in Chapter 2.

3.3. Two-Phase Flow Thermal Models

In this section, steady-state and transient thermal models are proposed for the distributive, segregated and intermittent multi-phase flow patterns.

3.3.1. Steady-State Two-Phase Flow Thermal Model

A cross sectional view of an insulated pipeline is given in Figure 3.4. The pipeline is subject to convective heat transfer from the two-phase flow production fluid to the pipe inner wall, conductive heat transfer thru the pipe wall and insulation and convective heat transfer from the insulation layer into the surrounding environment.

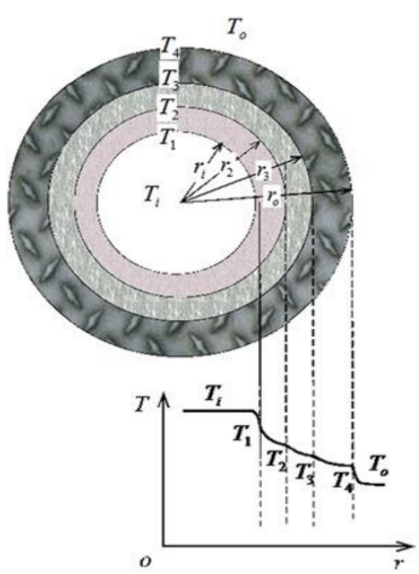

Figure 3.4: Cross Sectional View of an Insulated pipeline [64]

The heat loss in a pipeline segment of length dx is given by

$$dq(x) = U\left(\pi \times ID \times dx\right)\left(T_{fluid}(x) - T_{ambient}\right), \tag{3.1}$$

where U is the overall heat transfer coefficient, ID is the pipe internal diameter, T_{fluid} is the production fluid temperature and $T_{ambient}$ is the surrounding fluid temperature.

Assuming that the heat flow is from the production to the surrounding fluid, a constant specific heat capacity, no mechanical work involved (no pumps) and neglecting kinetic energy, gravitational energy and frictional heating of the fluid due to flow, an energy balance of the pipeline segment gives

$$dq(x) = -\dot{m}\, c_p\, dT_{fluid}(x), \tag{3.2}$$

where $\dot{m}$ is the mass flow rate, and c_p is the specific heat capacity.

Using (3.1) and (3.2) the pipeline segment outlet fluid temperature can be derived as

$$T_{out} = \left(T_{in} - T_{ambient}\right)\exp\left(\frac{-U\left(\pi \times ID\right)}{\dot{m}\, c_p} L\right) + T_{ambient}, \tag{3.3}$$

where T_{in} and T_{out} are respectively the inlet and outlet temperatures.

For the case of a pipeline with n insulation layers, the overall heat transfer coefficient is given by

$$U^{-1} = \underbrace{ID \times \sum_{i=1}^{n+1}\left\{\frac{\ln\left(\frac{ID_{i+1}}{ID_i}\right)}{2k_{cond_i}^{material}}\right\}}_{Conduction} + \underbrace{\frac{1}{h_{tp}} + \frac{1}{h_o \times \left(OD / ID\right)}}_{Convection}, \tag{3.4}$$

where $k_{cond_i}^{material}$ is the corresponding material conductivity, h_{tp} is the two-phase flow internal convection heat transfer coefficient and h_o is the external convection heat transfer coefficient.

In each two-phase flow patterns, the two-phase flow convection heat transfer coefficient h_{tp} is determined from the equivalent Nusselt number Nu_{eq}, equivalent thermal conductivity K_{eq}, and diameter D, as

$$h_{tp} = \frac{Nu_{eq} K_{eq}}{D}. \tag{3.5}$$

For each flow pattern, the Nusselt number is determined differently. Detailed below is the procedure for determining the two-phase flow convection heat transfer coefficient for the different considered flow patterns.

3.3.1.1. Distributive Flow

In this model, the distributive or distributed flow is comprised of dispersed bubble and bubble flow. Distributive flow is commonly approximated as a pseudo single phase. The proposed model uses the liquid holdup and gas-liquid properties to determine the equivalent two-phase density (2.42). Similarly, the specific heat capacity and thermal conductivity are respectively given by

$$Cp_{eq} = E_L Cp_L + (1 - E_L) Cp_G \ \ and \tag{3.6}$$

$$K_{eq} = E_L K_L + (1 - E_L) K_G. \tag{3.7}$$

However, since gas viscosity is usually negligible relatively to the liquid viscosity, and the lowest GVF levels characterize the distributive flow, liquid viscosity is usually equivalent to the two-phase viscosity. Dimensionless properties of equivalent Reynolds and Prandtl numbers are determined using

$$\mathrm{Re}_{eq} = \frac{\rho_{eq} V_m D}{\mu_L} \; and \tag{3.8}$$

$$\mathrm{Pr}_{eq} = \frac{\mu_L Cp_{eq}}{K_{eq}}. \tag{3.9}$$

When fluid enters and makes contact with the pipeline surface, the fluid velocity profile changes along the length of the pipeline [92]. After a certain length, the fluid velocity profile becomes uniform and it gets thermally and hydro-dynamically developed. For laminar flow, these developing regions can adversely affect the thermal and hydrodynamic profile. Therefore, for laminar flow, it is essential to first determine whether the flow is thermally and hydro-dynamically developed or not. This is done by determining the Graetz number as

$$Gz_{eq} = \frac{\mathrm{Re}_{eq}\mathrm{Pr}_{eq}}{L/D}. \tag{3.10}$$

For laminar flow with Graetz number less than 20, flow is not thermally and hydro-dynamically developed. Hence Sieder and Tate correlation is used [93]

$$Nu_{eq} = 1.86\left[\left(\frac{D}{L}\right)\mathrm{Re}_{eq}\mathrm{Pr}_{eq}\right]^{1/3}\left[\frac{\mu_{L,b}}{\mu_{L,w}}\right]^{0.14}. \tag{3.11}$$

If the Graetz number is greater than 20, flow is fully developed. In fully developed flow, if Prandtl number is greater than 5, Hausen correlation is used [94]. This correlation is also used when flow is hydro-dynamically developed, but thermally developing, namely

$$Nu_{eq} = 3.657 + \frac{0.0668\left(\frac{D}{L}\right)\mathrm{Re}_{eq}\mathrm{Pr}_{eq}}{1 + 0.04\left[\left(\frac{D}{L}\right)\mathrm{Re}_{eq}\mathrm{Pr}_{eq}\right]^{2/3}}. \tag{3.12}$$

If Prandtl number is less than 5, for fully developed laminar flow, and with constant surface temperature, the Equivalent Nusselt is given by [92]

$$Nu_{eq} = 3.657. \tag{3.13}$$

For fully developed laminar flow with constant surface heat flux, the Equivalent Nusselt is given by [92]

$$Nu_{eq} = 4.364. \tag{3.14}$$

For Turbulent Flow Conditions, the equivalent Nusselt number can be determined using the Gneilinski correlation [95]

$$Nu_{eq} = \frac{\left(\frac{f_{eq}}{8}\right)\left(\mathrm{Re}_{eq} - 1000\right)\mathrm{Pr}_{eq}}{1.07 + 12.7\sqrt{\frac{f_{eq}}{8}}\left(\mathrm{Pr}_{eq}^{2/3} - 1\right)}, \tag{3.15}$$

where f_{eq} is the equivalent Friction factor given by the Petalas and Aziz Model [50].

Summarized in Figure 3.5 are the different steps of the proposed method for determining the Nusselt number for two-phase distributive flow. This number is used to

calculate the heat transfer coefficient for distributive flow, using (3.5). It is shown that the steps used to calculate the Nusselt number for distributive flow is similar to the method used for single phase fluids.

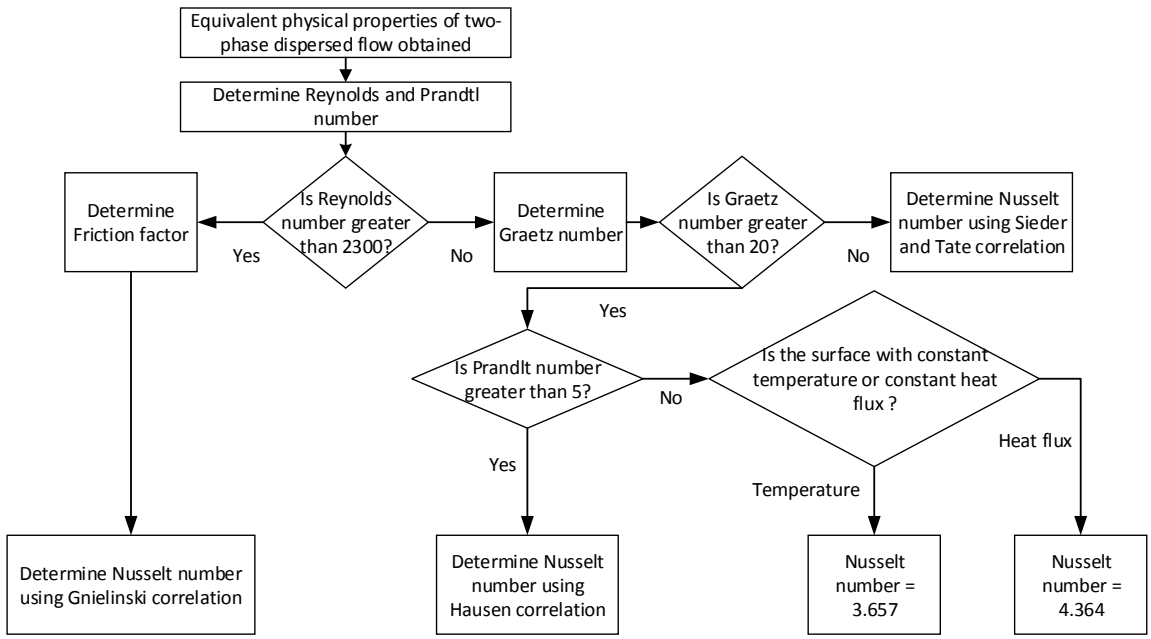

Figure 3.5: Method to Determine the Nusselt Number for Two-Phase Distributive Flow

3.3.1.2. Segregated Flow

Segregated or separated flow is comprised of stratified and annular-mist flows. For laminar flow conditions, Kaminsky's equation [96] is used

$$h_{tp} = \frac{h_{SL}\left(2.08 - E_L\right)S^{1/3}}{E_L^{2/3}}, \tag{3.16}$$

where S is the normalized wetted perimeter, E_L is the liquid holdup and h_{SL} is determined using the superficial liquid velocity.

For stratified flow, S is calculated as [45]

$$S_{str} = \pi - \cos^{-1}(2h_L - 1), \tag{3.17}$$

where h_L is the normalized liquid height calculated by the Petalas and Aziz model [50]. For annular flow,

$$S_{ann} = 1. \tag{3.18}$$

For horizontal segregated turbulent flow, the overall two-phase heat transfer coefficient is calculated as [96, 97]

$$h_{tp} = \frac{k_L\sqrt{\rho_L}}{10\mu_L}\left[SD\left(\frac{dP}{dL}\right)_{tp}\right]^{1/2}. \tag{3.19}$$

For vertical segregated turbulent flow, the ratio of heat transfer coefficients for two-phase flow and superficial liquid is considered, since the shear stress related formula (3.19) is not able to accurately predict the heat transfer coefficient according to Kaminsky [96]

$$h_{tp} = h_{SL}\left[SD\frac{\left(\frac{dP}{dL}\right)_{tp}}{\left(\frac{dP}{dL}\right)_{SL}}\right]^{1/2}, \tag{3.20}$$

where the liquid heat transfer coefficient h_{SL}, can be determined using superficial liquid properties, and the distributive flow method, as shown in Figure 3.5 and (3.5). $\left(\frac{dP}{dL}\right)_{SL}$ can be determined using Moody's friction factor and superficial liquid properties. $\left(\frac{dP}{dL}\right)_{tp}$ is determined using Petalas and Aziz model [50], for all flow types.

3.1.3.3. Intermittent Flow

Intermittent flow encompasses slug and elongated bubble flows. Both Flow patterns are comprised of successive periodic units. Each unit consists of a Taylor gas bubble region with a liquid film, and a liquid region with entrained gas.

The heat transfer coefficient for the gas bubble region with the liquid film h_{bf}, is calculated using the method for segregated flow, described earlier. The heat transfer coefficient for the Liquid region h_{sl}, is calculated using the distributive flow procedure based on the liquid-gas properties and the portion of the entrained gas in the liquid region. The overall heat transfer coefficient h_{tp}, is determined for intermittent flow, using [98]

$$h_{tp} = \alpha h_{bf} + (1-\alpha) h_{sl}, \tag{3.21}$$

where α is the ratio of the length of the gas bubble and liquid film part, to the length of the entire intermittent unit. α can be approximated using the ratio of the superficial velocity of gas to the translational velocity of the intermittent unit

$$\alpha = \frac{l_{bf}}{l_{bf} + l_{sl}} \approx \frac{V_g}{V_t}, \tag{3.22}$$

where V_t, the translational velocity of the intermittent unit, can be determined using the correlation and parameters proposed by Bendisken, Nicklin and Dumitrescu [99-101]

$$V_t = 1.05 \sin^2(\theta) V_m + \cos(\theta) 0.54 \sqrt{gD} + \sin(\theta) 0.35 \sqrt{gD}, \tag{3.23}$$

where θ is the angle of inclination of pipe from the horizontal plane. V_m is the sum of the superficial gas and liquid velocities.

3.3.2. Transient Two-Phase Flow Thermal Model

Unlike fluid systems, where the transient behavior is characterized by the Inertance, Resistance and Capacitance (Chapter 1), thermal systems transient behavior is characterized only by the thermal Resistance and Capacitance. For the case of heat transfer in insulated pipelines, those parameters relate the fluid temperature to the ambient temperature for the case of a pipeline shut down as follows:

Thermal Capacitance: $$-q_{out} = m\, c_{p_{tp}}\, \dot{T}_{Fluid} \text{ and} \tag{3.24}$$

Thermal Resistance: $$T_{Fluid} - T_{amb} = R\, q_{out}. \tag{3.25}$$

The two-phase specific heat capacity $c_{p_{tp}}$ and the thermal resistance R are given by

$$c_{p_{tp}} = \chi c_{p_G} + (1-\chi) c_{p_L}, \text{ and} \tag{3.26}$$

$$R = \underbrace{\sum_{i=1}^{n+1} \left\{ \frac{\ln\left(\frac{ID_{i+1}}{ID_i}\right)}{2\pi L\, k_{cond_i}} \right\}}_{Conduction} + \underbrace{\frac{1}{\pi \times ID \times L \times h_{tp}} + \frac{1}{\pi \times OD \times L \times h_o}}_{Convection}, \tag{3.27}$$

where χ is the gas mass fraction, c_{p_G} and c_{p_L} are respectively the gas and liquid specific heat capacities and T_{amb} is the ambient temperature.

Based on (3.24) and (3.25), the following Ordinary Differential Equation (ODE) can be established

$$\dot{T}_{Fluid} + \frac{1}{R\,m\,c_p} T_{Fluid} = \frac{1}{R\,m\,c_{p_{tp}}} T_{amb}. \tag{3.28}$$

Solving the ODE in (3.28) yields to

$$T_{Fluid}(t) = T_{amb} + \left(T_{Fluid}(0) - T_{amb}\right) e^{-t/t_c}, \tag{3.29}$$

where

$$t_c = R\,m\,c_{p_{tp}}. \tag{3.30}$$

The time constant t_c characterizes how fast the temperature reaches the steady state conditions. The same model can be used for the startup conditions.

3.3.3. Model Validation

To validate the proposed two-phase flow thermal model, an independent experimental dataset was constructed from the literature. A summary of experimental data sources, used to validate the two-phase thermal model, is presented in Table 3.1.

The predicted heat transfer coefficients, using the proposed thermal model, for two-phase flow are compared with experimental heat transfer coefficients, as shown in Figures 3.6 and 3.7, and Table 3.2.

Table 3.1: Experimental Data Used for the Validation of the Thermal Model

Source	Experimental Setup	Fluid Mixtures	Length(m) / Diameter(m) of pipe	Reynolds Number Range
Vijay [102]	Heated vertical tube	Air - Water Air - Glycerin (75%), Water (25%) Air - Glycerin	0.61/0.01	$43 \le \mathrm{Re}_g \le 157712$ $2 \le \mathrm{Re}_l \le 126628$
Sujumnong [103]	Heated vertical tube	Air - Water Air - Glycerin (59%), Water (41%) Air - Glycerin (85%), Water (15%)	0.61/0.01	$17 \le \mathrm{Re}_g \le 148169$ $9 \le \mathrm{Re}_l \le 106829$
Aggour [81]	Heated vertical tube	Air - Water Helium - Water Freon - Water	0.61/0.01	$14 \le \mathrm{Re}_g \le 209432$ $3841 \le \mathrm{Re}_l \le 144525$
Manabe [97]	Cooled horizontal and vertical tube	Natural gas - Crude oil	9.15/0.05	$7280 \le \mathrm{Re}_g \le 845740$ $770 \le \mathrm{Re}_l \le 27695$
Kim [104]	Heated horizontal tube	Air - Water	2.79/0.03	$536 \le \mathrm{Re}_g \le 6448$ $2468 \le \mathrm{Re}_l \le 35503$

Table 3.2: Steady-State Thermal Mechanistic Model Accuracy

Flow pattern	Average Percentage Error	Percentage of points predicted within 30% accuracy
Vertical distributed	14.7	96.5
Vertical segregated	44.7	36.3
Vertical intermittent	45.6	52.4
Horizontal segregated	18.4	75.0
Horizontal intermittent	15.1	92.5

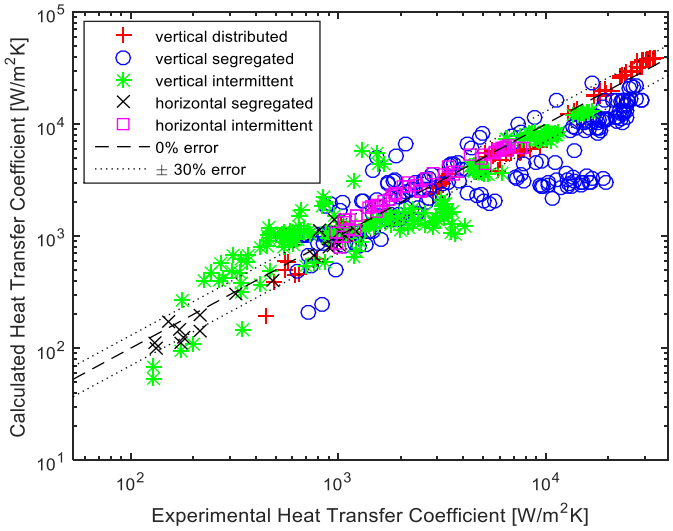

Figure 3.6: Comparison of Predicted and Experimental Heat Transfer Coefficients for Different Flow Patterns

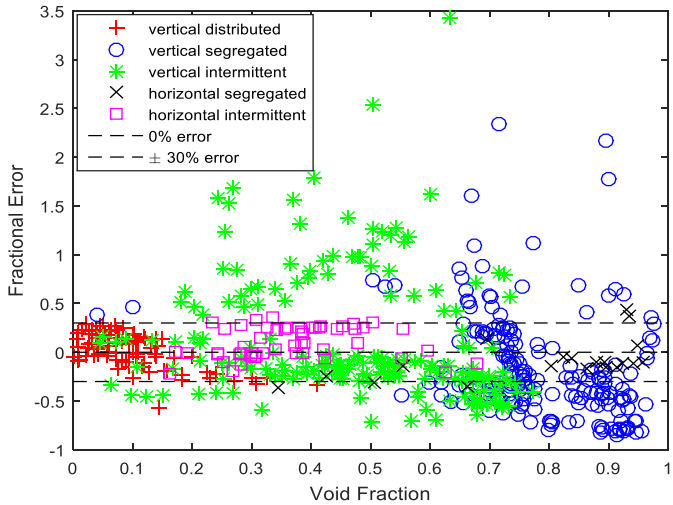

Figure 3.7: Fractional Error for Different Flow Patterns with Respect to Gas Void Fractions

For distributed flow, the model was validated with data for a vertical pipeline only, due to the lack of data. For distributed flow for different fluid mixtures, the proposed model was able to accurately predict 96.5% of the data points with less than 30% error. Thus the equivalent properties, which are determined using void fraction and single phase properties, are ideal to determine the heat transfer characteristics of two-

phase distributed flow for laminar, transitional, and turbulent flow. Despite the presence of thermal and hydro-dynamic developing regions in the experimental setups for distributed flow, it was seen that according to the Graetz number, the two-phase flow was not thermally and/or hydro-dynamically developed for some data points. Therefore, these regions had to be considered prior to determining the two-phase heat transfer coefficient.

The proposed segregated model was validated with horizontal and vertical inclinations. This model, similarly to Manabe [97] and Kaminsky [90], was based on equivalent liquid properties for laminar models, and shear stress and pressure drops for turbulent models. For horizontal flow, the proposed segregated model is able to predict the heat transfer coefficients with less than 20% average error for laminar and turbulent flow cases. Thus the approximation in this model, that most of the heat transfer occurs across the liquid's boundary, is valid. For the vertical segregated flow, the proposed model shows a higher absolute error, with less number of data points within 30% accuracy. A more accurate understanding of the heat transfer may be necessary here to increase the accuracy for vertical two-phase segregated flow.

It is shown in Figure 3.7 that for vertical flow, errors are higher for intermittent and segregated flow, particularly for gas void fractions greater than 0.2. For horizontal intermittent and segregated flow across the entire void fraction range, fractional absolute errors are generally below 30%. The proposed intermittent model heavily relies on the distributed and segregated models. It can be noticed that, for horizontal flow, where the accuracy of the segregated model is relatively higher than that for vertical flow, the accuracy of intermittent model is also higher. Thus, along with dispersed flow, slug

length to slug unit ratio, the underlying segregated model needs to have acceptable accuracy of more than 50%.

Since the proposed heat transfer model uses no empirical results, the model may be applied to data outside the stated parameters listed in Table 9. This model goes beyond the conventional data sets containing either water, glycerin, air, or noble gas mixtures and extends to crude oil-natural gas mixtures. Detailed comparisons of these models with existing heat transfer models can be found in several sources [88, 90, 97, 105], and it can be seen that most of the previous heat transfer models have either been considered valid for the former or latter data.

3.4. Multiphysics Integration Block

For a given pressure and temperature, the hydraulic and thermal properties of the liquid and gas need to be defined. Multiphysics integration subsystem is used to connect the hydraulic and thermal models in steady state conditions. This block is based on a Pressure, Volume and Temperature (PVT) database, which updates the thermal and hydraulic properties based on temperature and pressure of the liquid and gas in two-phase flow. The properties include density, viscosity, bulk modulus, specific heat capacity and thermal conductivity of gas and liquid, and surface tension of liquid in the two-phase fluid. The PVT database, obtained from a defined PVT file for a specific liquid and gas mixture, was imported into a Simulink look-up table. The final model is able to estimate different properties of liquid and gas with respect to different pressures and temperatures. Due to the nonlinear behavior of the gas and liquid properties with respect to temperature and pressure, spline function was used to interpolate between different temperatures and pressures. The range of the Multiphysics Integration Block depends on the limit defined

by the data. For the current data set used in this study, temperature ranges between -10 °C and 100 °C, while the pressure ranges between 100 kPa and 2,000 kPa.

3.5. Results and Discussion

The developed hydraulic and thermal models are simulated to discuss how the operating conditions and the inputs can affect the model estimations. A sensitivity analysis is performed in this section to evaluate the effect of some key parameters on the pipeline's dynamic response. Presented in Tables 3.3-3.5 are the characteristics of the base case.

Table 3.3: Pipeline and Insulation Properties

Pipe Length	3000 m
Number of Segments	1
Pipe Diameter	0.1 m
Pipe Wall Thickness	0.01 m
Pipe Thermal Conductivity	50 W/(m.K)
Insulation Wall Thickness	0.01 m
Insulation Thermal Conductivity	0.5 W/(m.K)

Table 3.4: Surrounding Fluid Properties

Velocity	0.048 m/s
Density	1026 kg/m^3
Dynamic Viscosity	0.00182 Pa.s
Specific Heat Capacity	420 J/(kg.K)
Temperature	277 K
Thermal Conductivity	0.56 W/(m.K)

Table 3.5: Hydraulic and Thermal Boundary Conditions

Inlet Temperature	300 K
Inlet Flow Rate	Stepped from 0 to 5e-3 m^3/s at t= 200 s
Outlet Pressure	1e7 Pa
GVF	40%

The gas and liquid properties for each pressure and temperature conditions are determined using a PVT file as described in section 3.4. A one-mode approximation of the transfer functions in (2.12) is considered.

3.5.1. Effect of the Gas Volume Fraction (GVF) Level

The GVF level is increased from 0% (single-phase flow liquid) to 40% to study its impact on the mixture dynamics. Given in Table 3.6 are respectively the equivalent fluid density, bulk modulus, dynamic viscosity, speed of sound, natural frequency and damping ratio for the considered GVF levels.

Table 3.6: Effect of the Gas Volume Fraction Level on the Equivalent Fluid Properties

GVF (%)	ρ_{eq} (Kg/m^3)	β_{eq} (Pa)	μ_{eq} (Pa.s)	c_{eq} (m/s)	ω_n	ξ
0	835.52	1.22e9	0.023	1212.35	0.577	0.189
20	827.42	4.207e8	0.019	713.064	0.334	0.264
40	717.17	4.84e7	0.013	259.95	0.118	0.5201

It is shown by Table 3.6 that adding gas into the two-phase flow system results in a lower equivalent fluid density and a lower equivalent bulk modulus. However, the effect of the reduction in the bulk modulus is predominant, especially at low GVF levels, due to the use of the GVF-weighted parallel combination in (2.41). This results in a significantly lower equivalent speed of sound and consequently a lower system natural frequency and higher damping ratio. In addition, the introduction of a higher gas flow rate results in a lower equivalent dynamic viscosity, specifically at higher GVF levels leading to a lower steady-state pressure drop. Shown in Figure 3.8 is the normalized inlet pressure transient response (P_{in} / P_{out}) due to a step in the inlet flow rate (Table 3.5) for a GVF equal to 0, 20, and 40%.

It is noticed, from Figure 3.8, that increasing the GVF level results in higher period of oscillation due to the lower system natural frequency and higher damping. The increase in the system damping will result also in a significant reduction in the pressure overshoot. This simulation confirms that increasing the GVF while keeping the same total flow rate leads to a lower steady-state pressure drop in the pipeline due to a lower equivalent fluid dynamic viscosity. Those conclusions are in accordance with what has been observed in Chapter 2.

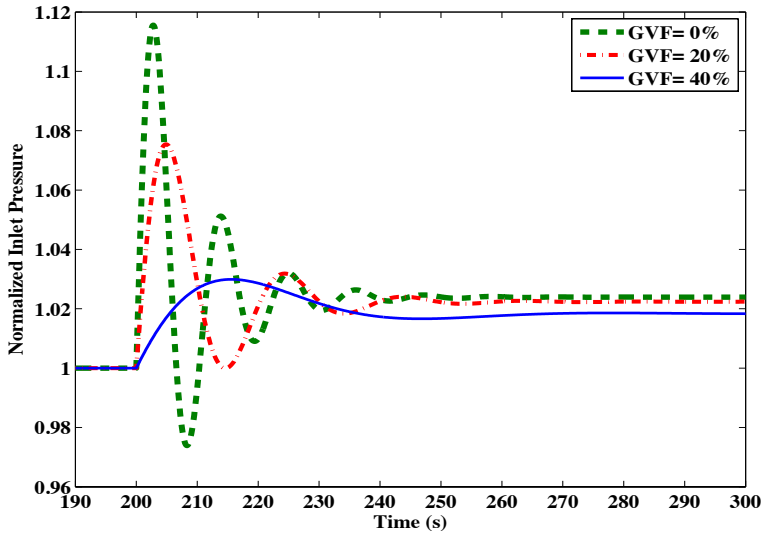

Figure 3.8: Inlet Pressure Time Response to Inlet Flow Rate Step for Different GVF

3.5.2. Effect of the Inlet Temperature

The inlet fluid temperature is increased from 290 to 310 K. Given in Table 3.7 are the equivalent fluid properties, the fluid-thermal system natural frequency and damping ratio.

Table 3.7: Effect of the Inlet Temperature on the Equivalent Fluid Properties

T_{in} (K)	ρ_{eq} (Kg/m^3)	β_{eq} (Pa)	μ_{eq} (Pa.s)	c_{eq} (m/s)	ω_n	ξ
290	718.58	4.76e7	0.016	257.91	0.116	0.527
300	717.17	4.84e7	0.013	259.95	0.118	0.5201
310	716.64	4.92e7	0.011	261.89	0.119	0.515

The equivalent fluid density and bulk modulus are not sensitive to fluid temperature within the considered range (less than 1% relative change) leading to similar system natural frequency and damping ratio. However, a substantial reduction in the equivalent fluid dynamic viscosity (around 45% relative change) is noticed when varying the inlet temperature inducing a reduction in the steady state pressure drop. Shown in Figure 3.9 is the normalized inlet pressure transient response due to a step in the inlet flow rate for fluid inlet temperatures equal to 290, 300 and 310K.

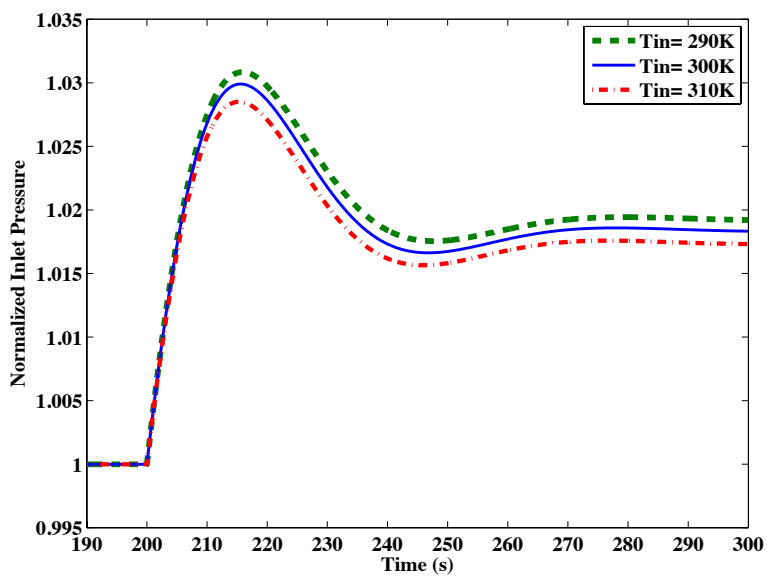

Figure 3.9: Inlet Pressure Time Response to Inlet Flow Rate Step for Different Inlet Temperatures

The variation in the fluid inlet temperature results in a similar mixture pressure dynamic response (similar period of oscillation, percent overshoot and settling time).

This observation is in accordance with the conclusions drawn from Table 3.7 (similar mixture natural frequency and damping ratio). However, the temperature variation affects the steady state pressure drop due to the change in the equivalent fluid dynamic viscosity.

3.5.3. Effect of the Outlet Pressure

The pipeline outlet pressure is varied from 1e7 to 2e7 Pa. Shown in Table 3.8 the equivalent fluid properties, the mixture natural frequency and damping ratio for the studied pressure values.

Table 3.8: Effect of the Outlet Pressure on the Equivalent Fluid Properties

P_{out} (Pa)	ρ_{eq} (Kg/m^3)	β_{eq} (Pa)	μ_{eq} (Pa.s)	c_{eq} (m/s)	ω_n	ξ
1e7	717.17	4.84e7	0.013	259.95	0.118	0.5201
1.5e7	721.19	9.015e7	0.0101	353.42	0.164	0.425
2e7	726.66	1.59e8	0.0088	469.054	0.222	0.363

It is shown from Table 3.8 that the increase in the pipeline pressure conditions results in a significant increase in the equivalent fluid density and bulk modulus due to the effect of the fluids compressibility. Similar to the case of the change in the GVF levels, the effect of the increase in the equivalent bulk modulus is predominant, leading to a higher natural frequency and lower damping ratio. In addition, the increase in the pipeline outlet pressure induces a slight reduction in the fluids viscosity leading to a lower steady-state pressure gradient.

Presented in Figure 3.10 is the normalized inlet pressure transient response for the different outlet pressures discussed in Table 3.8. The increase in the system natural frequency associated with lower damping ratios due to the increase in the pipeline's pressure level induces a more oscillating pressure at the pipeline inlet.

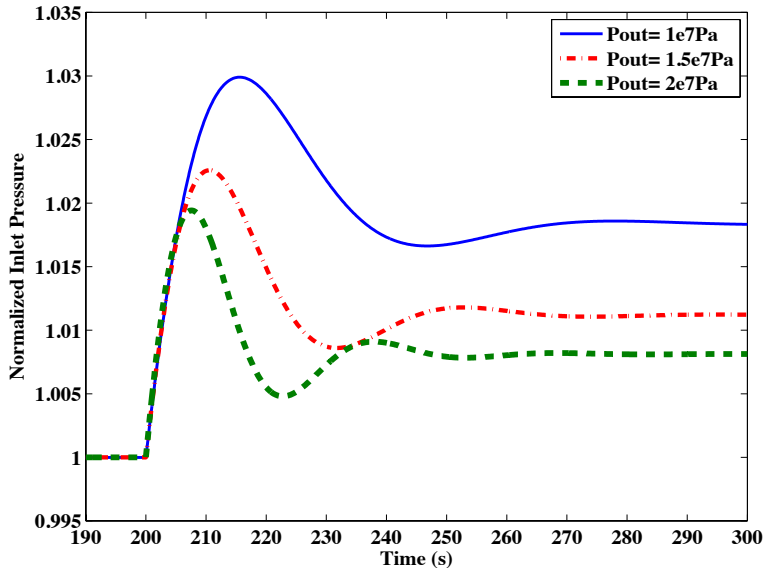

Figure 3.10: Inlet Pressure Time Response to Inlet Flow Rate Step for Different Outlet Pressures

3.5.4. Effect of the Hyperbolic Functions Approximation Order

Shown in Figure 3.11 is the normalized inlet transient pressure for different truncation orders of the transfer functions in (2.12). Increasing the number of modes in (2.12) enables a more accurate approximation of the hyperbolic transfer functions by including the higher order pipeline mixture dynamics. This will translate, in the time domain, into a more oscillating transient pressure. Although using a higher number of modes results in a more accurate and realistic estimation of the pressure and flow dynamic response, it will lead to a higher computational time (Chapter 2).

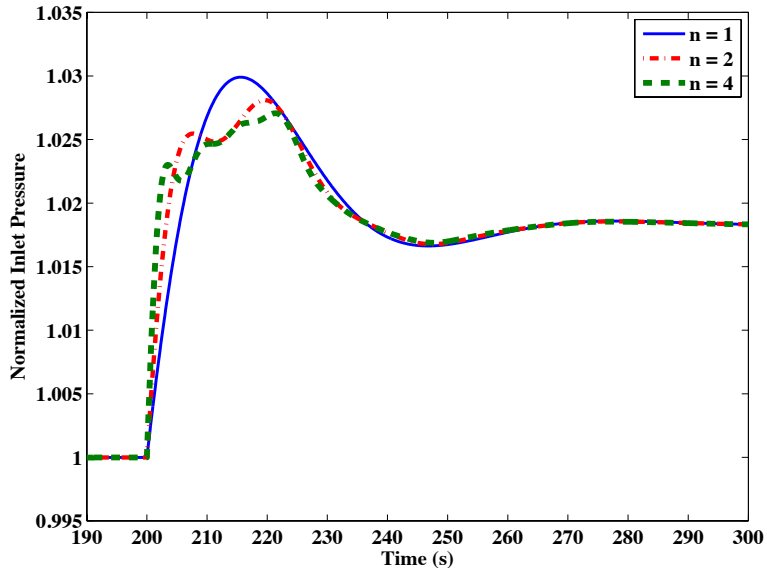

Figure 3.11: Inlet Pressure Time Response to Inlet Flow Rate Step for Number of Modes

3.5.5. Effect of the Number of Pipe Segments

In this section the pipeline is divided into a different number of equal-length segments along its axis. The pipeline segments are linked following the schematic in Figure 3.3 to ensure the causality of the system. Given in Figure 3.12 are the pressure and temperature profile considering one, two and four pipeline segments.

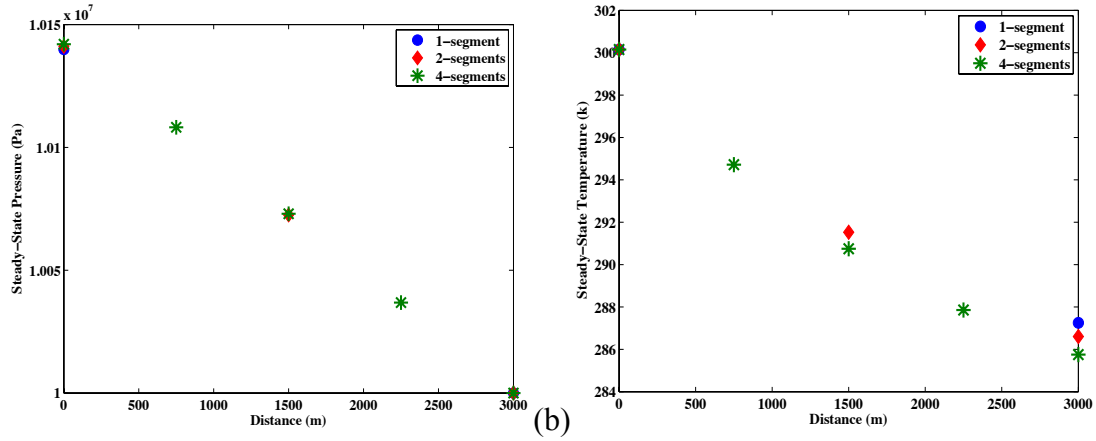

Figure 3.12: Effect of the Number of Pipeline Segments: (a) Steady-State Pressure Profile, (b) Steady-State Fluid Temperature Profile

The pipeline segmentation enables the prediction of the fluid pressure and temperature along the pipeline axis. This result can be used to determine not only if the pipeline can be subject to hydrate or wax formation, but also the location of the blockage. This feature enables the model users to adopt an affective inhibition strategy by protecting only a section of the pipeline. The pressure and temperature profile are also used to generate a more accurate estimation of the liquid and gas properties via the two-phase PVT file (Figure 3.1) and therefore a more accurate estimation of the equivalent fluid parameters along the pipeline.

Given in Figure 3.13 are the equivalent fluid properties profile distributions for the different considered number of segments. As the distance from the pipeline inlet increases, the mixture pressure drops due to the friction effects and the fluid temperature decreases due to the heat loss from the hot fluids into the cooler environment. This phenomenon has different effects on the fluids properties. While the pressure loss along the pipelines results in lower liquid and gas densities (Table 3.8), the temperature leads to higher densities (Table 3.7). However, the effect of the pressure is prevalent for the studied case leading to a lower equivalent fluid density (Figure 3.13(a)). It is shown in Figure 3.13(b) that the equivalent fluid viscosity will increase considerably along the pipeline driven by the reduction in the fluid temperature. As demonstrated in Tables 3.7 and 3.8, it is confirmed by analyzing Figure 3.13(c) that the decrease in the pressure and temperature leads to a lower equivalent bulk modulus resulting in a higher fluid compressibility as we get farther from the pipeline's inlet. Finally, as previously discussed, the effect of the bulk modulus reduction overcomes the reduction in the

equivalent fluid density leading to a slightly lower equivalent speed of sound (Figure 3.13 (d)).

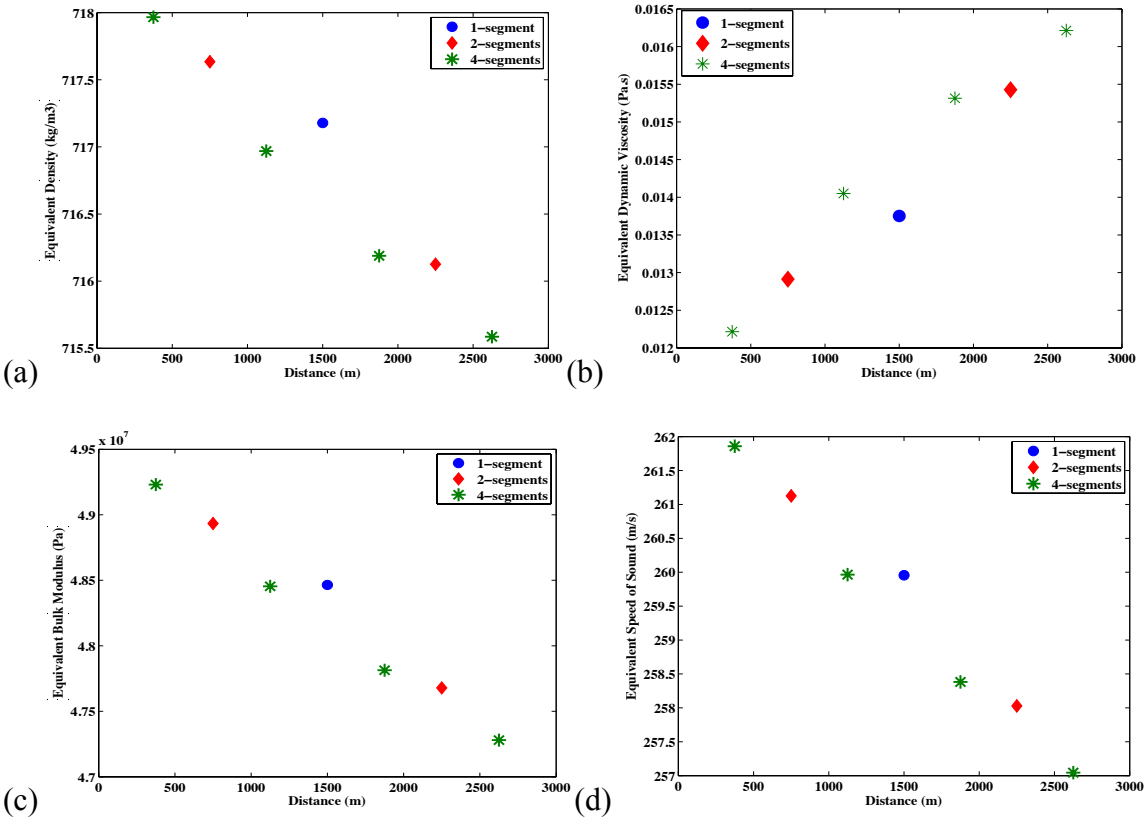

Figure 3.13: Equivalent Fluid Properties Profile: (a) Equivalent Density, (b) Equivalent Dynamic Viscosity, (c) Equivalent Bulk Modulus, and (d) Equivalent Speed of Sound

To evaluate the effect of the pipe segmentation on its dynamic response, the base case simulation was carried out using one, two and four segments. Presented in Figure 3.14 is the normalized transient pressure at the pipeline inlet. Note that a one-mode approximation of the exact hyperbolic transfer functions is adopted for all the cases simulated in Figure 3.14.

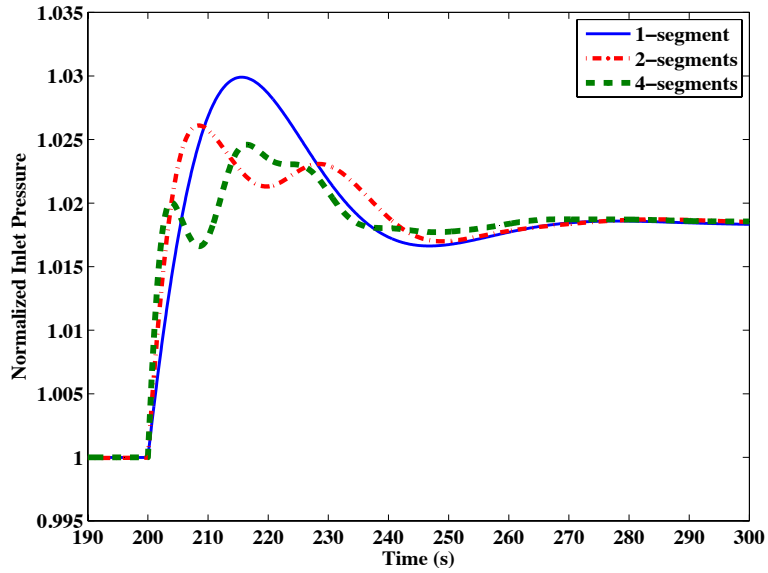

Figure 3.14: Inlet Pressure Time Response to Inlet Flow Rate Step for Different Number of Segments

The increase in the number of pipeline segments used in the simulations results in a more dynamic pressure response. This can be explained by the decrease in the segments length leading to higher natural frequencies of their corresponding transfer functions. Although a one-mode approximation of the transfer functions is considered, the model is able to capture the higher order dynamics similarly to the use of a higher truncation order; thanks to the coupling of the smaller segments and a more accurate estimation of the fluid characteristics distribution along the pipeline.

The normalized pressure is monitored at different locations along the pipeline using four segments (Fig 3.15). It is shown that the pressure at the pipeline inlet (location of the step in the flow rate) is characterized by higher frequency oscillations and a higher overshoot. Those oscillations will be damped as we move closer to the pipeline outlet, characterized by a constant pressure boundary condition.

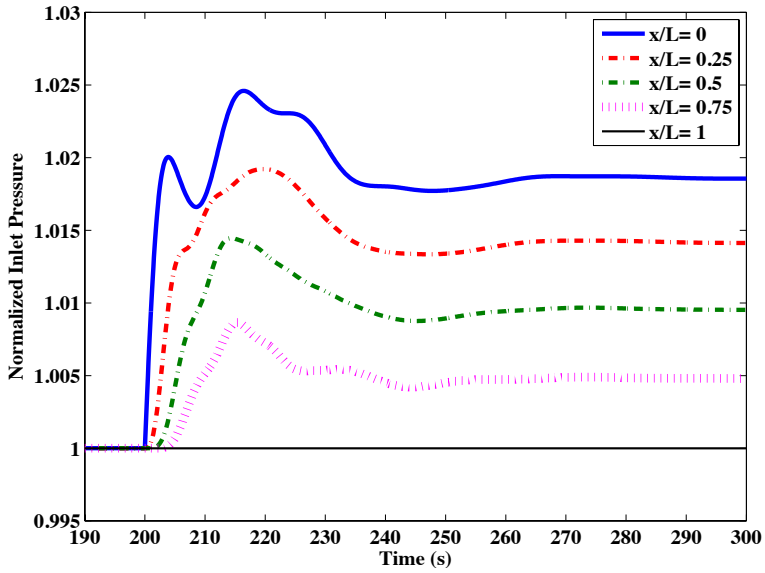

Figure 3.15: Transient Inlet Pressure along the Pipeline (4 segments)

It is also noticed that the model was able to capture the time delay in the pressure response as the distance from the pipeline's inlet increases. The pipeline segmentation enables a considerable improvement in the model estimation capabilities. However, similarly to the use of a higher hyperbolic functions truncation order, the increase in the number of segments will result in a higher computational cost.

Given in Figure 3.16 are the computation time and the mean squared error as a function of the number of pipeline's segments for the base case. Note that a one-mode approximation is considered for the studied cases while a 20-mode approximation with ten segments is used as a baseline.

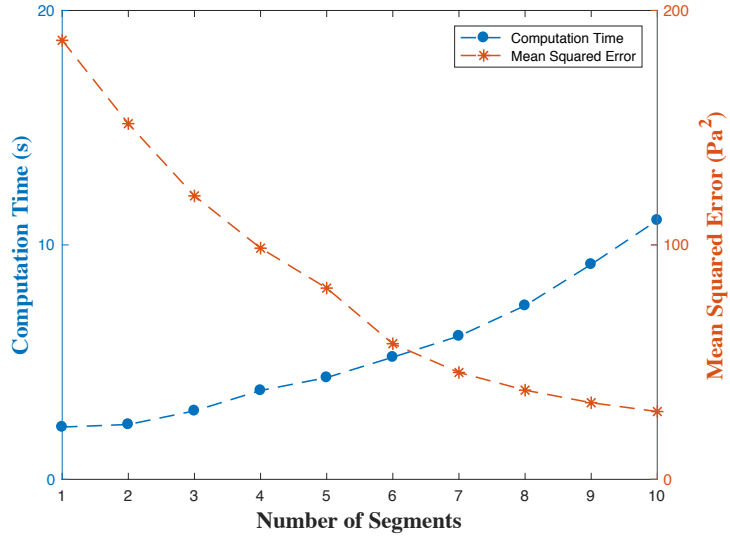

Figure 3.16: Computation Time vs. Mean Squares Error

As the number of pipelines segments is increased, the mean squared error drops quickly at the beginning while the computation time undergoes a low increase. This tendency is inverted when considering the higher number of segments where the computation time increases dramatically without a noticeable improve in the model accuracy. Hence, it is crucial to select the suitable number of pipe segments depending on the desired model application and available computing power. This type of study can be performed to evaluate the maximum number of segments that can be used not to exceed a required simulation time for the real time monitoring of the pipeline's dynamics or the minimum number of segments that should be considered to achieve a certain degree of accuracy and reliability in the design of safety equipment [106, 107].

3.5.6. Effect of the Transient Thermal Module

The base case parameters given in Tables 3.3-3.5 are used to evaluate the effect of the transient thermal model on the pipeline's dynamic response. To simulate startup conditions, the inlet flow rate is stepped at t= 200s from 0 to 5e-3 m3/s at a constant

temperature (350K) while keeping a fixed outlet pressure (1e7 Pa). A steady state coupling of the hydraulic and thermal module is first used to generate the inlet pressure and outlet temperature. The proposed transient thermal module is then enabled to assess the effect of transient heat transfer on the pressure and temperature flow conditions. Given in Figure 3.17 are the pressure and temperature predicted using the steady-state and transient Heat Transfer (HT) models.

It can be noticed from Figure 3.17 that both the transient and steady-state thermal models lead to the same steady-state pressure and temperature conditions, However, unlike the model with steady state heat transfer, characterized by very fast pressure transients (50s settling time), the full transient multi-physics model is characterized by significantly slower pressure and temperature transients (1500 s settling time). This feature is very important, especially when designing pumps for start up conditions or calculate the cool down time for shut down conditions. In Figure 3.17(a), the transient inlet pressure predicted by the full transient model is considerably higher than the one simulated using the steady-state HT model.

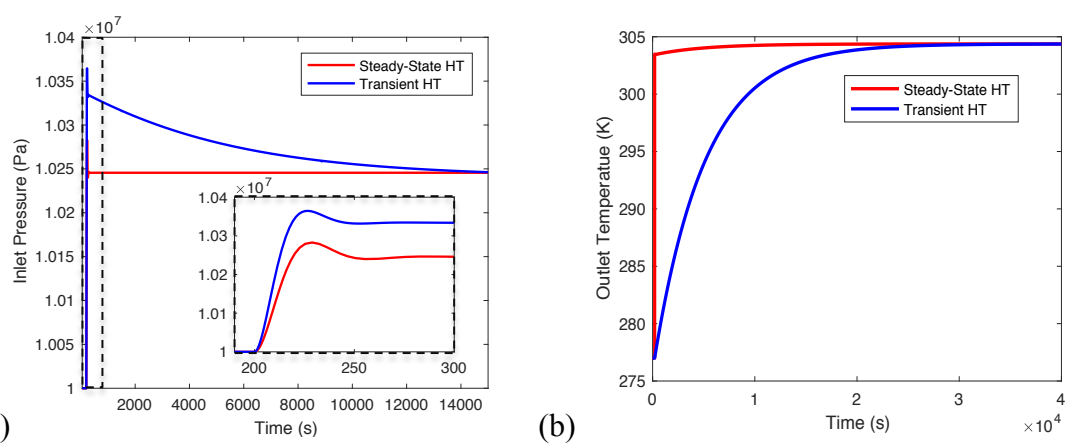

Figure 3.17: (a) Inlet Pressure, and (b) Outlet Temperature

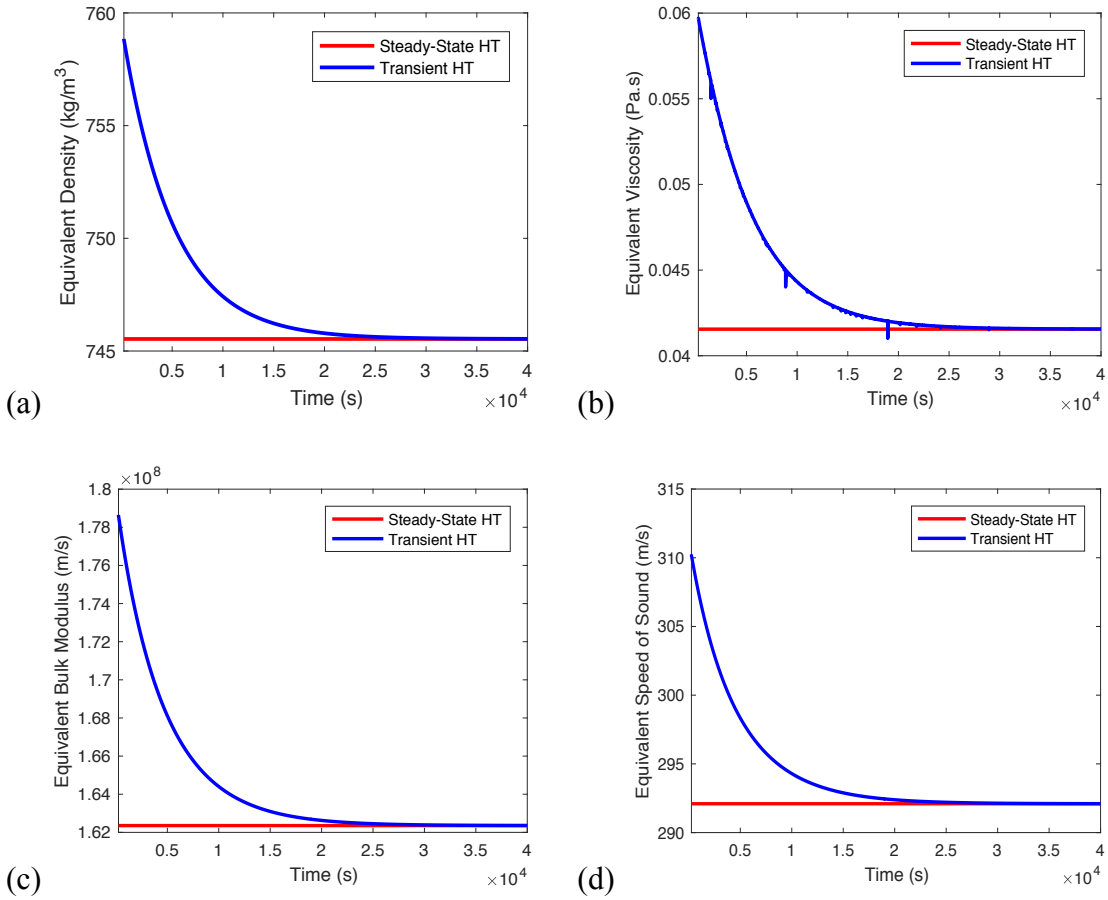

Figure 3.18: Equivalent Fluid Properties Transients: (a) Equivalent Density, (b) Equivalent Dynamic Viscosity, (c) Equivalent Bulk Modulus, and (d) Equivalent Speed of Sound

To understand in more details the effect of the transient temperature variations on the pipeline dynamic response, the equivalent fluid properties calculated by the steady-state and transient HT models are given in Figure 3.18.

The equivalent fluid properties given by the steady-state HT model are constant after the step in the flow rate due to a constant fluid temperature (Figure 3.17 (b)). In contrast, the equivalent fluid properties given by the transient HT model gradually decrease to reach their steady state values as the fluid temperature increases from the ambient temperature (277k), at shut down condition, to 304 K at flowing condition. The

equivalent fluid dynamic viscosity is highly dependent on the temperature conditions. A lower temperature at the beginning of the simulation will therefore result in significantly higher fluids viscosity predicted by the multiphysics integration module (Figure 3.18 (b)) and therefore a higher and more damped inlet pressure (Figure 3.17 (a)). On the other hand the equivalent speed of sound (Figure 3.18 (d)) is not affected considerably by the transient temperature variations leading to a similar pressure oscillation frequency (Figure 3.17 (a)).

3.6. Conclusion

In this chapter, a multi-physics low-dimensional reduced-order model for liquid-gas two-phase flow transients in pipelines is proposed. A hybrid approach is used where empirical and physics-based mathematical models were developed to capture the hydraulic and thermal behavior of steady-state and transient two-phase flow in pipelines. First, the pipeline is divided into different segments. A two-phase steady-state hydraulic model is coupled with a thermal model using a multiphysics integration block that estimates the fluid properties as a function of the pressure and temperature conditions. The equivalent fluid properties are then derived based on the GVF level and used to construct the pipeline two-phase flow dynamic model. A transient two-phase flow module is also implemented to simulate startup or shutdown conditions. A parametric study is conducted to verify the model and understand the correlation between all system parameters and variables (i.e. pipeline/fluid properties and operating conditions).

The accuracy of each component of the proposed multi-physics model has been investigated in Chapters 2 and 3 by comparing the model components predictions with experimental data. However, the overall model performance is yet to be evaluated.

Chapter 4 of this dissertation is intended to compare the developed low-D model to both commercial package simulations and transient experimental data to assess its degree of accuracy.

Chapter 4

Model Comparison

4.1. Introduction

In Chapter 2 of this dissertation, a low-dimensional approach for transient two-phase in pipelines has been proposed. This approach is based on coupling the mechanistic steady state model in [50] with the single-phase flow pipeline distributed parameter model in [17] through the derivation of equivalent fluid properties. In Chapter 3, the developed low-D model was integrated with a two-phase flow heat transfer model to account for the effect of the temperature variation on the fluid properties and the pipeline's dynamic response.

Each component of the models described previously has been validated against an independent experimental dataset or the prediction of a published numerical model. However, the overall performance of the presented model is yet to be assessed.

In this chapter, the low-D model predictions are first compared to, OLGA, a commercial multiphase flow dynamic simulator. The developed model's prediction and the commercial software simulations are then compared to experimental data for different GVF levels.

4.2. Comparison to OLGA

In this section, the developed low-dimensional model is compared to OLGA, one of the leading commercial codes used in the oil and gas industry. OLGA is based on a three-fluid model. Five continuity equations are used: Three equations for the gas, oil and

water phases, and two equations for the oil and water droplets. Three momentum equations are considered, one for the oil; one for the water; and one for the combination of the gas with liquid droplets. Assuming that all phases are at the same temperature, one mixture energy equation is also solved. This results in a system of nine conservation equations and one equation of state to be solved.

Depending on the complexity of the problem and the required accuracy, an appropriate time-step and special discretization of the pipeline should be considered which might present some instability problems of the numerical scheme. On the other hand, the developed low-dimensional model does not require a spatial discretization of the pipeline allowing the use of higher time-steps without encountering any stability issue. This characteristic makes the low-D model equally suited for simulating the slow transient encountered in the oil and gas industry during the production phase or fast transient such as water hammer generated by a rapid valve closure. Two classes of flow regimes are considered by the OLGA model; distributed flow comprised of bubble and slug flow, and separated flow grouping stratified and annular-mist flow. As explained in section 2.3, the two-phase low-dimensional model recognizes seven flow regimes.

4.2.1. Single-Phase Flow

First, the case of single-phase flow is considered for laminar and turbulent flow conditions. The pipeline characteristics, fluid properties and flow conditions are given respectively in Tables 4.1-4.3.

Table 4.1: Pipe characteristics

	Pipe Length	Pipe Diameter	Pipe Roughness	Pipe Inclination
Laminar	457.2 m	0.0257 m	3.32E-06 m	0°
Turbulent	457.2 m	0.1402 m	3.32E-06 m	0°

Table 4.2: Fluid Properties

	Liquid Density	Liquid Viscosity	Liquid Bulk Modulus
Laminar	927.44 Kg/m^3	0.00784 Pa.s	1.6E9 Pa
Turbulent	904.96 Kg/m^3	0.01927 Pa.s	1.6E9 Pa

Table 4.3: Flow Conditions

	Outlet Pressure	Inlet Flow Rate
Laminar	1.0342e+7 Pa	Stepped from 0 to 15.87 E-5 m^3/s at t = 200 s
Turbulent	1.7237e+7 Pa	Stepped from 0 to 0.0827 m^3/s at t = 200 s

A specific pressure level was maintained at the outlet of the pipeline while the inlet flow rate was stepped at 200 seconds. Shown in Figure 4.1 is a comparison between the inlet pressure time response given by OLGA assuming isothermal conditions and the low-dimensional model for different truncation orders of the hyperbolic transfer functions in (34) for laminar and turbulent flow conditions.

The single-phase dissipative distributed parameter model is based on solving the Navier-Stokes equations assuming a non-turbulent mean flow, Mach number much less than unity, a high length to diameter ratio, and a low normalized density variation. This model has been experimentally validated in [66-68]. The dissipative model has been extended to model turbulent flow conditions and experimentally validated in [108]. This part will therefore serve assessing the accuracy of OLGA in modeling transient single-phase flow.

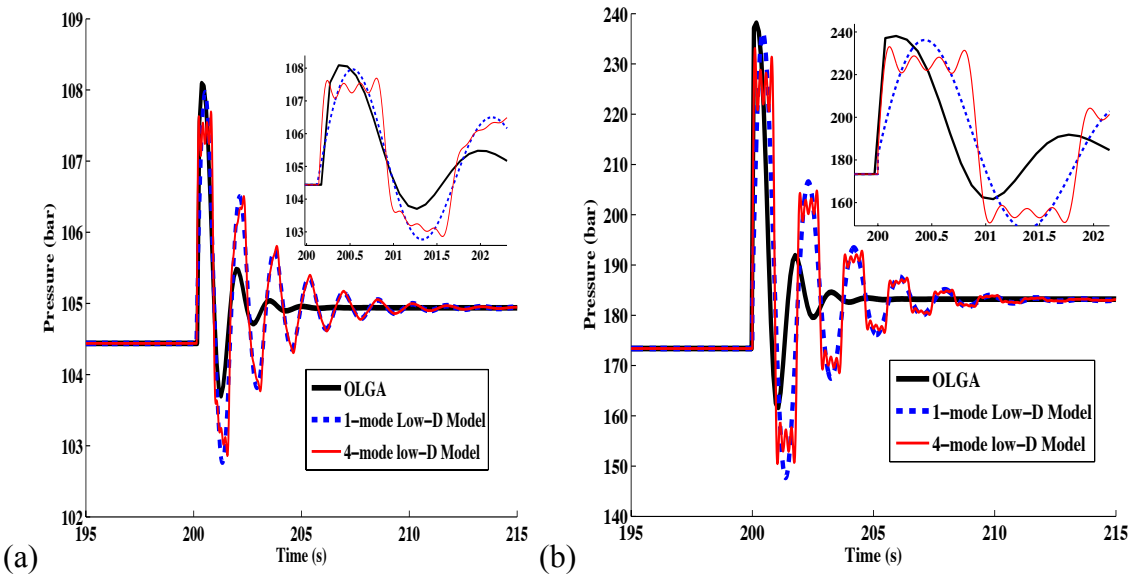

Figure 4.1: Inlet Pressure Time Response to Inlet Flow Rate Step: (a) Laminar Flow, (b) Turbulent Flow

As shown in Figure 4.1, the OLGA simulations and the low-dimensional model show a perfect match of the steady-state pressure for the laminar and turbulent flow conditions with a relative absolute error respectively of 0.0043% and 0.81%. Furthermore, the pressure response given by the two models have similar period of oscillations. On the other hand, although the general behavior of the inlet pressure over time is similar, the overshoot values and the settling time present a discrepancy between the two models. This can be explained by a difference in the estimation of the system's damping between OLGA and the low-D model. Since, the response given by OLGA is also closer to the one given by the one mode approximation of the hyperbolic functions, it is believed that OLGA does not capture the higher order dynamics. Shown in Figure 4.2 is the frequency response given by the two models. It is noticed that the two models have a good agreement in the estimation of the system natural frequency (Table 4.8).

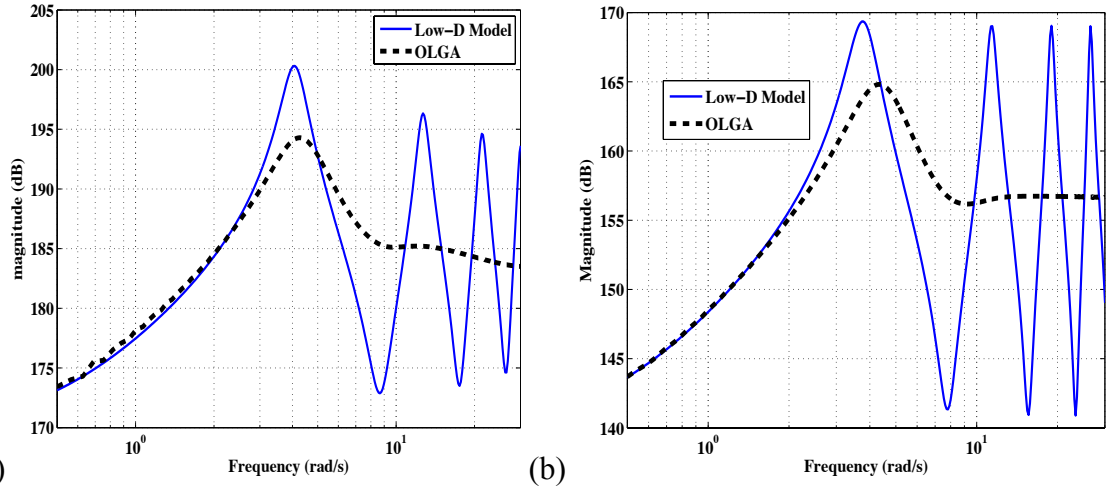

Figure 4.2: Frequency Response of the TF Relating Pin to Qin: (a) Laminar Flow, (b) Turbulent Flow

4.2.2. Two-Phase Flow

In this section, the developed low-dimensional model will be compared to OLGA for different GVF values. These latter were chosen from the Stanford multiphase flow database such as the mechanistic model in [50] allows a good prediction of the steady-state pressure gradient and liquid holdup. This was essential since the equivalent fluid properties are expressed in terms of the phases properties, weighted by the mechanistic model outputs. Shown in Table 4.4 is a comparison between the steady state prediction of the flow pattern, the liquid holdup and the pressure gradient of OLGA and the low-D model.

Table 4.4: Steady-State Models Accuracy

	Flow Pattern			Relative Absolute Error (Liquid Holdup)		Relative Absolute Error (Pressure Gradient)	
GVF	Experimental	OLGA	Low-D Model	OLGA	Low-D Model	OLGA	Low-D Model
10%	Elongated-Bubble	Bubble	Elongated -Bubble	0.74%	0.71%	13.83%	1.62%
20%	Elongated-Bubble	Bubble	Elongated -Bubble	0.79%	0.56%	15.66%	1.10%
30%	Slug	Slug	Slug	3.39%	2.47%	0.96%	0.93%
50%	Slug	Slug	Slug	2.21%	1.78%	4.92%	4.46%

As shown in Table 4.4, the low-D model is able to accurately predict the correct flow pattern while OLGA could not predict the elongated-bubble flow due to its limitation on the considered flow patterns. The low-D model gives also a very good prediction of the liquid holdup and the pressure gradient allowing an accurate estimation of the equivalent fluid properties while the OLGA model presents in some cases a relatively large error, which may affect the resulting pipeline's dynamics. The pipe characteristics, flow conditions, as well as the phases properties used for the simulations are given in Tables 4.5-4.7.

Table 4.5: Pipe Characteristics

Pipe Length	Pipe Diameter	Pipe Roughness	Pipe Inclination
457.2 m	0.1402 m	3.32E-06 m	0°

Table 4.6: Fluid Properties

GVF	Liquid Density	Liquid Viscosity	Liquid Bulk Modulus	Surface Tension	Gas Density	Gas Viscosity	Gas Bulk Modulus
10%	904.96 Kg/m^3	0.01927 Pa.s	1.6E9 Pa	0.03 N/m	1.6722 Kg/m^3	1.8E-5 Pa.s	1.72E7 Pa
20%	904.96 Kg/m^3	0.01909 Pa.s	1.6E9 Pa	0.03 N/m	1.7149 Kg/m^3	1.9E-5 Pa.s	1.72E7 Pa
30%	904.96 Kg/m^3	0.01972 Pa.s	1.6E9 Pa	0.03 N/m	1.3719 Kg/m^3	1.8E-5 Pa.s	1.72E7 Pa
50%	813.64 Kg/m^3	0.0024 Pa.s	1.6E9 Pa	0.027 N/m	1.4833 Kg/m^3	1.8E-5 Pa.s	1.72E7 Pa

Table 4.7: Flow Conditions

GVF	Outlet Pressure	Liquid Superficial Velocity	Gas Superficial Velocity
10%	1.7237E+7 Pa	5.36 m/s	0.42 m/s
20%	1.7237E+7 Pa	5.26 m/s	1.29 m/s
30%	1.7237E+7 Pa	2.53 m/s	1.68 m/s
50%	1.7237E+7 Pa	3.17 m/s	4.03 m/s

Similarly to the case of single-phase flow, a fixed pressure level was maintained at the outlet of the pipeline while the inlet flow rate was stepped at 200 seconds to achieve the desired gas and liquid superficial velocities. Detailed in Table 4.8 is the natural frequency of the first mode given by the Low-D model and the OLGA model for the different simulated cases.

Table 4.8: System Natural Frequency Estimation

	Liquid-Laminar	Liquid-Turbulent	10% GVF	20% GVF	30% GVF
Low-D Model	3.73 rad/s	4.098 rad/s	2.12 rad/s	1.87 rad/s	0.95 rad/s
OLGA	4.33 rad/s	4.21 rad/s	2.4 rad/s	2.056 rad/s	1.14 rad/s

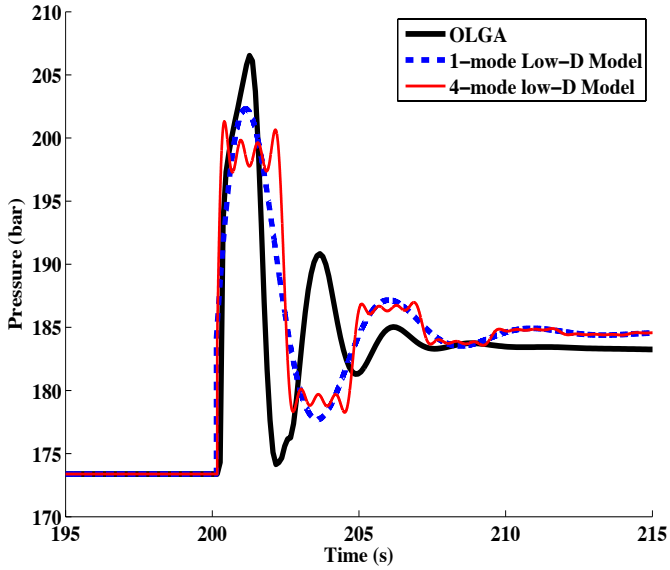

Figure 4.3: Inlet Pressure Time Response to Inlet Flow Rate Step for 10% GVF

Shown in Figures 4.3-4.6 is a comparison between the inlet pressure time responses given by OLGA assuming isothermal conditions and the low-dimensional model using different truncation orders for different GVF levels.

As demonstrated in section 2.5, introducing gas into the pipeline results in a dramatic decrease of the equivalent bulk modulus due to the GVF-weighted parallel combination of the gas and liquid bulk moduli. This effect leads to a lower equivalent speed of sound and therefore lower natural frequencies (Table 4.8), resulting in higher period of oscillation. Comparing Figures 4.1(b) and 4.3 shows that this phenomenon was equally captured by the OLGA simulation and the low-D model. In addition, the presence of gas results in a lower steady-state pressure drop when compared to the case of single-phase flow due to a lower equivalent viscosity. Although this effect is present in the results given by the two models, the inlet pressure response given by the OLGA simulations at a GVF of 10 % has an absolute relative error of 13.83% at steady-state

when compared to the Stanford multiphase flow database, while the low-dimensional model presents an error of 1.62% (Table 4.4). Figure 4.3 shows also that the 10% GVF simulation is characterized by a lower overshoot and a lower settling time compared to Figure 4.1(b). However, similarly to the case of single-phase flow, the overshoot values and the settling time present a discrepancy between the two models indicating different damping ratios.

The inlet pressure time response of a 20% GVF system, given in Figure 4.4, show a similar trend compared to the one given by a 10% GVF system (Figure 4.3) for both models. This can be explained by the increase in the gas superficial velocity while keeping a similar liquid superficial velocity, which cancels the effect of the increase in GVF on the natural frequency and the damping ratio. As highlighted in Table 4.4, the 20% GVF OLGA simulation has an error of 15.66% in the estimation of the steady-state pressure gradient, while the error of the low-dimensional model is only 1.1%.

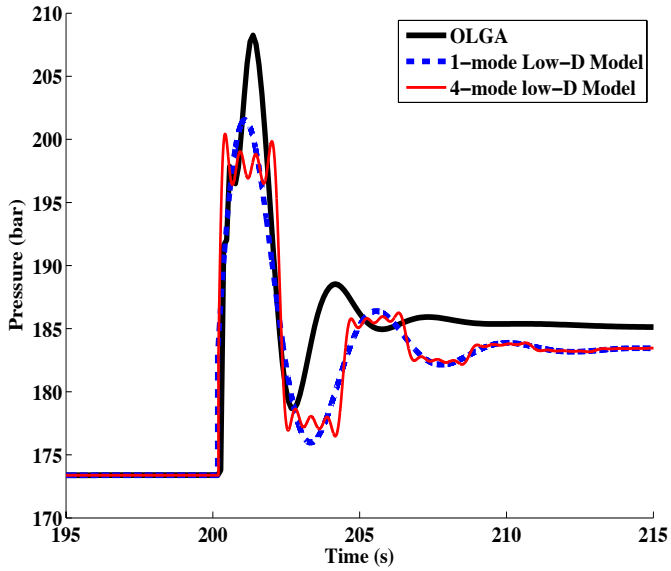

Figure 4.4: Inlet Pressure Time Response to Inlet Flow Rate Step for 20% GVF

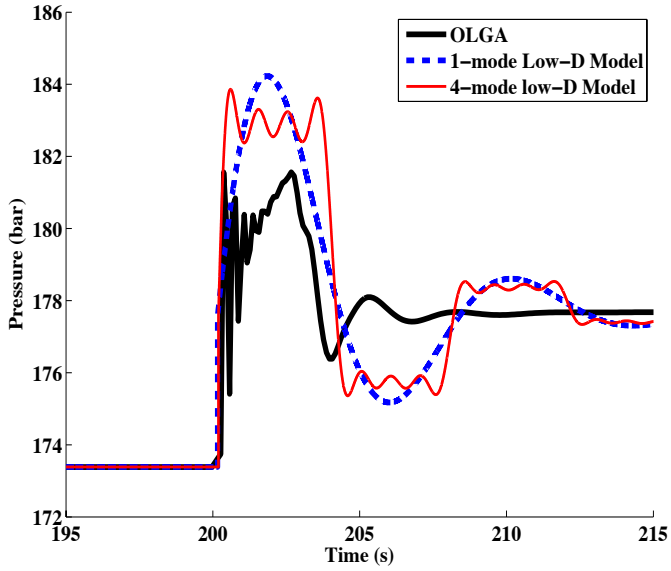

Figure 4.5: Inlet Pressure Time Response to Inlet Flow Rate Step for 30% GVF

The Inlet pressure time responses given by OLGA and the low-D model for a 30% GVF system are characterized by longer periods of oscillations associated with lower overshoot values and longer setteling time compared to the 10 and 20% GVf simulations due to the increase in the amount of gas. However, although both models were able to predict the existance of slug flow within the pipeline, the resuling pressure responses do not present the severe fluctuations typical of slug flow conditions but only predict the change in average pressure. It is believed that the chattering of the pressure in the first oscillation of the OLGA similation following the step in the flow rate is attributed to a numerical instability problem rather than the effect of slug flow or the inclusion of higher order dynamics as this phenomenon dies out.

To summarize, the inlet pressure response given by the OLGA simulations at GVF of 10 and 20% present high relative absolute error at steady-state when compared to the Stanford Multiphase Flow Database and the Low-D model. This error decreases

considerably for a GVF of 30. Similarly to the case of the single-phase flow, the low-D and OLGA models show a good agreement of the period of oscillations for all the considered GVF levels indicating similar estimations of the natural frequencies (Table 4.8). However, the two models present an important disagreement in the overshoot values and the settling time which can be explained by the difference the liquid holdup estimation resulting in different fluids and interfacial friction factors and consequently different damping ratios. It is also noticed that the OLGA Simulation results are closer to the ones of a one-mode approximation of the hyperbolic functions in (2.12) for all the considered GVF levels indicating that OLGA does not capture the higher order dynamics. In absence of experimental transient data, it is difficult to accurately evaluate the validity of both models.

4.3. Experimental Validation

4.3.1. Experimental Facility, Instrumentation and Data Acquisition

The experimental results presented in this dissertation were collected on the Multiphase Flow Loop Facility located in the Department Of Mechanical Engineering at National University of Singapore.

This Three-Phase, Oil-Water-Air, Flow Loop Test Facility is a multi-purpose test facility that can be used to test multiphase equipment, e.g. pipelines, separators, multiphase flow meters, multiphase pumps, etc. Schematic views and pictures of the facility are presented in Figure 4.6.

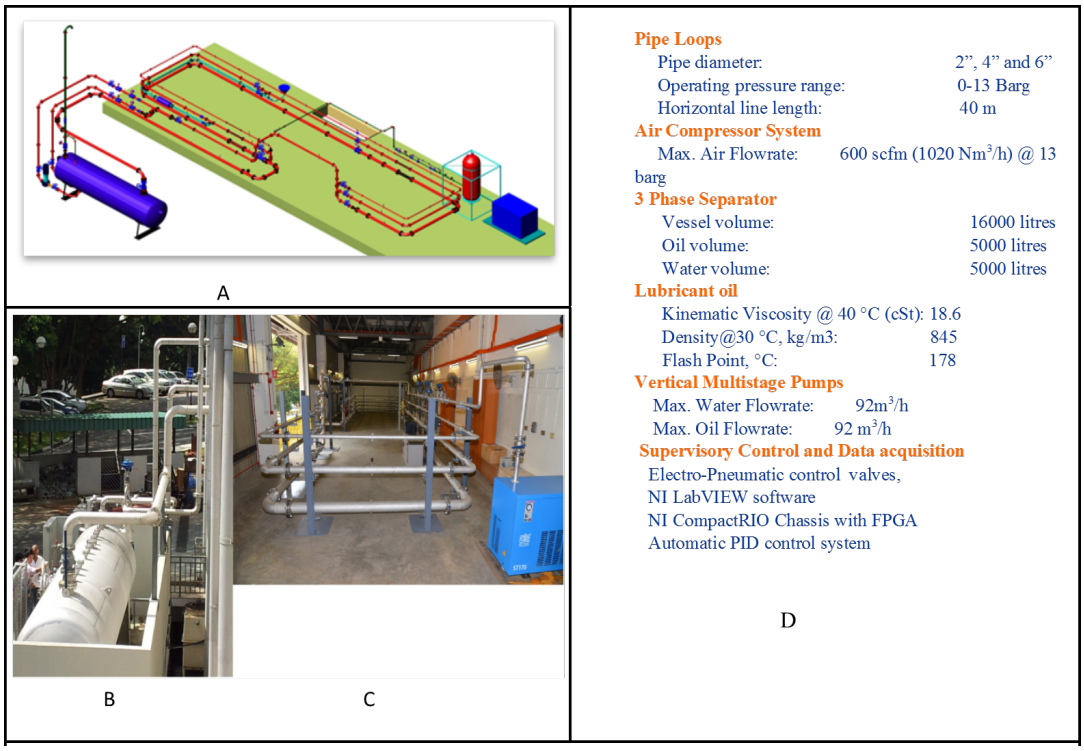

Figure 4.6: Schematic views and pictures of the experimental setup: A) Full 3d view, B) Separator tank, C) Pipe flow loops, D) Specifications.

In this facility, multiphase flow is achieved by mixing known quantities of air, oil and water. Before being mixed, the respective phases are measured separately. The metering section and the test flow loops are located indoors, whereas the separator is located outdoors. The multiphase flow loop test facility in NUS is rated at 13 barg. The flow loops are built in a modular fashion from 3 m sections of seamless stainless steel pipes, schedule 10, which can be interchanged.

The Three-phase flow facility is fully automatically controlled. This involves both hardware and software. In terms of hardware, a compactRIO main chassis is employed. The compactRIO is a rugged, embedded controller system supplied by National Instruments. It consists of a Real-time processor, a reconfigurable Field Programmable Gate Array (FPGA) and the IO modules. It is connected to the Host PC with an Ethernet

cable. In terms of software, a supervisory control and data acquisition (SCADA) program has been developed in the software LabVIEW. Since the facility is being also used as a reference to test the performance of third party multiphase flow meters, the flow meters of air (vortex) and liquid (Coriolis) have been optimized for accuracy.

Air is supplied by two compressors connected in parallel to a receiver tank. An air drier is used to remove humidity from the air before it is measured. In order to measure the air flow, two air flow meters are available. They are installed in parallel in order to cover the flow over a wide range that would not be possible otherwise using a single flow meter. These are, namely, one DP flow meter for low range 0 to17 Nm 3 /h (0 to 10 scfm) and one vortex flow meter for high range 0 to 1115 m 3 /h (0 to 656 cfm). The vortex gas flow meter used in the present experiments has a measurement uncertainty of 1% of the indicated value.

The flow is controlled automatically from the computer control system, using a PID algorithm implemented in the LabVIEW program. The control system will regulate the opening of the valves CV1 and CV5 (Figure 4.7). The air flow is calculated based on the test section inlet pressure (2inP1 in Figure 4.7). The calculation is carried out using ideal gas equation. The measurement instruments used, shown in the Figure 4.7, are: The vortex flow meter, F1, temperature and pressure at the air supply measurement section (T1 and P1-air, respectively), as well as the pressure and temperature at the pipe line, 2inP7 and 2inT6, respectively.

Water is supplied from the separator tank by the water pump. In order to measure the flow rate, a Coriolis flow meter is used. The Coriolis flow meters provide measurement of density and volumetric flow rate; hence also mass flow rate can be

obtained. The Coriolis liquid flow meter has a measurement uncertainty of ±0.3% of the indicated value. The water flow is controlled automatically with the control system by using the water pump, Coriolis flow meter and control valve, CV3, see Fig. 2. An inverter is used to control the pump speed.

After being measured, the air and water are mixed. The mixing section consists of a concentric 2-in pipe of air joining a 4-in 90 °bend with liquid in a mixing bend configuration, as shown in Figure 4.8. Check valves are used to prevent liquid going into the air line and vice versa.

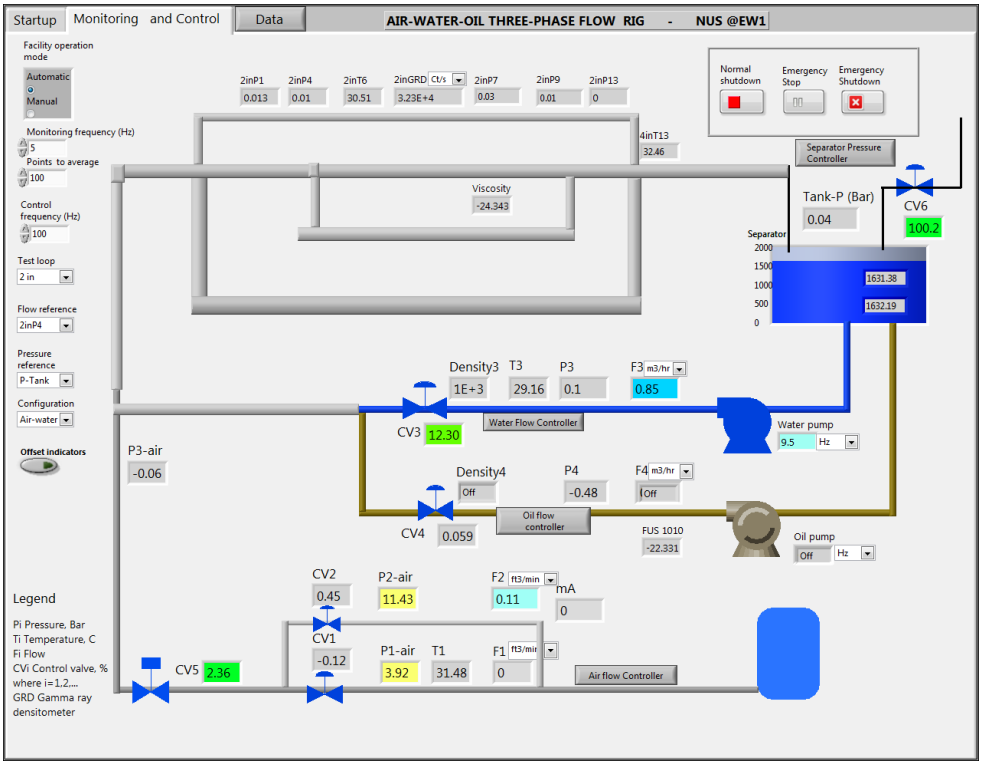

Figure 4.7: Experimental Setup Control panel

The test section consisted of a 40 m long loop in a rectangular shape as depicted in the Figure 4.8. Measurements were taken at P1, P7 and P13. Pressure and temperature sensors are placed at different locations, as shown in Figures 4.6-4.8, to monitor and take into account pressure and temperature effects. Pressure sensors have a measurement uncertainty of 0.05% of the scale (16 Bar). The flow loop data acquisition is carried out using LabVIEW (National Instruments). After travelling across the flow loop, the mixture goes into a three-phase separator that also serves as storage tank. After separation, the liquid is recycled, while air is released to the atmosphere through the control valve CV6 (Figure 4.7) and a silencer. The separator tank volume is 16 m^3 and it holds 5 m^3 of water and 5 m^3 of oil. Efficient phase separation in the three-phase flow separator is confirmed by the density readings from the Coriolis flow meters.

For the experiments presented in this dissertation, the flow loop was limited to air-water flow in a horizontal configuration.

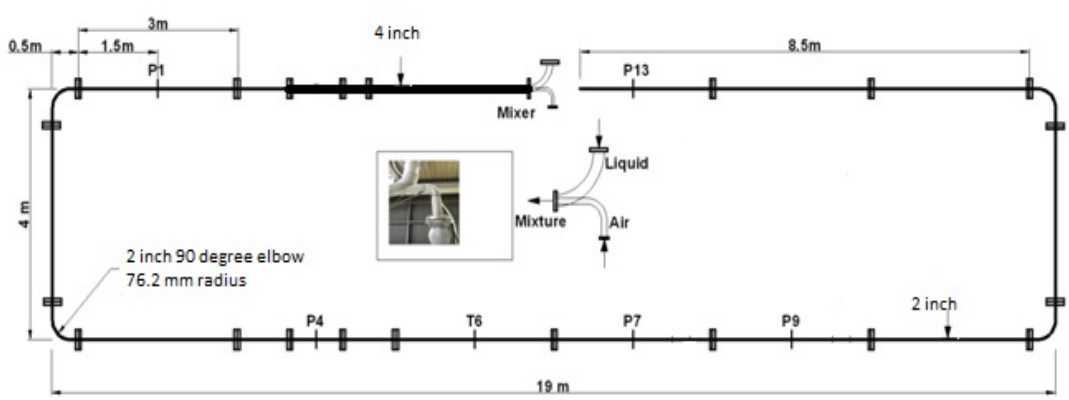

Figure 4.8: Top view of the physical configuration of the 2-inch test loop, mixing section and instrumentation.

4.3.2. Results and Discussion

4.3.2.1. Effect of the Number of Modes on the Low-D model Accuracy

In Chapters 2 and 3, the effect of the number of modes considered in the approximation of (2.12) on the pipeline dynamic response was outlined. The intend of this section is to validate the conclusions drawn previously by comparing the low-D model prediction to experimental results for different approximation orders n.

The gas and liquid superficial velocities (Figure 4.9(a)) and the test section outlet pressure P13 (Figure 4.9(b)) are used as model inputs.

Given in Figure 4.10 is the inlet pressure predicted by the low-D model using different truncation orders of the hyperbolic transfer functions given by (2.12) compared to the measured inlet pressure P1 in the multiphase flow loop

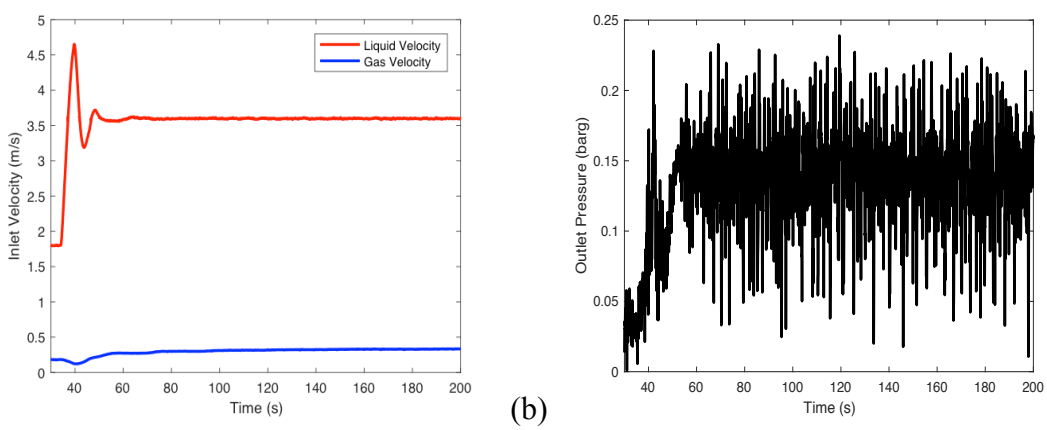

(a) (b)

Figure 4.9: Model Inputs (10% GVF): (a) Liquid and Gas Superficial Velocity, and (b) Outlet Pressure

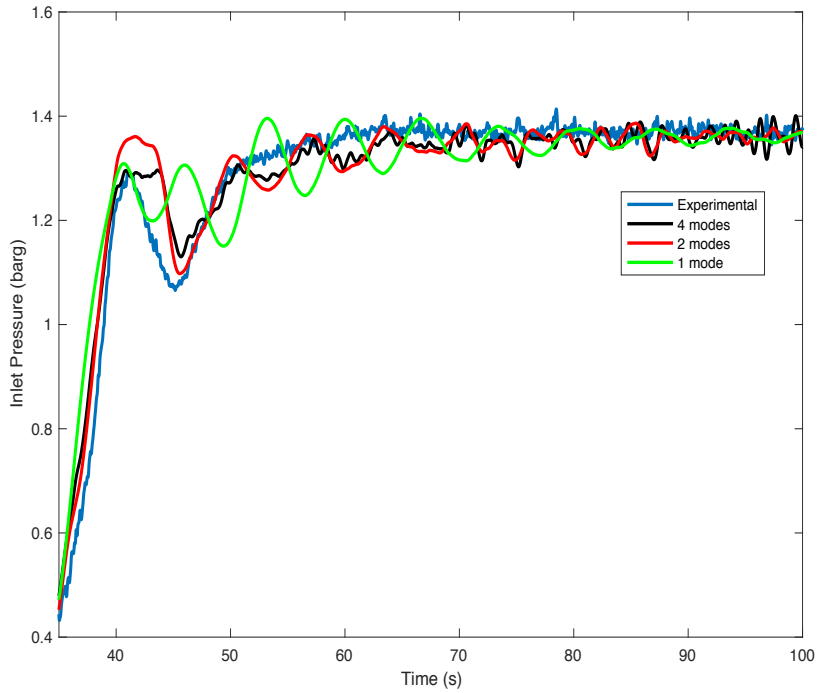

Figure 4.10: Experimental vs. Low-D Model Predictions as Function of the Truncation Order

It is shown in Figure 4.10 that using a higher number of modes results in a better estimation of the transient inlet pressure (more accurate estimation of the oscillation frequency and pressure overshoot). However, this results in a higher simulation time. Hence, a trade off should be performed to determine the optimal number of modes as suggested in Chapters 2 and 3.

Given in Figure 4.11 are the computation time and the Mean Absolute Percent Error (MAPE) as a function of the number of modes considered in the low-D model. As the number of modes is increased, the MAPE drops quickly at the beginning while the computation time undergoes a low increase. This tendency is inverted when considering the higher number of modes where the computation time increases dramatically without a noticeable improve in the model accuracy. Hence, it is crucial to select the suitable

number of modes depending on the desired model application and available computing power. For the rest of this Chapter 4-modes will be considered to approximate the transfer functions in (2.12).

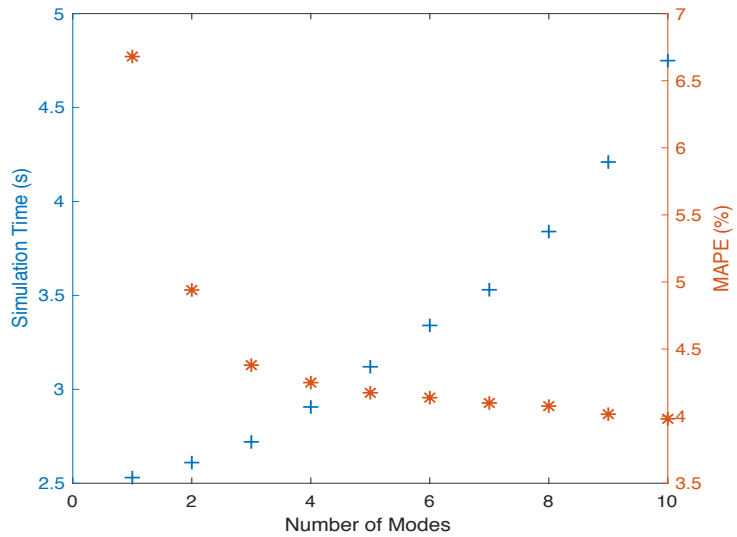

Figure 4.11: Simulation Time vs. MAPE

4.3.2.2. Effect of Entrained Air on the Pipeline's Dynamic Response

The transient single-phase flow in pipelines has been extensively studied in the literature [17, 19, 109]. However, in most of the studies, the effect of entrained air on the pipeline's dynamic response has not been accounted for. Air pockets can form inside the pipeline due to bubble entrainment through the action of pump suction (Figure 4.7) or can be released as the pressure of the liquid decreases along the pipeline. Under standard conditions water can contain up to 2% of entrained air per volume unit [110]. Depending on the application, the effect of entrained air can be either beneficial or detrimental. The presence of air in pipeline systems can result in numerous problems including loss of carrying capacity, disruption of the flow, reduced pump and turbine efficiency or create

cavitation problems under low-pressure conditions causing significant damage to the pipeline's structure.

On the other hand, the speed of waves propagation can be reduced substantially with the presence of air in the pipeline and the damping can be increased allowing a shorter length of the fortified zone required for a the High Integrity Pressure Protection System (Chapter 5).

In this section, the National University of Singapore multiphase flow loop, the low-D two-phase flow models of Chapters 2 and 3, and the OLGA multiphase flow simulator are used to investigate the effect of the entrained air on the pipeline's dynamic response.

The water pump of the flow loop is activated to step the liquid superficial velocity from 0.1 m/s to 2 m/s while keeping the air compressors inactive. Shown in Figure 4.12 are the liquid flow rate and the outlet pressure in the test section.

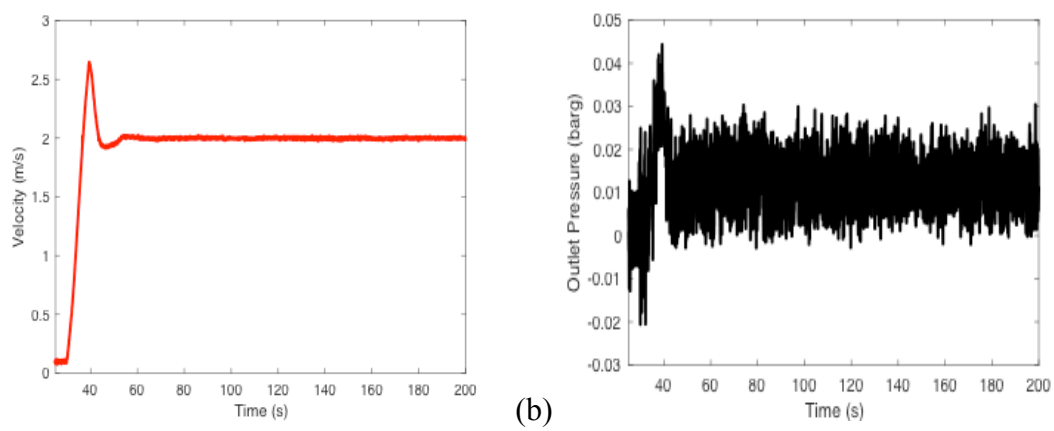

(a) (b)

Figure 4.12: Model Inputs (Liquid/Case1): (a) Liquid Superficial Velocity, and (b) Outlet Pressure

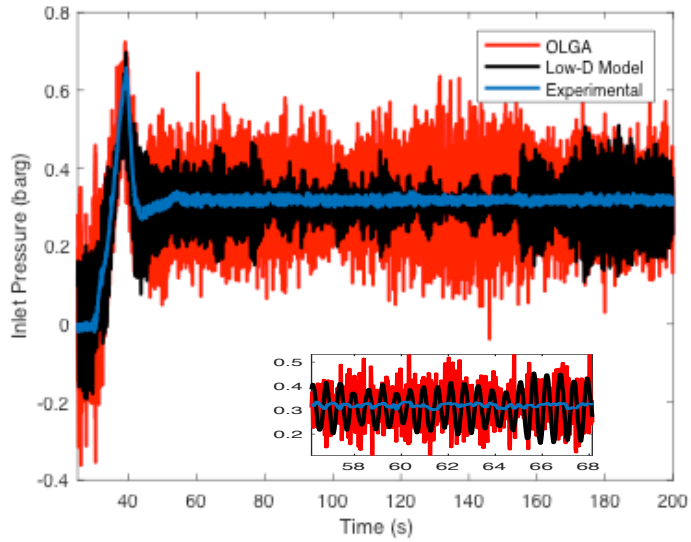

Figure 4.13: Experimental vs. Simulations (Liquid/Case1)

The measured inlet pressure and the one predicted by the low-D model and the OLGA simulation are given if Figure 4.13.Both models show a good agreement of the steady-state predictions of the inlet pressure with the experimental data. However, the low-D model and the OLGA simulations are characterized by higher frequencies of oscillation associated with higher overshoot. To confirm those findings two similar cases are run on the flow loop where the inlet liquid superficial is stepped from 0.1 m/s to respectively 3 m/s (Figure 4.14) and 4 m/s (Figure 4.15). The measured and simulated inlet pressures are shown in Figures 4.16 and 4.17.

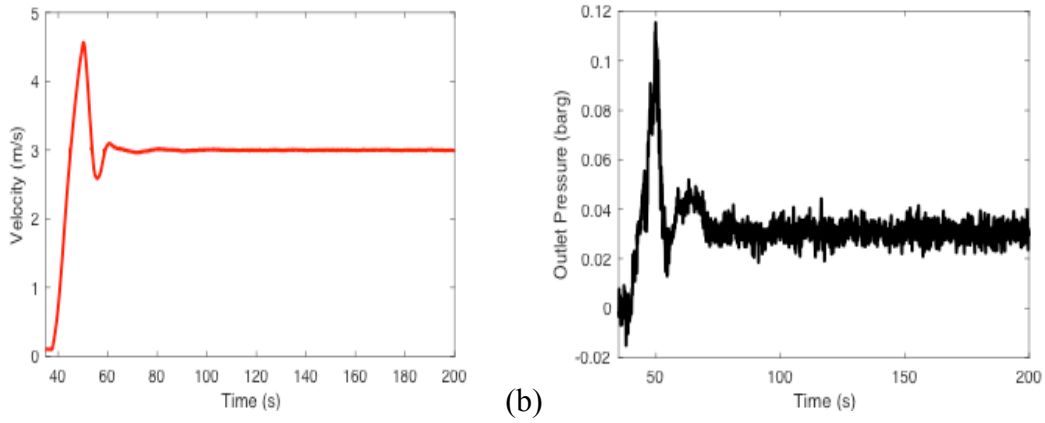

(a) (b)

Figure 4.14: Model Inputs (Liquid/Case2): (a) Liquid Superficial Velocity, and (b) Outlet Pressure

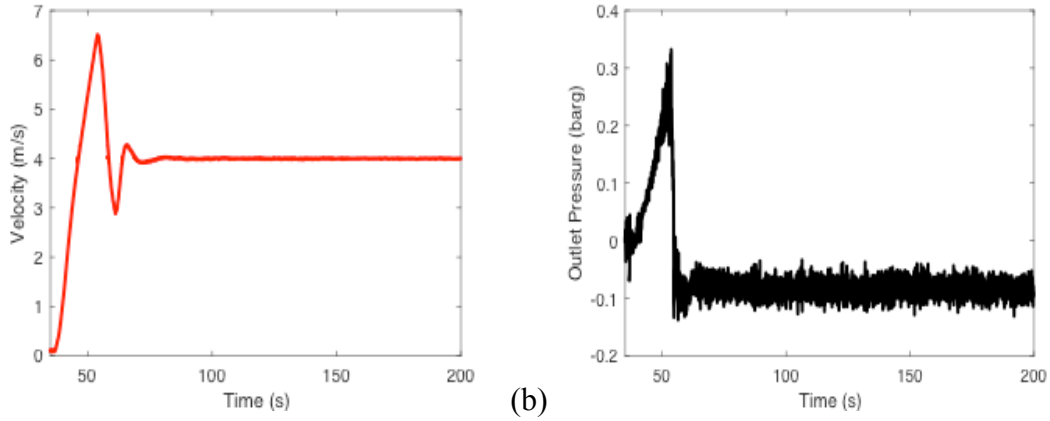

(a) (b)

Figure 4.15: Model Inputs (Liquid/Case3): (a) Liquid Superficial Velocity, and (b) Outlet Pressure

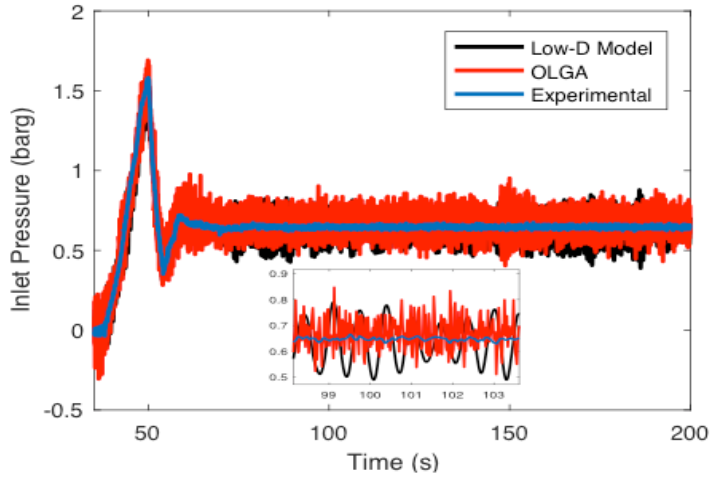

Figure 4.16: Experimental vs. Simulations (Liquid/Case2)

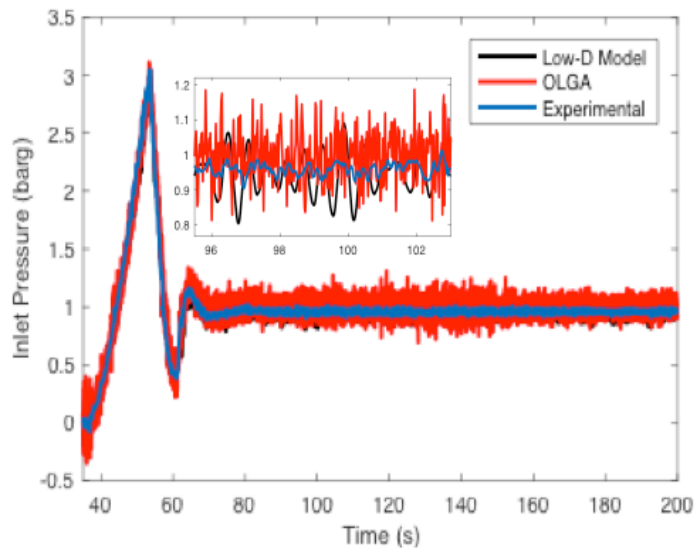

Figure 4.17: Experimental vs. Simulations (Liquid/Case3)

We notice that the amplitude of oscillation decrease from Case 1 to Cases 2 and 3. This can be explained by a higher turbulent flow resistance due to the increase in the liquid flow rate. We notice also, similarly to Case 1, that both the low-D model and the OLGA simulations give higher frequency oscillation and overshoot.

Upon further investigation of Cases 1-3, the air velocity sensors are recording low flow rates, suggesting the presence of entrapped air in the system. The presence of entrained air in the pipeline results in a significant increase in the fluid compressibility. This effect can be modeled by altering the fluid equivalent bulk modulus. Two models are presented in the literature to account for the effect of the entrained air on the fluid bulk modus. In [111] the author propose the following equation

$$\beta_{eq} = \beta_L \frac{1 + r_v}{1 + \left(\frac{P_0}{P}\right)^{\frac{1}{k}} r_v \frac{\beta_L}{kP}}; r_v \equiv \frac{V_{G_0}}{V_{L_0}}, \tag{4.1}$$

where β_L is the liquid bulk modulus without entrained air; V_{G_0} is the entrained air average superficial velocity in the liquid at atmospheric pressure; V_{L_0} is the average liquid velocity at atmospheric pressure; P_0 is the atmospheric pressure, P is the fluid average pressure; and is k is the isentropic exponent (normally, k=1.4).

In Chapter 2, the equivalent bulk modulus of a two-phase flow mixture was characterized as a function of the GVF level (2.41). The same equation can be adopted to account for the effect of entrained air (very low GVF) on the equivalent bulk modulus. The pipeline compliance also affects the fluid compressibility [111]

$$\beta' = \beta \frac{1}{1 + \frac{\beta}{\beta_P} w}, \tag{4.2}$$

where β_P is the bulk modulus of the pipeline and w is given by

$$w = \frac{2\left(\frac{d_o}{d_i}\right)^2 (1+\upsilon) + 3(1-2\upsilon)}{\left(\frac{d_o}{d_i}\right)^2 - 1}, \tag{4.3}$$

if $\frac{S}{d_o} > 0.1$ (thick walls) or $w = \frac{d_i}{S}$, if $\frac{S}{d_o} < 0.1$ (thin walls), where d_o outer pipe diameter; d_i inner pipe diameter; v Poisson's number (0.3 for steel) and S pipe wall thickness. Shown in Figure 4.18 is the water equivalent bulk modulus as a function of the GVF level (up to 2%) using Model1 (4.1) and Model2 (2.41).

We can notice a very good agreement between the two models in estimating the effect of entrained air on the water bulk modulus. Both model predict a sudden decrease in the bulk modulus as the first air bubbles are introduced which results in an important

increase of the fluid compressibility. The entrained air will also affect the fluid equivalent density as shown in (2.42). Given in Figure 4.19 is the equivalent density as function of the GVF level.

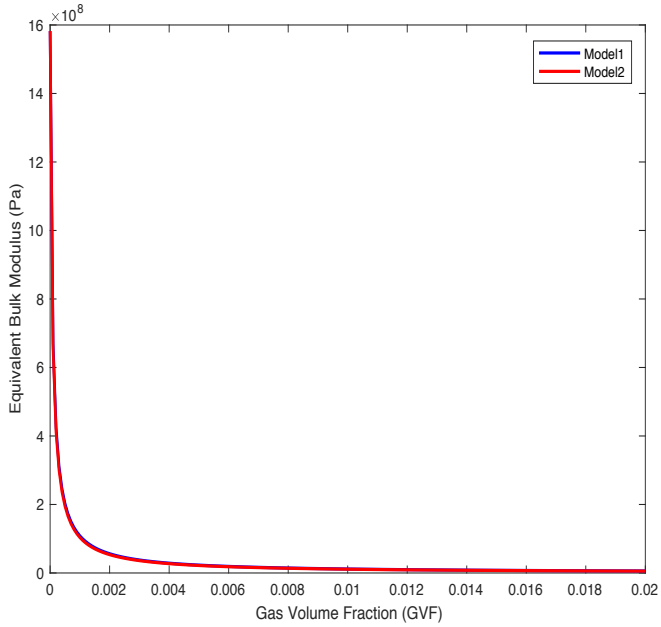

Figure 4.18: Equivalent Fluid Bulk Modulus

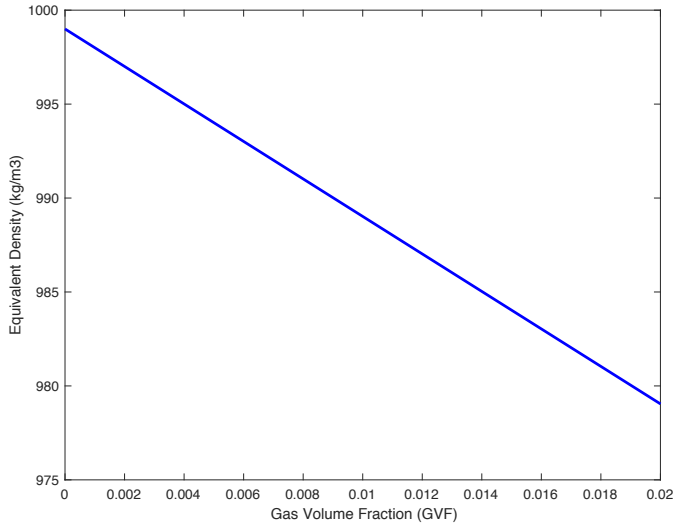

Figure 4.19: Equivalent Fluid Density

The experimental average air and water superficial velocities measured in the flow loop are used to calculate the GVF. The updated equivalent fluid parameters are used as model inputs for the low-D model for Cases 1-3 (Table 4.9).

Table 4.9: Equivalent Fluid Properties

Case No.	GVF	Equivalent Bulk Modulus (Pa)	Equivalent Density (kg/m3)
1-3	0 (No air)	1.58e9	999
1	0.015	7.12e6	983.55
2	0.016	6.85e6	982.94
3	0.014	7.57e6	984.48

In the OLGA simulator, an air feed corresponding to the average air velocity is introduced at the pipeline inlet to account for the entrained air. Shown in Figures 4.20-4.22 is a comparison between the experimental data and models estimations assuming the presence of entrained air.

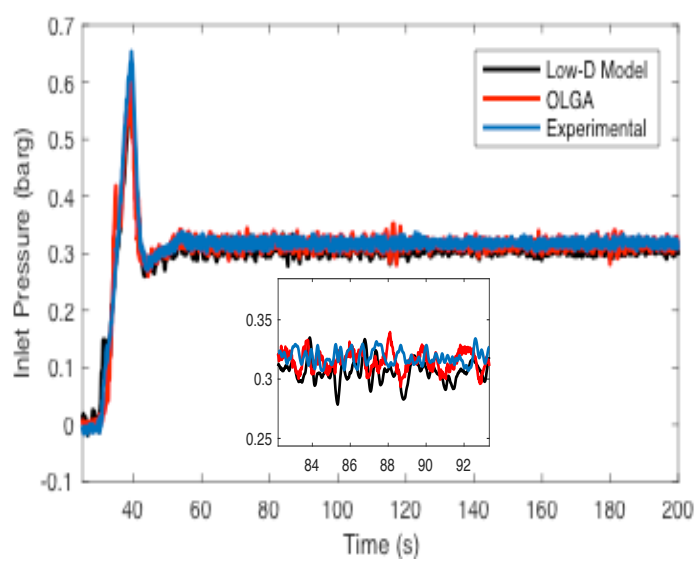

Figure 4.20: Experimental vs. Simulations (Liquid with Entrained Air/Case1)

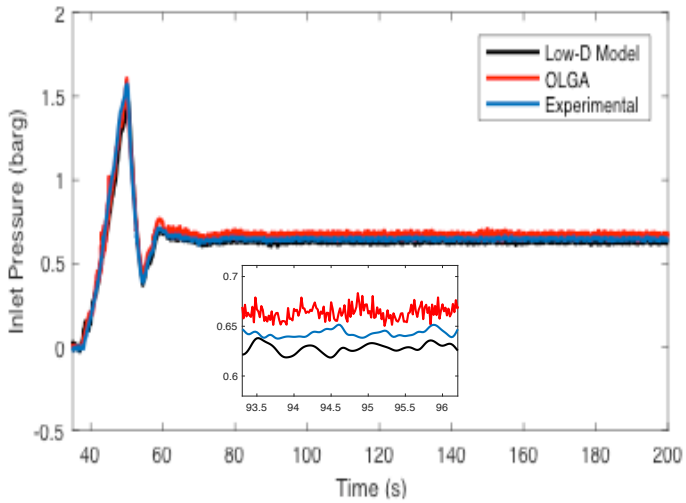

Figure 4. 21: Experimental vs. Simulations (Liquid with Entrained Air/Case2)

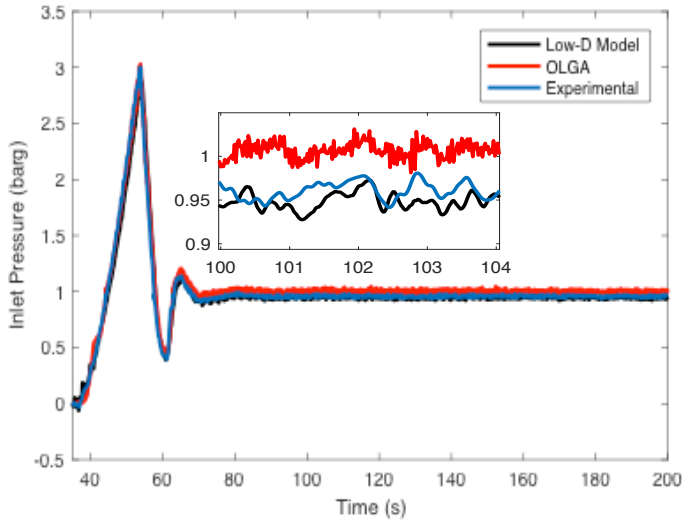

Figure 4.22: Experimental vs. Simulations (Liquid with Entrained Air/Case3)

It can be noticed that the introduction of entrained air in the system results in lower natural frequencies and higher damping ratios. This translates in time domain into a better matching of the oscillation frequency and the overshoot when compared to the experimental dataset. In the rest of this Chapter, the experimental dataset measured for higher GVF levels will be compared to the low-D model and OLGA predictions.

4.3.2.3. Effect of the GVF on the Pipeline's Dynamic Response

In this section the water pump and the air compressors (Figure 4.7) are used to control the water and air superficial velocity and therefore achieve GVF levels of 10, 20, 30, 40 and 50%. The measured liquid and air inlet superficial velocities and the outlet pressure, used as model inputs for the low-D model and OLGA, are shown respectively in Figures 4.9 and 4.23-4.26.

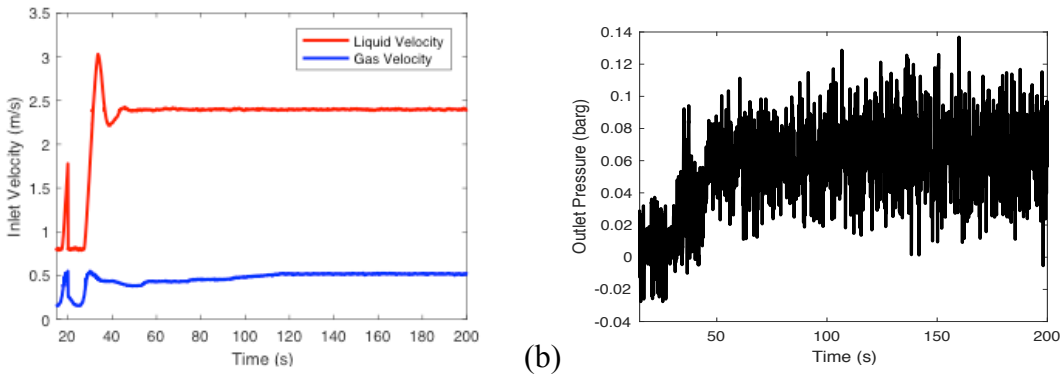

(a) (b)

Figure 4.23: Model Inputs (20% GVF): (a) Liquid and Gas Superficial Velocity, and (b) Outlet Pressure

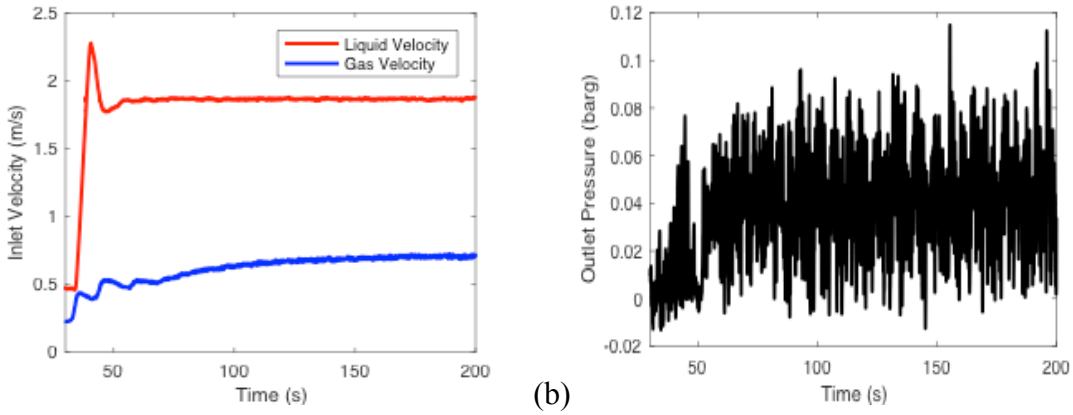

(a) (b)

Figure 4.24: Model Inputs (30% GVF): (a) Liquid and Gas Superficial Velocity, and (b) Outlet Pressure

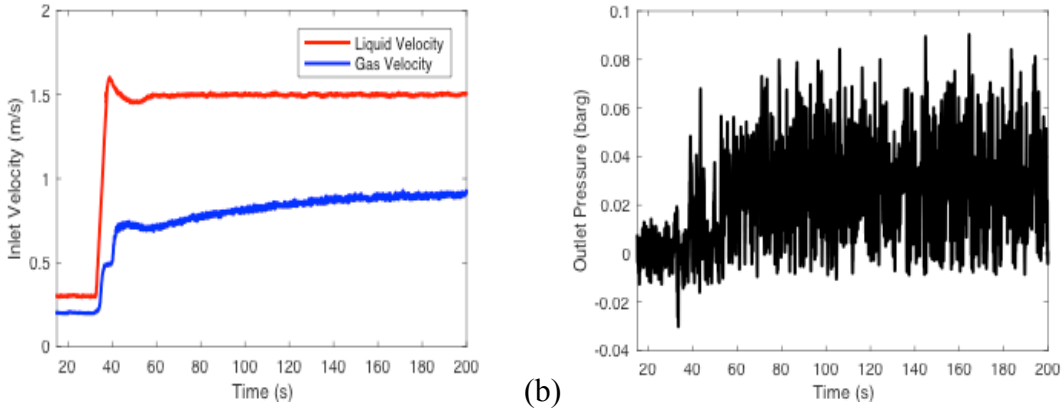

(a) (b)

Figure 4. 25: Model Inputs (40% GVF): (a) Liquid and Gas Superficial Velocity, and (b) Outlet Pressure

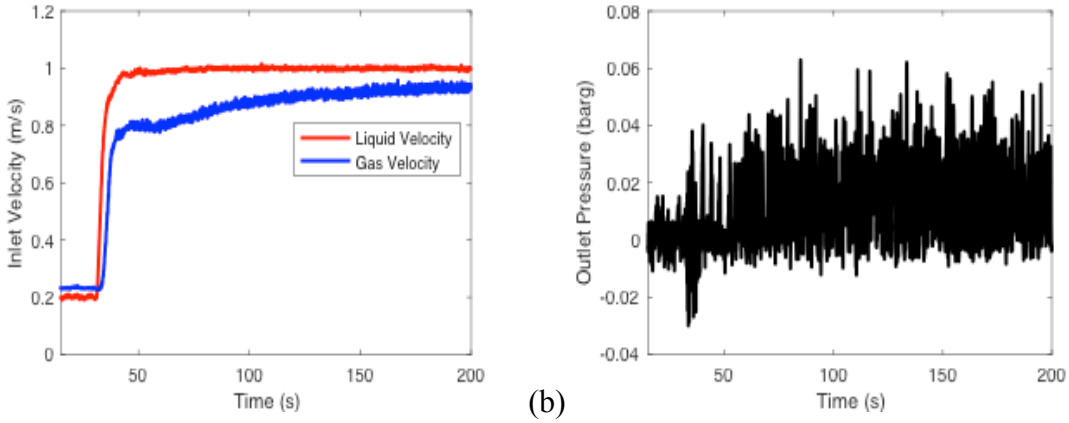

(a) (b)

Figure 4.26: Model Inputs (50% GVF): (a) Liquid and Gas Superficial Velocity, and (b) Outlet Pressure

The measured and simulated inlet pressures are given in Figure 4.27 for the case of a 10% GVF level. By comparing the 10% GVF case (Figure 4.27) to the low GVF dataset (Figure 4.20-4.22), we can notice that the inlet transient pressure response is characterized by a lower overshoot caused by a higher damping caused by a dramatic decrease in the fluid speed of sound. This effect was better captured by the low-D model when compared to the OLGA simulation. We notice also that the OLGA and Low-D models present a good agreement with the experimental dataset in the steady-state pressure and the period of oscillation demonstrating a similar estimation of the pipeline

natural frequency. However they present a discrepancy in the overshoot values and the settling time, which can be explained by a difference in the calculated damping ratio. Those results support the conclusions drawn in section 4.2. It is clear, in Figure 4.27, that the 4-modes realization of the low-D model has a better estimation of the pipeline transient response.

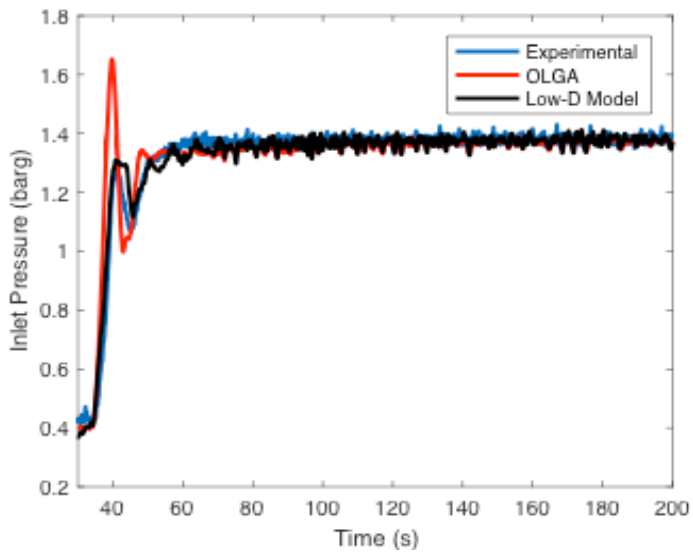

Figure 4.27: Experimental vs. Simulations (10% GVF)

To evaluate and compare the overall models accuracy, the MAPE with respect to the experimental dataset is compared for the different considered GVF levels (Table 4.10). Note that only the transient part of the data is considered in the calculation of the MAPE. The low-D model is characterized by a lower MAPE for the 10% GVF case. This confirms its superior performance. The measured and predicted inlet pressures for 20-50% GVF are presented in Figures 4.28-4.31.

Table 4.10: Low-D Model and OLGA MAPE

GVF	10%	20%	30%	40%	50%
MAPE (Low-D Model)	4.25%	7.26%	9.91%	12.84%	16.94%
MAPE (OLGA)	8.1007%	14.52%	18.65%	25.78%	36.04%

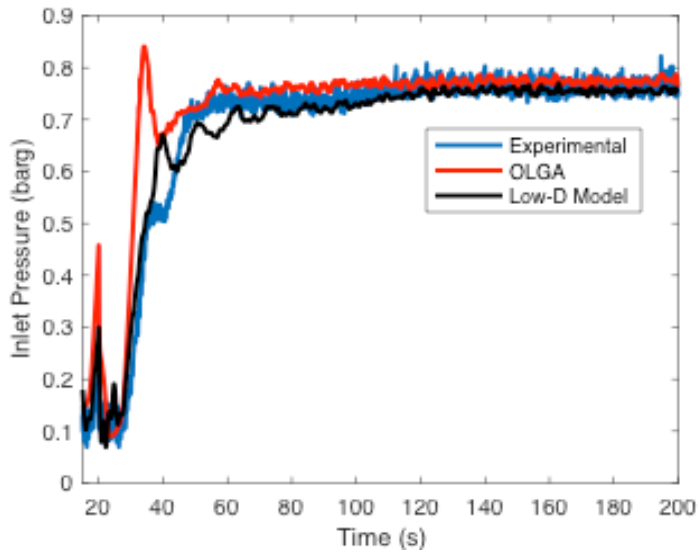

Figure 4.28: Experimental vs. Simulations (20% GVF)

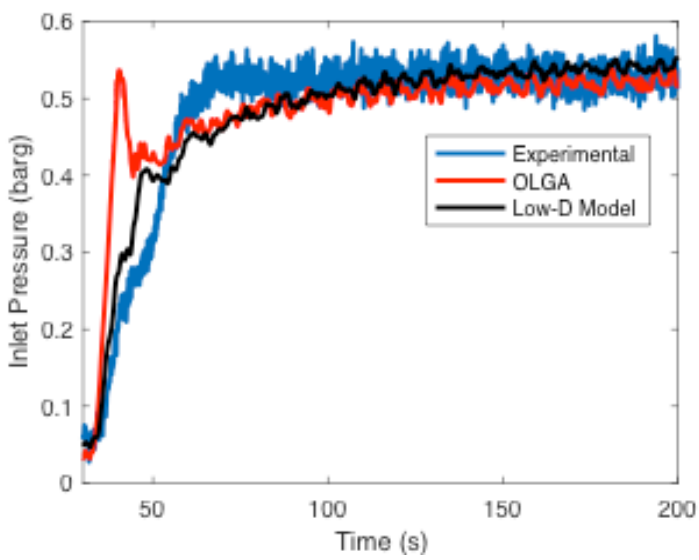

Figure 4.29: Experimental vs. Simulations (30% GVF)

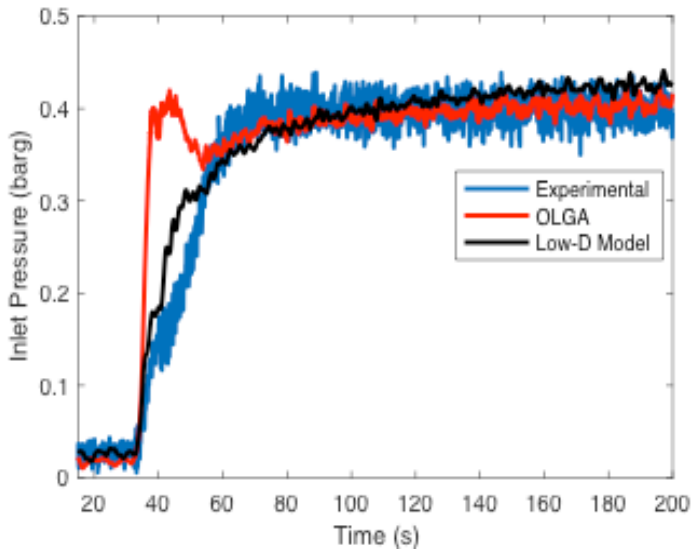

Figure 4.30: Experimental vs. Simulations (40% GVF)

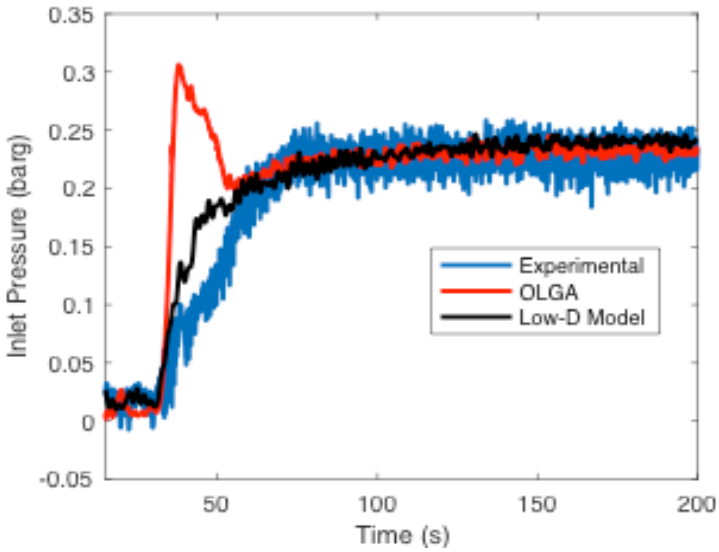

Figure 4.31: Experimental vs. Simulations (50% GVF)

As the GVF level is increased in the pipeline by a higher gas flow rate imposed by the air compressors, the steady-state pressure drop across the pipeline decreases driven by a lower equivalent dynamic viscosity. This phenomenon was equally captured by the developed low-D and the OLGA models. Increasing the GVF results also in an

overdamped system for the presented dataset in Figures 4.28-4.31. We notice, again, that the low-D model gives a better estimation of the system's damping ratio when compared to the OLGA simulation especially at higher gas contents (Figure 4.31). We notice in Figure 4.28 the presence of terrain slugging in the test section indicated by the sudden increase of the water flow rate and inlet pressure. This phenomenon is created by the accumulation of water at the bend upstream of the test section before being suddenly pushed by the air pressure. While the terrain slugging is present in the simulated pressure by both models, the hydrodynamic behavior of slug flow is not captured as the low-D and OLGA models only model the average pressure seen by the pipeline as previously outlined in section 4.2. From Table 4.10, the following conclusions can be drawn:

- Both models give a good estimation of the two-phase flow pressure (MAPE<40%);
- The MAPE of both models increases for higher GVF levels; and
- The low-D model has a superior performance when compared to the OLGA model for all the considered cases.

4.4. Conclusion

In this chapter, the ability of the developed low-D model to reproduce the dynamics of multiphase flow in pipes has been evaluated first upon comparison to OLGA simulations for different flow regimes and GVF level. The two models presented a good agreement of the steady-state response and the period of oscillation demonstrating a similar estimation of the pipeline natural frequency. However they present a discrepancy in the overshoot values and the settling time, which can be explained by a difference in the calculated damping ratio.

To further evaluate the models performance, experimental data were collected from the National University of Singapore multiphase flow loop. This permitted to determine the effect of the number of modes on the low-D model accuracy and the simulation time. The analysis of the single-phase flow experimental dataset established the existence of entrained or entrapped air in the system due to the action of the water pump. It has been proven that the presence of entrained air in the pipeline results in a significantly lower speed of sound of the fluid leading to a considerable increase in the pipeline damping and a decrease in the natural frequency. The low-D model pressure predictions and the OLGA simulations were compared to the measured pressure for different GVF levels. It is concluded that the low-D modeling approach is characterized with a better overall performance, especially in the overshoot estimation.

Chapter 5

Design, Simulation and Optimization of Subsea Architectures with a High Integrity Pressure Protection System (HIPPS)

5.1. Introduction

The production of an ultra-deepwater reserve involves the flow of oil, gas, water and aggregate within a reservoir to a low-pressure region created by the well(s). Commonly multiple wells are drawing hydrocarbons from the same reservoir to increase production rates, improve the oil and gas recovery and allow multiple access points to the reservoir. Yet, despite sharing a common reservoir, each well is distinct in terms of its production composition, flow rates, temperature and pressure. Production variations among the wells make the subsea production systems challenging and complicated. As mentioned in Chapter 1, multiphase flow phenomena are a ubiquitous and key factor in any oil and gas drilling or production operation.

Focusing on subsea production applications, this chapter aims at demonstrating how the developed multiphysics low-D models can be used in a systems approach for the design, simulation and optimization of subsea architectures. In addition, the installation of a High Integrity Pressure Protection Systems (HIPPS) is discussed as a possible mean to reduce the subsea project capital expenditures (CAPEX).

5.2. Subsea Field Architectures

At the end of the drilling operations, a subsea production structure is installed to control the wellhead and ensure the production and transportation of the hydrocarbons to the host facility. Subsea production equipment can be arranged in multiple layouts or architectures as dictated by the operator strategy and each field specificities and requirements. The most common configurations are [64]:

- Single-Well Tie Back: In this architecture (Figure 5.1 (a)), each subsea well is connected back to the host platform or floating production facility using a dedicated single or dual production pipeline. It is typically used for small fields containing a limited number of wells or in the case of widely separated wells. This architecture has the advantage of being easy to install and maintain but is characterized with a high cost due to the required length of pipelines and umbilical.
- Daisy Chain Tieback: In this architecture (Figure 5.1 (b)), a flowline loops from one production well to the other forming a daisy chain before returning to the host facility. This layout enables considerable cost savings but can bring a multitude of flow assurance issues. In addition, additional isolation equipment need usually to be installed to separate one well from the others in case of faults or instabilities.
- Cluster Well Manifold: In this architecture (Figure 5.1 (c)), the production from the different wells is grouped into a subsea manifold using jumpers. The overall production is then transported into the host facility via single or dual flowline(s). The dual flowlines provide redundancy, and permit pigging but is associated with an extra cost. This subsea layout usually serves a limited number of wells (typically four to six).

- Multi-well Template: This configuration (Figure 5.1 (d)) generally includes many of the features of a cluster well manifold described previously. The main difference is that the wells and the manifold are located on the same structure. In that case, the umbilical and jumpers relating the trees to the manifold can be prefabricated and tested prior to the subsea installation. However, this requires the wells locations to be close to each other and known with a higher precision.

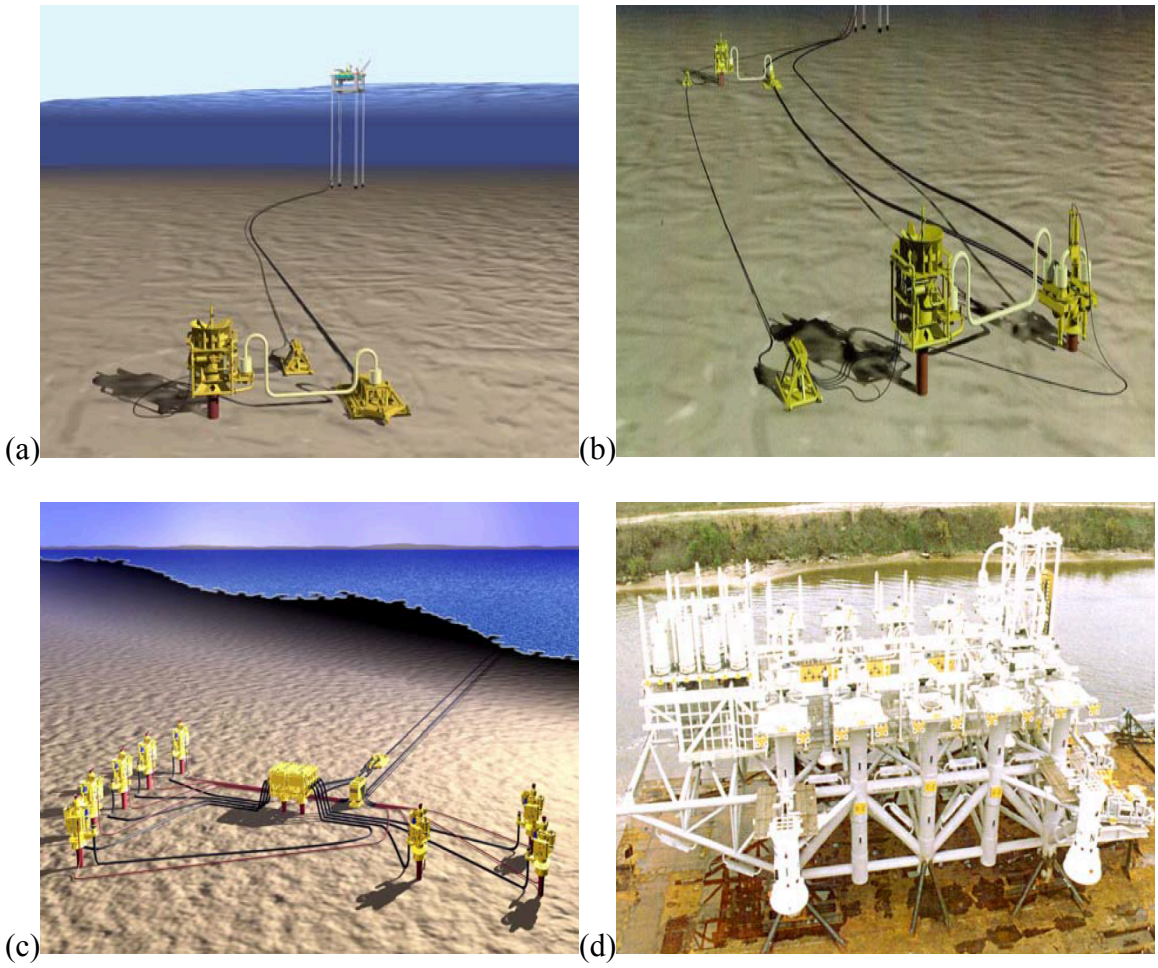

Figure 5.1: Subsea Field Architectures: (a) Single-Well, (b) Daisy Chain, (c) Cluster, and (d) Template

5.3. Overview on Subsea HIPPS

During the oil and gas production, the internal pressures seen by the pipelines are significantly less than the total reservoir pressure. However, traditional subsea pipelines are designed to be fully rated systems. That is, the pipelines are able to withstand the highest potential reservoir pressures. The need for these extreme designs is due to several reasons. Consider the case when the riser emergency shutdown (ESD) valve is activated before the Christmas tree valve located at the well can be closed. In this case, the entire subsea piping system will experience high transient pressures (surge pressures) since the flow has suddenly stopped. Another case is when a hydrate or blockage forms within the pipelines network. Here the pipeline(s) upstream of the blockage will undergo the surge pressures. Therefore, pipelines without proper protection from such high-pressure spikes can be damaged.

The desire to meet both an allowable capital expenditures (CAPEX) and ecosystem safe subsea production system has led to a new approach for high-pressure-high-temperature (HPHT) oil and gas production.

The solution comes from the installation of High Integrity Pressure Protection Systems known as HIPPS. HIPPS is a safety-instrumented system for protection from over pressure in the pipelines. The primary function of the HIPPS is to protect the downstream production system from overpressure by closing off the source. This is accomplished by the timely closure of one or more dedicated shutoff valves. The benefit realized by HIPPS is that the downstream piping requirement can be relaxed, thus reducing the cost and making the project economically feasible.

HIPPS is a self-contain instrumented safety device that isolates high-pressure flows upstream of its location (Figure 5.2). This modular safety device contains a gate valve, fluid power system, and onboard intelligence. A spring is located in the hydraulic cylinder so that when all power is lost, the valve is closed. During normal operation, the cylinder pressure above the piston is high, pushing the piston rod assembly downward thereby opening the valve (Figure 5.2, left diagram). Constant high-pressure hydraulic fluid must be maintained to the HIPPS to keep the valve open. To close the valve, the high-pressure fluid above the cylinder piston is vented and the valve closes due to the spring. The valve may close faster by supply a high pressure below the cylinder piston.

A redundant onboard intelligent system (Figure 5.3) determines whether the valve is open or closed. In some cases, multiple gate valves are employed to provide mechanical redundancy to improve the integrity of the HIPPS. Upstream of the valve are triple pressure and temperature (PT) sensors and a dual hydraulic rod piston rod displacement transducer to indicate cylinder actuation. Paralleling the aerospace industry, the multiple sensors provide high integrity to the HIPPS onboard intelligence. A two-out-of-three (2oo3) voting strategy is used to decide if closing the HIPPS system is necessary. With the HIPPS safety role of isolating high-pressure flows upstream to protect downstream pipelines, it is critical that complete fault-tolerant operation be guaranteed.

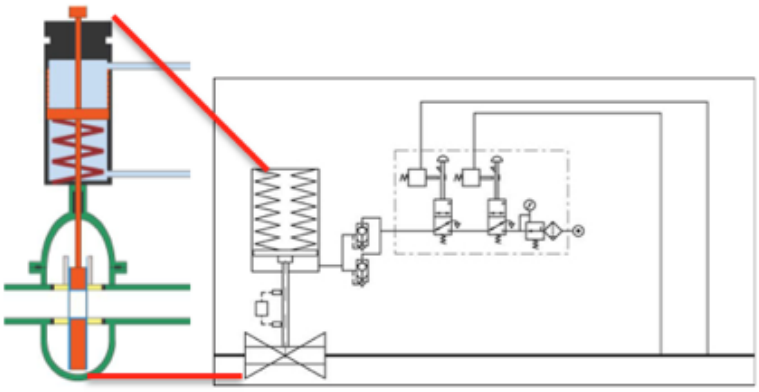

Figure 5.2: HIPPS Cross Sectional View and Hydraulics

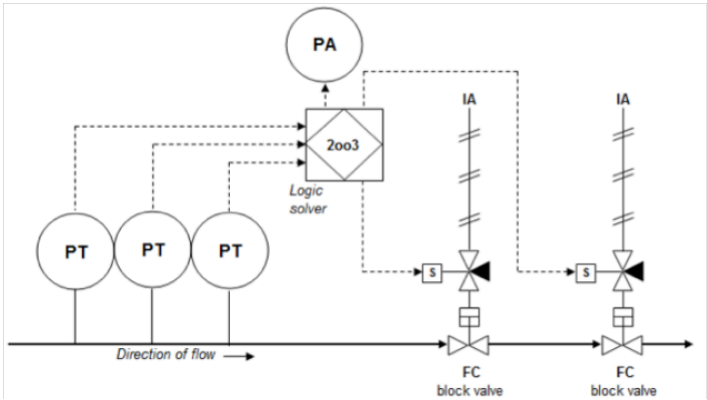

Figure 5.3: HIPPS Onboard Intelligent System

The sate of the art in the design of a subsea HIPPS has been described in [112, 113]. However, the impact of the HIPPS installation on the subsea architecture dynamics and project CAPEX has yet to be identified.

5.4. Subsea HIPPS Model-Based Design Procedure

The complexity of multiple-well subsea systems requires the use of a model-based HIPPS design procedure to produce a viable yet cost-effective solution. The recommended model-based procedure is summarized by the flow chart in Figure 5.4.

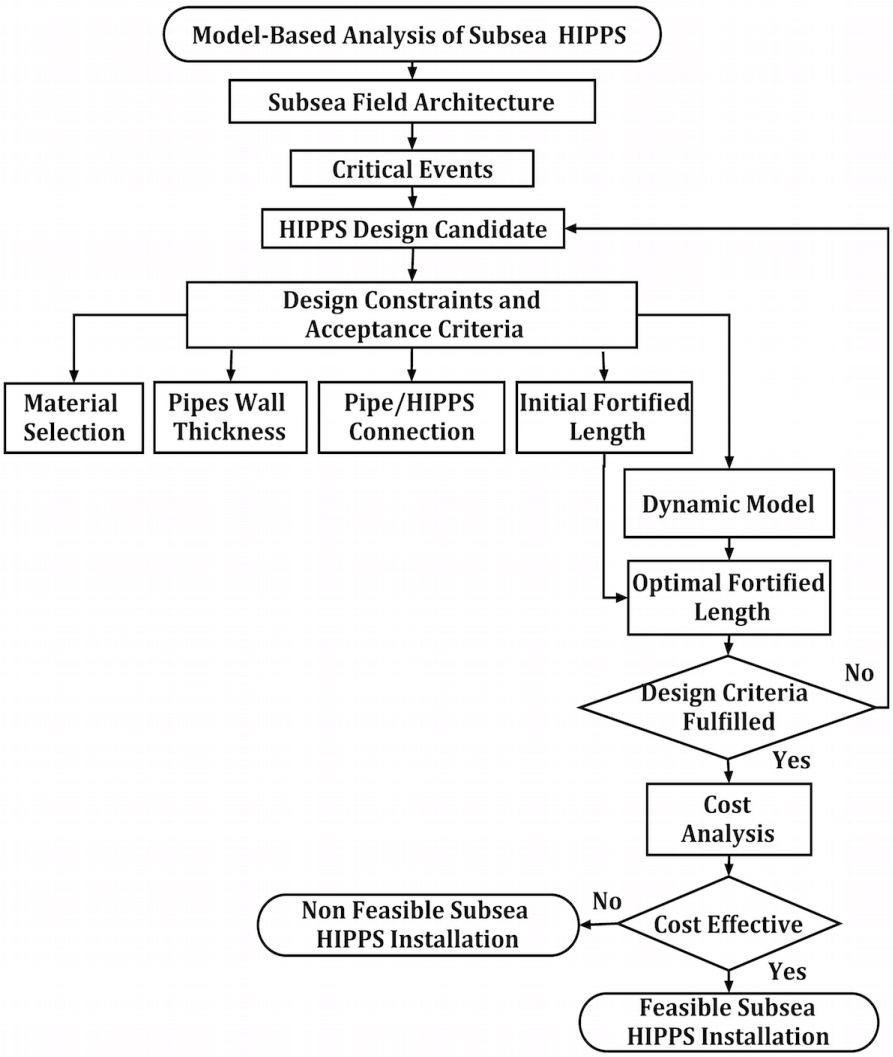

Figure 5.4: Flow Chart for a Model-Based Analysis of Subsea HIPPS

Following is a description of the different steps involved in the subsea HIPPS proposed design procedure.

Step1: Subsea Field Architecture

This step involves collecting the necessary information needed for the design and evaluation of the HIPPS, such as reservoir characteristic (number of wells, production composition, flow rates, temperature and pressure levels, etc.); field layout (individual tie

back, cluster manifold system, daisy chain, etc.), pipelines diameter, and distance to the hosting facility.

Step 2: Critical Events

The closure of the HIPPS valve can be caused by one of the following events:

- An increase in the pipelines inlet pressure due to a higher reservoir pressure or a failure of a choke valve resulting in a sudden increase in the wells production rate;
- A blockage du to hydrate or wax formation in the low-rated pipelines; and
- Activation of the riser emergency shutdown (ESD) valve before the closure of the Christmas tree valve located at the well.

All the discussed critical events will result in a sudden overpressure in the thin walled pipelines designed for the low-pressure working conditions.

Step 3: Design Constraints and Acceptance Criteria

Four international standards are currently used in the design of subsea HIPPS: IEC 61508 [114], IEC 61511 [115], API 14C [116], and API 17O [117]. The first three standards do not have a specific description of a HIPPS system. Instead, they give the requirements for the design of a safety-instrumented system, such as a Pressure Safety Valve (PSV) by introducing the concept of Safety Integrity Level (SIL) that can be extended to the HIPPS. Elaborated based on the standards described previously, the API 17O, published in 2009, represents the only industry guideline specific for the design of HIPPS.

Step 4: Equipment Sizing

Detailed in this section is the sizing of the subsea equipment according to the industry standards. Depending on the pressure rating, the material used for the different equipment can be determined according to the API 6A / ISO 10423 specification [118]. According to the ANSI/ASME Standard B31.1 [119] the pipeline wall thickness is determined using the following equation

$$t = t_e + t_{th} + \left[\frac{Pd_0}{2(SE + PY)}\right]\left[\frac{100}{100 - T_{ol}}\right], \tag{5.1}$$

where t is minimum design wall thickness (in); t_e is the corrosion allowance (in); t_{th} is the thread or groove depth (in); P is the allowable internal pressure in pipe (psi); d_0 is the outside diameter of pipe (in); S is the allowable stress for pipe (psi); E is the longitudinal weld-joint factor; Y is the derating factor and T_{ol} is the manufacturers allowable percent tolerance.

The design of the pipeline/HIPPS flanged connection is subject to the API 6A / ISO 10423 [118] Specification for Wellhead and Christmas Tree Equipment.

Step5: Multiphase Flow Dynamic Model

In this step, the low-D models proposed in Chapters 2 and 3 and validated in Chapter 4 are used to build a multiphase flow dynamic model for the subsea architecture. In this step, the flowlines (jumpers and pipelines) are integrated with other equipment such as check valves, directional valves, subsea tree, etc. The user can then define the model physical components parameters (geometry, material) as well as the fluid properties (density, absolute viscosity, Bulk modulus). Furthermore, this system approach

to modeling subsea architecture allows an easier design of the control system, critical to the HIPPS operations.

Step 6: Fortified Zones Design

HIPPS closing performance is a key factor during the design process. The HIPPS control system reaction time combined with the valve closure time must be lowered to protect the low-rated equipment downstream of its location from over pressure. However, a region downstream of HIPPS and upstream of the low pressure-rated pipelines must be designed to withstand the well shut-in pressure. This fortified zone is made of a thick wall pipeline that can withstand high-pressure flows that will progress downstream of the HIPPS during its closing time. The minimum required length of the fortified zone is determined based on dynamic simulations, using the models build in Step 5, for different HIPPS closing time and GVF levels. Furthermore, the riser and a short section of the pipeline upstream of the riser base need to be fortified to protect the platform from overpressure in case of a failure of the HIPPS valve.

Step 7: Cost Analysis

The use of subsea HIPPS with low-rated equipment downstream of its location was introduced by the oil and gas industry in high-pressure-high-temperature (HPHT) subsea wells as an alternative to the conventional approach involving the use of full-rated equipment. This new approach was mainly motivated by the need to reduce the high CAPEX by:

- Reducing the pipelines procurement cost by replacing the thick walled pipelines made of resistant materials by thin walled pipelines made of more conventional materials;

- Reducing the installation costs thanks to lower transportation cost and welding times, a higher installation speed and the use of less sophisticated pipe laying vessels.

Hence, any subsea HIPPS installation feasibility analysis should imperatively be concluded by balancing the CAPEX savings against the risks associated with the use of HIPPS.

5.5. Case Study: Design, Simulation and Optimization of a Multiple-Well Subsea Architecture

To illustrate the flow chart described in section 5.4, the installation of a subsea HIPPS in a multiple-well field is discussed step by step.

Step 1: Subsea Field Architecture

In this case study, a four-well subsea architecture is considered (Figure 5.5). The oil and gas production from the different wells is grouped through a subsea manifold, which feeds the riser through a 20 miles single production pipeline. Check valves are mounted at the outlet of each jumper allowing the coordination of the arrival pressures at the subsea manifold and therefore preventing backflow into the wells. A High Integrity Pressure Protection System (HIPPS) is mounted on top of the manifold to protect the downstream low-rated equipment from overpressure.

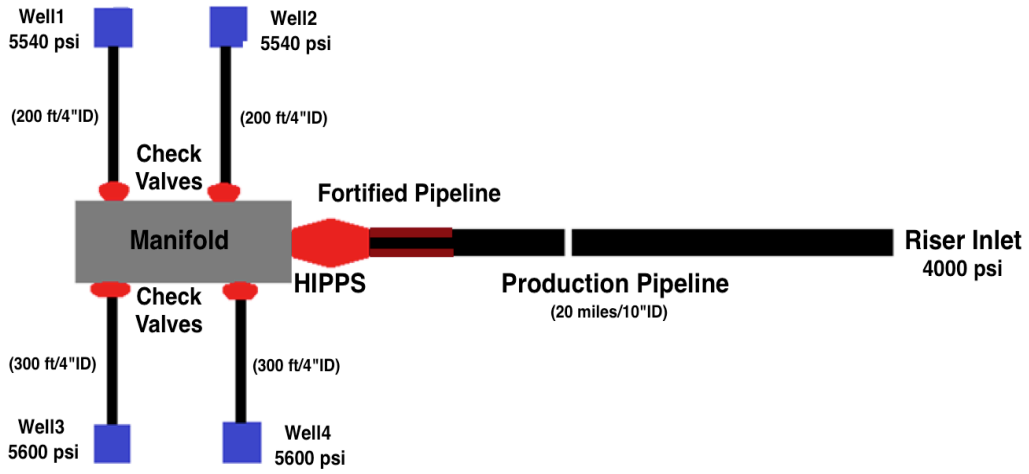

Figure 5.5: Simplified Schematic of the Case Study Subsea Architecture

Given in Table 5.1 are properties of the gas and liquid phases used in this study.

Table 5.1: Liquid and Gas Properties

	Liquid	**Gas**
Density (kg/m^3)	870	238
Kinematic Viscosity (Pa.s)	0.0153	1.12e-5
Bulk Modulus (Pa)	0.8e9	2.5e7

Step2: Critical Event

To simulate a sudden increase in the reservoir pressure due to an instability or a failure of a choke valve in the wellhead, the pressure in the wells 3 and 4 will be stepped to 14,000 psi. The effect of this event on the subsea architecture will be studied for different GVF levels and HIPPS valve closing times.

Step 3: HIPPS Design Candidate

In this study the HIPPS will be composed of one acting electro-hydraulic valve and a control module. The control module will close the HIPPS valve within the

prescribed closing time if the pressure downstream of its location exceeds the design pressure (6,000 psi). The characteristics of the HIPPS valve are given in Table 5.2.

Table 5.2: Characteristics of the HIPPS Valve

Valve Maximum Area (m^2)	3.5e-3
Valve Leakage Area (m^2)	5e-06
Valve Discharge Coefficient	0.7
Valve Maximum Opening (m)	0.1

Step 4: Design Constraints and Acceptance Criteria

The wells, Christmas trees, jumpers, manifold, HIPPS and fortified pipeline will be rated to the well shut-in pressure (15,000 psi) and subject to a SIL 3 design requirement (Probability of failure less than 10^{-3}). The low-rated section of the production pipeline will be designed to withstand a working pressure of 6,000 psi, enabling a reduction in the material grade and wall thickness.

Step 5: Equipment Sizing

Using the corresponding Table of the API 6A / ISO 10423 specification and the design constraints described previously, the 75k material is recommended for the full rated equipment upstream of the HIPPS and the fortified section of the production pipeline. The 65k material is used for the low pressure-rated section of the production pipeline.

The jumpers and pipelines wall thicknesses (Table 5.3) are calculated based on (5.1).

Table 5.3: Characteristics of the HIPPS Valve

	Wall thickness (in)
Jumpers	1.417
Fortified Pipeline	1.268
Low Pressure-Rated Pipeline	0.718

It is noticed that the installation of the HIPPS results in a considerable reduction of thickness in the production pipeline.

Step 6: Dynamic Simulations

First the Petalas and Aziz mechanistic two-phase steady-state model is used to determine the flow pattern, liquid holdup and pressure gradient at each component of the subsea architecture. The equivalent fluid parameters are then calculated for each GVF level. The described subsea architecture is implemented in a Simulink environment to simulate the dynamic pressure and flow responses (Figure 5.6).

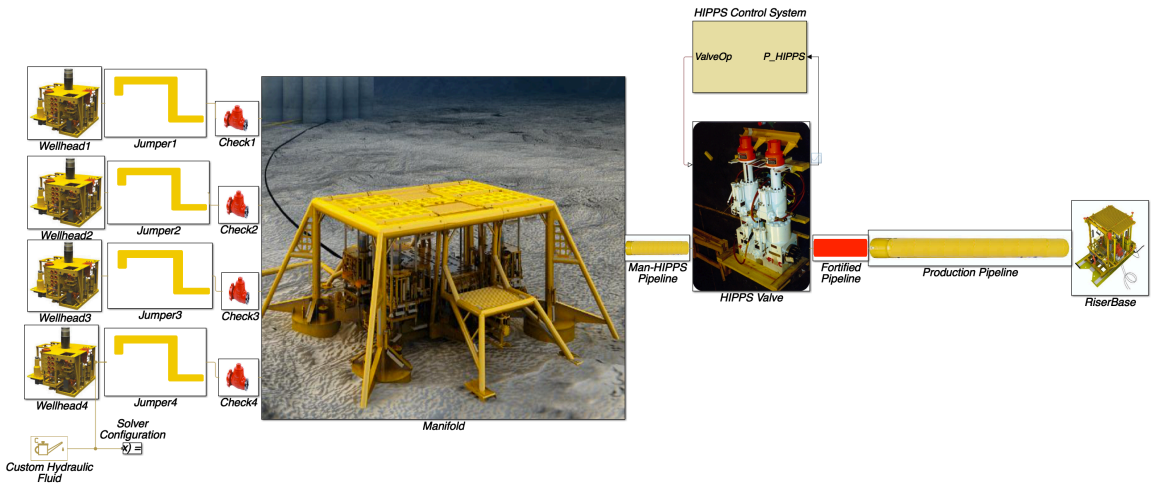

Figure 5.6: Four-Wells Cluster Subsea Architecture Dynamic Model

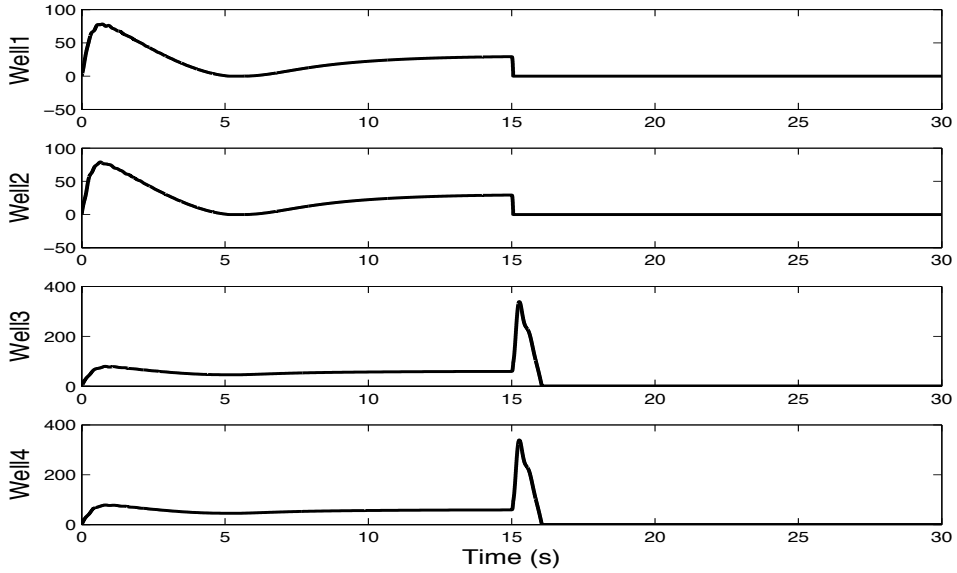

Figure 5.7: Wells Production Flow Rates

The pressure of wells 3 and 4 are stepped from 5600 to 14,000 psi at t=15s. Presented in Figure 5.7 are the production flow rates of the different wells. It is noticed that wells 1 and 2 are immediately shut down after the pressure step due to the closure of the check valves to prevent backflow. The closure of the HIPPS valve, located upstream of the manifold stops the production of wells 3 and 4 resulting in a complete shut down of the field.

Given respectively in Figure 5.8 and 5.9 is the transient pressure and flow rate at the inlet and outlet of the HIPPS valve for the case of a 0% GVF and different valve closing times. As mentioned in section III, choosing a proper valve closing time is a key factor in the design of a subsea HIPPS. In fact, the HIPPS valve and the control module should be designed to act as quickly as possible to protect the downstream equipment from overpressure. However, an abrupt closure of the HIPPS valve can lead to a considerable pressure surge at its inlet due to the water hammer effect, which may cause the pressure to exceed the well shut-in pressure (Figure 5.8).

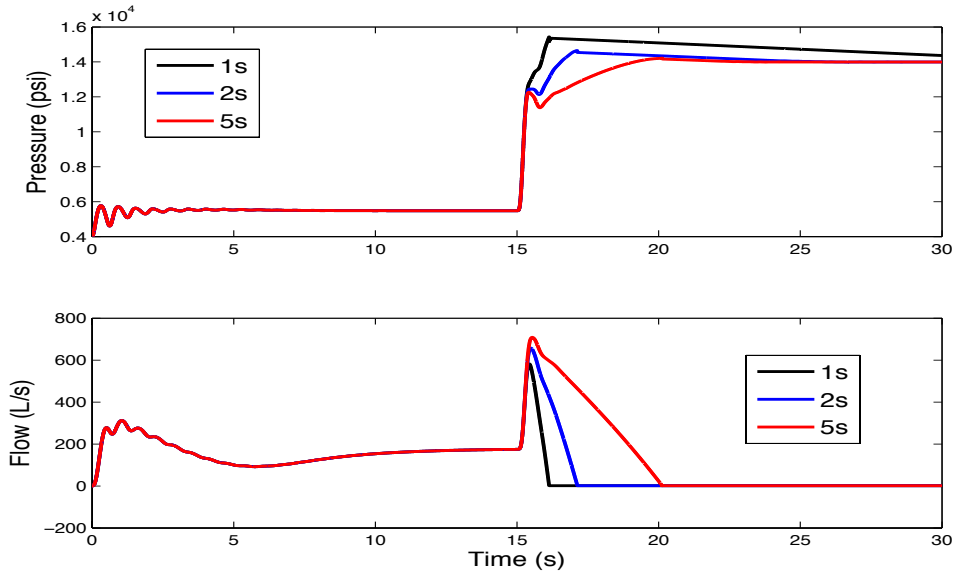

Figure 5.8: Transient Pressure and Flow Rate at the HIPPS Inlet

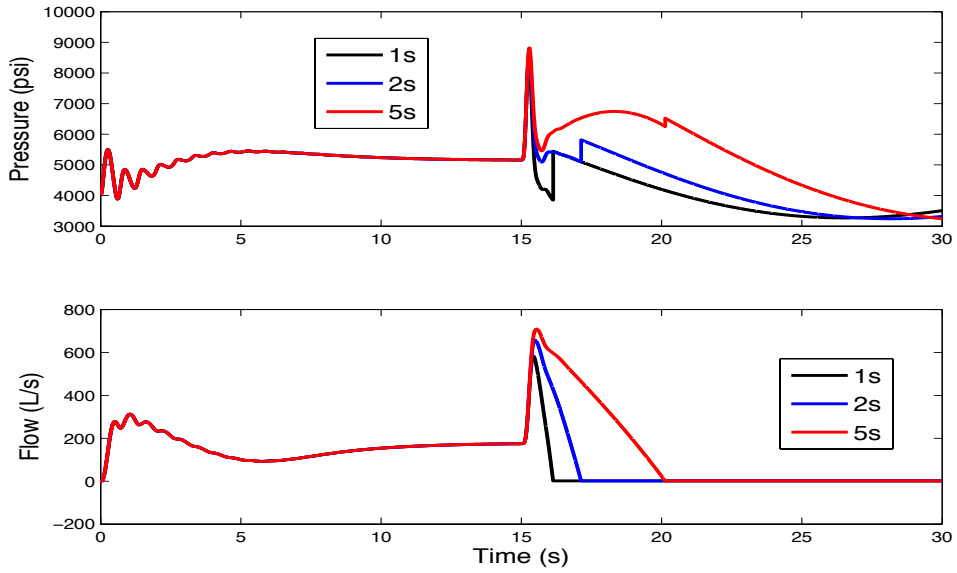

Figure 5.9: Transient Pressure and Flow Rate at the HIPPS Outlet

Figure 5.9 proves that even if the HIPPS valve was able to stop the flow rate within the different considered closing times, the pressure exceeds the design pressure of the low pressure-rated production pipeline (6,000 psi) due to the propagation of the high-pressure wave during the closure of the HIPPS valve. Hence, it is required to fortify a

section upstream of the HIPPS by rating it to the wells shut-in pressure (15,000 psi). The next step of the design process will be intended to determine the minimum required length of the fortified zone using the developed two-phase dynamic model.

Step6: Length of the Fortified Pipeline

The equivalent speed of sound, defined by (2.43) represents the speed at which a pressure wave will travel inside the pipeline. An initial value of the length of the fortified pipeline can be given by

$$L_{Fortified} = c_{eq} t_{HIPPS}, \tag{5.2}$$

where t_{HIPPS} represents the control system reaction time combined with the HIPPS valve closure time.

For the case of 0% GVF and 1s valve closing time, adopting (5.2) gives a fortified length of 958 m resulting in a conservative design of the fortified pipeline. Due to friction effects, this initial length can be decreased. Using the dynamic model established in the previous step, the length of the fortified pipeline will be decreased until reaching the design constraint.

Shown in Figure 5.10 is the pressure and flow rate transient response 609 m downstream of the HIPPS valve.

It is noticed that this length is sufficient to contain the pressure surge at the outlet of the HIPPS. The same procedure is repeated for GVF between 0 and 50% and valve closing time between 1 and 5s (Figure 5.11). It is confirmed by Figure 5.11 that the use of a fast acting HIPPS valve will result in shorter length for the fortified zone as demonstrated by (5.2). Furthermore, it can be noticed that higher GVF levels in the wells

will result also in shorter fortified length. This can be explained by the fact that increasing the amount of gas in the pipelines will result in a lower density and bulk modulus. However, the speed of sound is more sensitive to the bulk modulus due to the use of the parallel combination of the liquid and gas bulk moduli (2.41), leading to a lower speed of sound characterizing the equivalent fluid.

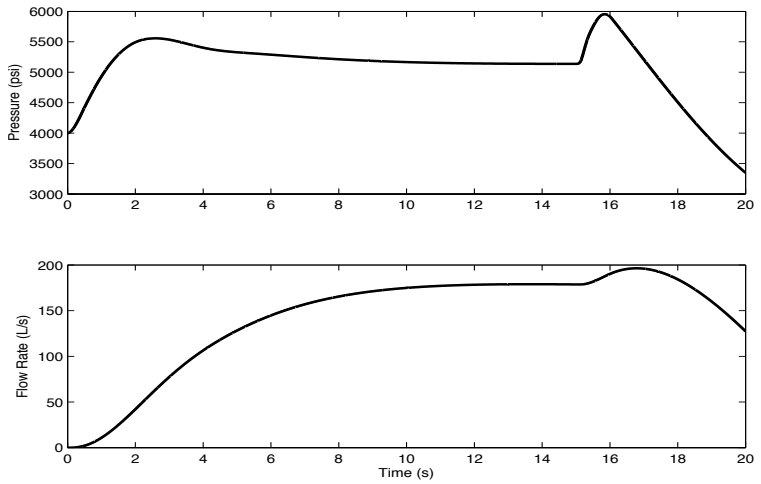

Figure 5.10: Transient Pressure and Flow Rate at the Outlet of the Fortified Pipeline

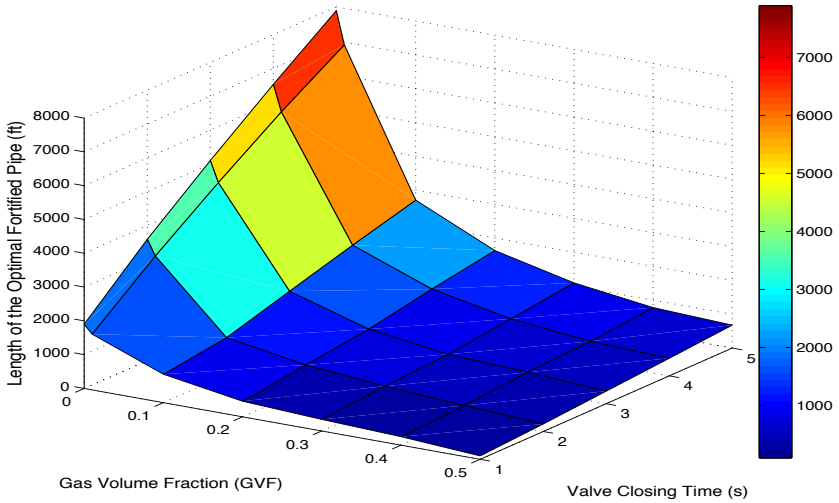

Figure 5.11: Optimal Length of the Fortified Pipeline

Step 6: Cost Analysis

The costs of the different pipelines are calculated as

$$C = f_s f_P C_0 L + C_{mis}, \tag{5.2}$$

where f_s is the size factor; f_P is the pressure rating facto; C_0 is the basic cost per unit length; L is the pipeline length; and C_{mis} are miscellaneous costs associated with the pipeline.

The different parameters are tabulated in [64]. Based on (5.2), if all the pipelines were to be designed to withstand the wells shut-in pressure, the total cost of the pipelines would be equal to 31.94 million USD. Given in Figure 5.12 is the percentage of saving in the pipelines cost with the use of the HIPPS with low-pressure rated pipelines for different GVF levels and valve closing times.

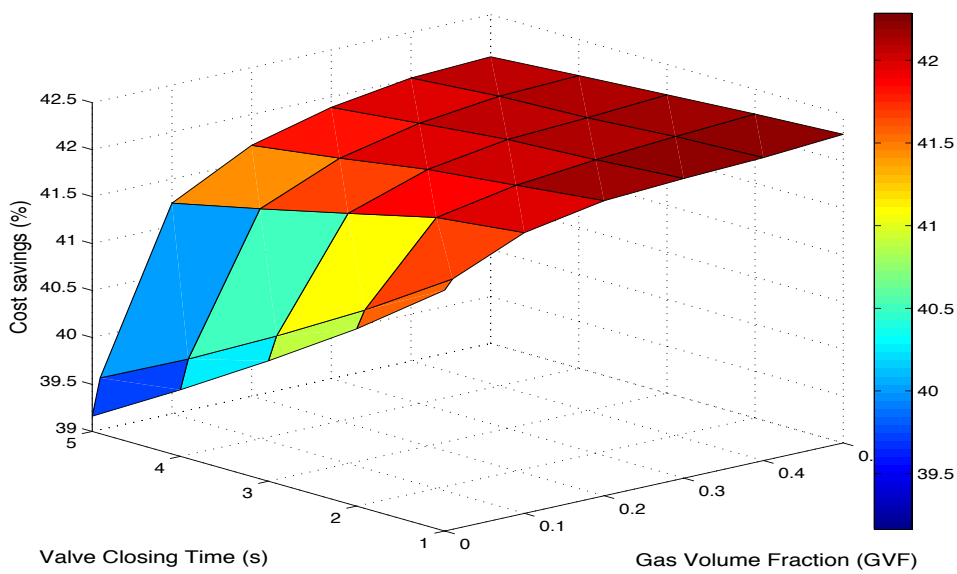

Figure 5.12: Cost Savings Associated with HIPPS Installation

Figure 5.12 demonstrates that the installation of HIPPS will results in savings between 12.5 and 13.5 million USD representing between 39 and 42% of the total pipelines procurement cost. Those savings can be more important if a dual production pipeline is used downstream of the HIPPS.

To further reduce the subsea project CAPEX, the effect of the subsea manifold location is studied to minimize the total flowlines cost using a subsea HIPPS associated with low-rated pipelines downstream of its location. The same four-well subsea architecture described in Step 1 is considered. Shown in Figure 5.13 are the wells and the possible manifold locations.

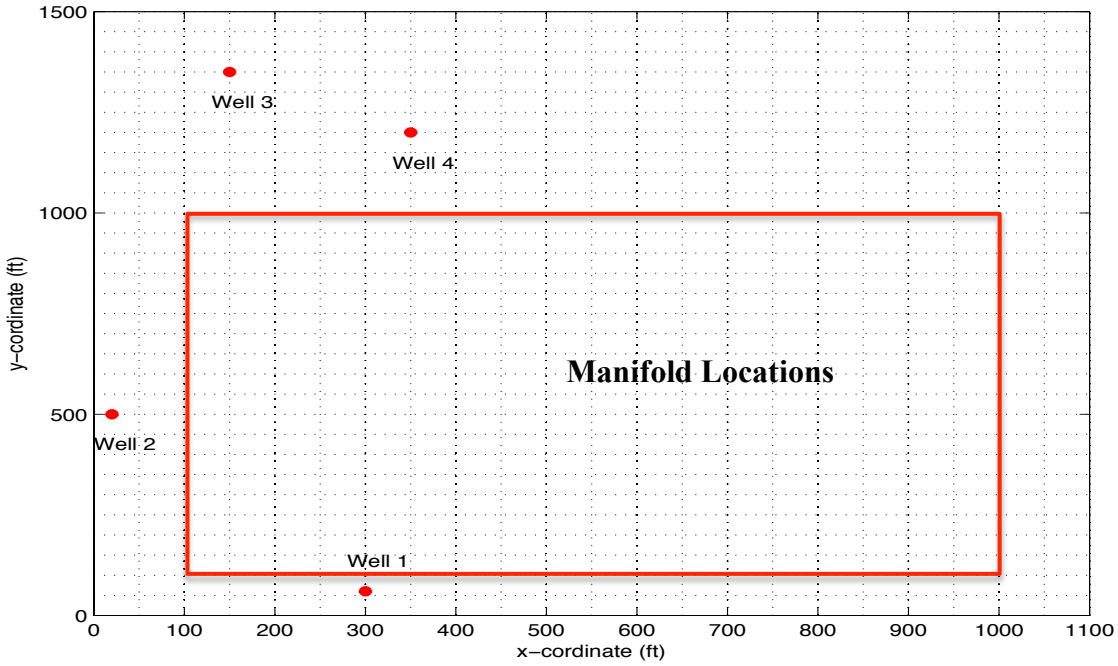

Figure 5.13: Wells and Manifold Locations

Shown in Figure 5.14 is the pipelines cost calculated following (5.2) for different possible manifold locations for a 30% GVF level and 1s HIPPS valve closing time.

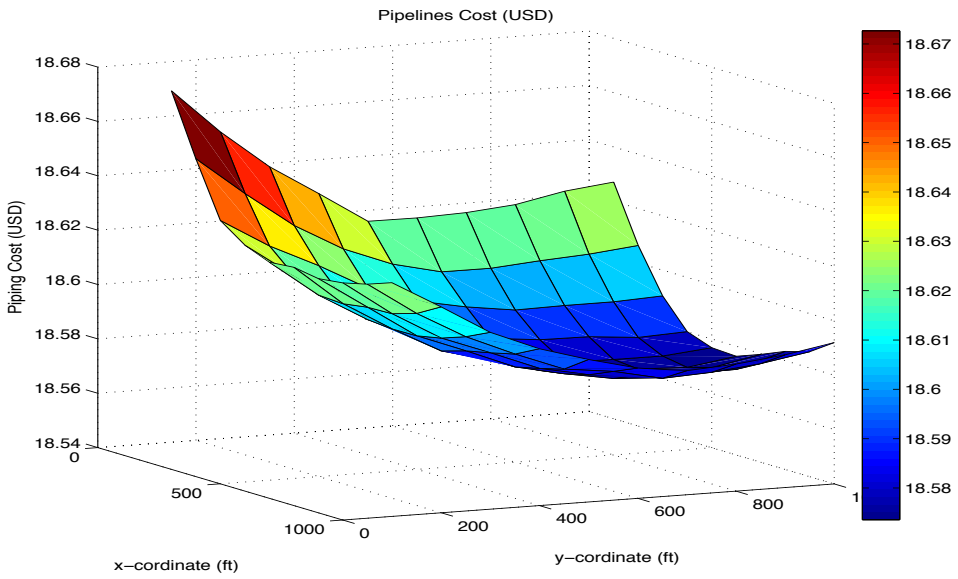

Figure 5.14: Flowlines Cost for Different Manifold Locations

Presented in Figure 5.15 is the optimal manifold location minimizing the total pipelines cost.

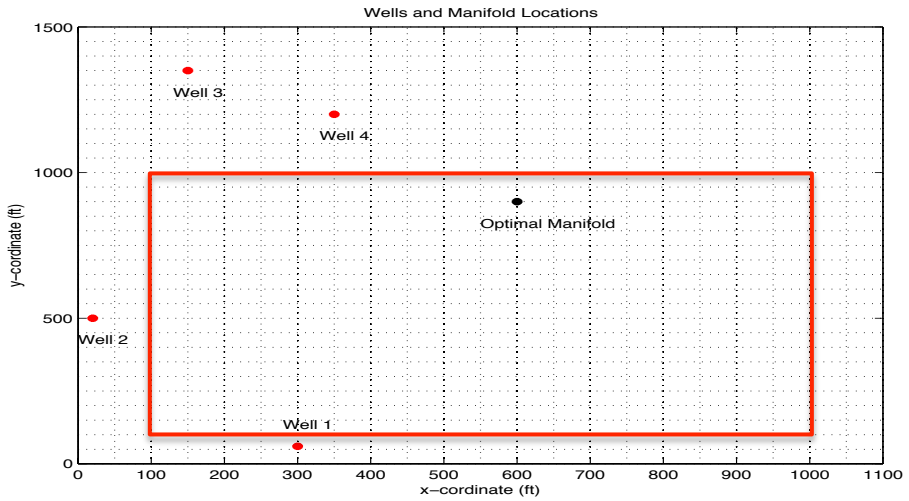

Figure 5.15: Optimal Manifold Location

5.6. Conclusion

In this chapter, the multi-physics two-phase flow models presented in Chapter 2 and 3 are used in a systems approach for the design, simulation and optimization of subsea architecture with a High Integrity Pressure Protection System. It has been demonstrated that the installation of HIPPS associated with the optimal length of the fortified zone and the optimal manifold location can result in significant savings in the subsea project CAPEX (around 40%).

The developed subsea HIPPS design procedure will help evaluating the performance of the current installed subsea HIPPS and can be used as a guideline of the feasibility study of the installation of HIPPS in a new subsea project.

Chapter 6

Conclusions and Future Work

6.1. Conclusions

Aiming at providing a systems approach platform for subsea engineering design, multi-domain hydraulic and thermal reduced order models for transient two-phase flow in pipelines are proposed in this dissertation. The developed models are not computationally expensive and provide a quasi-instantaneous result. The ability of delivering quick results can make a big difference in the oil and gas industry, where real-time monitoring of pressure and flow is of high interest.

The two-phase flow transient low-dimensional fluid model, presented in Chapter 2, is based on a three-steps process. First, a mechanistic steady-state model is implemented to determine the two-phase flow pattern, liquid holdup and pressure drop. These estimates are used to derive an equivalent single-phase fluid, which is fed to a modal approximation of the dissipative distributed-parameter model. The mechanistic steady-state two-phase flow model used in this development is validated using the Stanford University Oil & Gas Database for multiphase flow. This database contains pressure gradient, liquid holdup and flow pattern observations for a wide range of liquid and gas flow rates, fluid properties, and pipe characteristics. Given that the predicted steady-state pressure drop and liquid holdup directly intervene in the equivalent single-phase fluid, which considerably affects the model response, any new more reliable steady-state model can be easily incorporated, without affecting the low-D model structure.

To capture the interdependence between heat transfer and fluid flow, the low-D fluid model is integrated with a two-phase flow thermal model using a multiphysics integration block that estimates the fluid properties as a function of the pressure and temperature conditions. This approach enables a more accurate evaluation of the liquid and gas properties distribution along the pipeline and therefore a better prediction of the equivalent fluid parameters. A major advantage of this integrated model over existing commercial multiphase flow packages is that it offers a physics-based tool to estimate the pipeline liquid holdup and the two-phase pressure and temperature conditions. Therefore, they directly translate into models having utility in flow assurance applications.

The pressure predictions of the derived multi-physics two-phase flow model are compared to OLGA simulations for different Gas Volume Fraction (GVF) levels. The two models show a similar estimation of the steady-state pressure drop and the system natural frequency but are characterized with a different damping ratio. To further assess the developed model accuracy, experimental tests were conducted at the National University of Singapore multiphase flow loop. It has been demonstrated that the more modes are considered in the approximation of the dissipative distributed parameter model, the more dynamic is the response, and the closer to the reality are the transients. As this improved accuracy comes with an additional required computational power, recommendations on the appropriate selection of the model order are made depending on the desired application. Furthermore, the experimental results associated with the low-D model and OLGA estimations confirm the presence of entrained air at the test facility, leading to longer and more damped pressure oscillations. A comparison to the measured

transient pressure for different GVF levels confirmed a better overall performance of the developed model over the OLGA software.

In order to demonstrate its utility in modeling complex systems, the proposed two-phase flow transient model is used to design, simulate and optimize a multiple-well subsea architecture. The installation of a High Integrity Pressure Protection System (HIPPS) is also suggested as a mean to considerably reduce the subsea architecture capital expenditures.

6.2. Future Work

This dissertation presents physics-based low-dimensional fluid and thermal models for transient two-phase flow in pipelines as an alternative to multiphase flow commercial packages. A multitude of possible extensions can emerge from this work aiming at refining the proposed models, evaluate their accuracy and broaden their area of application.

Hydrodynamic slug flow is one of the most commonly observed flow patterns in the subsea oil and gas production. The developed low-D two-phase flow model accounts for the effect of the slug flow conditions on the average flow, pressure and temperature seen along the pipeline. In reality, under this type of flow, the transient pressure and flow is characterized by higher frequency oscillations due to the succession of liquid slugs and Tailor bubbles. This phenomenon can induce a cyclic fatigue in the jumpers, pipelines and riser thus affecting the subsea structure integrity. The hydrodynamic slug modeling can be integrated to the proposed low-D model by scheduling between the dispersed bubble flow (liquid slug) and the annular mist or stratified flow (Tailor bubble) based on their respective length and propagation velocity. The model user can disable this

additional module if only the average properties are of interest. The addition of the hydrodynamic slugging module will enable the study of slug catchers sizing and slugging mitigation using active feedback control of the topside valve or the choke at the subsea Christmas tree.

The transient experimental data, collected at the National University of Singapore flow loop, were limited to the case of air-water mixtures. Performing tests using air, water and oil mixtures will enable a more detailed evaluation of the developed model accuracy and ability to capture the effect of the fluid properties variation on the pipeline dynamic response. Furthermore, those additional test will help assess if the proposed modeling procedure can be extended to the case of three phase flow mixtures. The transient datasets presented in this dissertation were also collected at constant temperature conditions. To account for transient heat transfer effects, the fluids can be heated before being supplied to the test section by the air compressor and the water pump for different GVF levels. The air and water flow supply is then stopped to study the pipeline cool-down phenomena. The flow rate, pressure and temperature measurements are then compared to the multi-physics model predictions and OLGA simulations.

Once the transient thermal part validated, the proposed model can be coupled with the hydrate formation or wax deposition characteristic curves to determine if the pipeline is subject to a partial or complete blockage. The same multi-physics model can be used to identify the effective strategy to mitigate the risk of flow obstruction either by chemicals injection to move the effective fluid properties out of the hydrate or wax deposition region or by the design of the pipeline insulation necessary to reduce the heat loss to the subsea environment.

Although the two-phase flow models presented in this dissertation were limited to the case of Newtonian fluids, commonly observed during the oil and gas production phase, the same modeling procedure can easily be extended to the case of non-Newtonian fluids by the introduction of the concept of apparent viscosity for the case of power law fluids or Bingham plastics. The non-Newtonian fluids are most commonly observed in the drilling phase. They are always associated with particles or cuttings transport. The presence of a solid phase adds an extra layer of complexity to the multiphase flow modeling process, as the particle shape and gel strength can affect considerably the drilling fluid carrying capacity. The derivation of a reliable non-Newtonian multiphase flow model has a significant utility in the simulation and optimization of the drilling operations.

Thanks to the low-dimensional and reduced-order nature of the developed physics-based two-phase flow transient models, they can be used for different condition-based and health monitoring applications. For instance, the presence of a leak in the pipeline results in a higher equivalent viscosity due to the additional pressure loss and a lower speed of sound due to the increase in the fluid apparent compressibility. By dividing the pipeline into segments and identifying the equivalent fluid properties variations, the leak can be located and quantified.

Finally, the two-phase flow low-D models used in this dissertation for subsea engineering applications can be extended for the study of some of the downstream equipment characterized by a similar transient behavior such as flowlines, pumps and accumulators.

References

[1] F. Domine and P. B. Shepson, "Air-Snow Interactions and Atmospheric Chemistry," *Science,* vol. 297, pp. 1506-10, Aug 30 2002.

[2] Y. Jung, E. C. Wong, and T. T. Liu, "Multiphase Pseudocontinuous Arterial Spin Labeling (Mp-Pcasl) for Robust Quantification of Cerebral Blood Flow," *Magn Reson Med,* vol. 64, pp. 799-810, Sep 2010.

[3] B. Das, G. Enden, and A. S. Popel, "Stratified Multiphase Model for Blood Flow in a Venular Bifurcation," *Ann Biomed Eng,* vol. 25, pp. 135-53, Jan-Feb 1997.

[4] W. G. Lindsley, W. P. King, R. E. Thewlis, J. S. Reynolds, K. Panday, G. Cao*, et al.*, "Dispersion and Exposure to a Cough-generated Aerosol in a Simulated Medical Examination Room," *J Occup Environ Hyg,* vol. 9, pp. 681-90, 2012.

[5] C. X. Zhao, "Multiphase Flow Microfluidics for the Production of Single or Multiple Emulsions for Drug Delivery," *Adv Drug Deliv Rev,* vol. 65, pp. 1420-46, Nov 2013.

[6] B. P. Van Poppel, O. Desjardins, and J. W. Daily, "A Ghost Fluid, Level Set Methodology for Simulating Multiphase Electrohydrodynamic Flows with Application to Liquid Fuel Injection," *Journal of Computational Physics* vol. 229, pp. 7977-7996, 2010.

[7] G. C. Cheng and F. Richard, "Real Fluid Modeling Oof Multiphase Flows in Liquid Rocket Engine Combustors," *Journal of propulsion and power,* vol. 22, pp. 1373-1381, 2006.

[8] D. Dos Santos and S. Santana, "Determination of Mo and V in Multiphase Gasoline Emulsions by Electrothermal Atomic Absorption Spectrometry," *Spectrochimica Acta Part B: Atomic Spectroscopy,* vol. 61, pp. 592-595, 2006.

[9] J. B. Young, "Two-Dimensional, Nonequilibrium, Wet-Steam Calculations for Nozzles and Turbine Cascades," *ASME J. Turbomach* vol. 114, pp. 569-579, 1992.

[10] B. J. Dikken, "Pressure Drop in Horizontal Wells and its Effect on Production Performance," *Journal of Petroleum Technology* vol. 42, pp. 1-426, 1990.

[11] S. Sundaresan, "Modeling the Hydrodynamics of Multiphase Flow Reactors: Current Status and Challenges."

[12] T. Young, "Propagation of Impulse Through an Elastic Tube," presented at the Trans. Royal Society of London, 1808.

[13] D. J. Korteweg, "Uber die Fortpflanzungsgeschwindigkeit des Schallesin Elastisches Rohren," *Annalen der Physikund Chemie,* vol. 9, pp. 525-542, 1878.

[14] H. Lamb, "On the Velocity of Sound in a Tube, as Affected by the Elasticity of the Walls," in *Manchester Literary and Philosophical Soc, Memoirs and Proc*, 1898.

[15] A. K. Trikha, "An Efficient Method for Simulating Frequency-Dependent Friction in Transient Liquid Flow," *Trans. ASME Journal of Fluids Engineering, Series I,* vol. 97, p. 97-105, 1975.

[16] A. S. Iberall, "Attenuation of Oscillatory Pressures in Instrument Lines," *J. Res. Nat. Bur. Stand,* vol. 45, p. 85, 1950.

[17] F. T. Brown, "The Transient Response of Fluid Lines," *Journal of Basic Engineering, ASME Transactions, Series D,* vol. 84, pp. 547-553, 1962.

[18] R. E. Oldenburger and R. E. Goodson, "Simplification of Hydraulic Line Dynamics by Use of Infinite Products," *ASME J. Basic Eng. ,* vol. 86, pp. 1-8, 1964.

[19] C. Y. Hsue and D. A. Hullender, "Modal Approximations for the Fluid Dynamics of Hydraulic and Pneumatic Transmission Lines," presented at the Fluid Transmission Lines Dynamics, ASME Special Publication, New York, 1983.

[20] P. K. Bansal and A. S. Rupasinghe, "A Homogeneous Model for Adiabatic Capillary Tubes," *Applied Thermal Engineering,* pp. 207-219, 1998.

[21] R. G. Owen, J. C. R. Hunt, and J. G. Collier, "Magnetohydrodynamic Pressure Drop In Ducted Two- Phase Flows," *International Journal of Multiphase Flow,* pp. 23-33, 1976.

[22] J. J. Ginoux, *Two-phase Flows and Heat Transfer with Application to Nuclear Reactor Design Problems*. Washington: Hemisphere Publishing Co, 178.

[23] A. Faghri and Y. Zhang, *Transport Phenomena in Multiphase Systems*. Burlington, MA: Elsevier, 2006.

[24] M. M. Awad and Y. S. Muzychka, "Effective Property Models for Homogeneous Two-Phase Flows," *Experimental Thermal and Fluid Science,* pp. 106-113, 2008.

[25] R. C. Martinelli and D. B. Nelson, "Prediction of Pressure Drop during Forced Circulation Boiling of Water," *Trans. Amer. Soc. Mech. Engrs.,* pp. 695-702, 1948.

[26] R. W. Lockhart and R. C. Martinelli, "Proposed correlation of data for isothermal two-phase, two-component flow in pipes," *Chemical Engineering Progress,* vol. 45, pp. 39-45, 01// 1949.

[27] A. Gopalakrishman and V. E. Schrock, *Void Fraction from the Energy Equation*. Stanford, CA: Palo Alto : Heat Transfer and Fluid Mechanics Institute, Stanford University Press, 1964.

[28] A. Premoli, D. Francesco, and A. Prima, "An Empirical Correlation for Evaluating Two-Phase Mixture Density under Adiabatic Conditions," in *Proc. European Two-Phase Flow Meeting*, 1970.

[29] L. Friedel, "Improved Friction Pressure Drop Correlations for Horizontal and Vertical Two-Phase Flow," *3R Int.,* pp. 485-491, 1979.

[30] S. Levy, "Steam Slip-Theoretical Prediction from Momentum Model," *Trans. ASME, J. Heat Transfer,* pp. 113-124, 1980.

[31] H. J. Richter and S. E. Minas, "Separated Flow Model for Critical Two-Phase Flow," *Nonequilibrium Interfacial Transport Processes, ASME (Nonequilibrium Interfacial Transport Processes, ASME),* 1979.

[32] H. J. Richter, "Separated Two-Phase Flow Model: Application to Critical Two-Phase Flow," *International Journal of Multiphase Flow,* pp. 511-530, 1983.

[33] S. Wongwises, P. Chan, N. Luesuwanatat, and T. Purattanarak, "Two-Phase Separated Flow Model of Refrigerants Flowing Through Capillary Tubes," *International Communications In Heat And Mass Transfer,* pp. 343-356, 2000.

[34] M. Ishii, "Thermo-Fluid Dynamic Theory of Two-Phase Flow," *Eyrolles,* 1975.

[35] T. Saito, E. D. Hughes, and M. W. Carbon, "Multi-Fluid Modeling of Annular Two-Phase Flow," *Nuclear Engineering and Design,* pp. 225-271, 1978.

[36] J. A. Bouré and J. M. Delhaye, *General Equations and Two-Phase Flow Modeling*. New York: Hemisphere-McGraw-Hill, 1986.

[37] J. A. Bouré, "Two-Phase Flow Models: The Closure Issue," presented at the European Two-Phase Flow Group, Munich, 1986.

[38] V. Stevanovic, S. Prica, and B. Maslovaric, "Multi-Fluid Model Predictions of Gas-Liquid Two- Phase Flows in Vertical Tubes," *FME Transactions,* pp. 173-181, 2007.

[39] N. Zuber and J. A. Findlay, "Average Volumetric Concentration in Two-Phase Flow Systems," *J. Heat Mass Transfer,* pp. 453-468, 1965.

[40] M. Ishii, *One-Dimensional Drift-Flux Model and Constitutive Equations for Relative Motion Between Phases in Various Two-Phase Flow Regimes*: ANL-77-47, 1977.

[41] G. B. Wallis, *One-Dimensional Two-Phase Flow. 2nd Edition.* New York: McGraw Hill, 1979.

[42] B. Chexal and G. Lellouche, "Void Fraction Correlation for Generalized Applications," *Progress in Nuclear Energy,* pp. 255-295, 1992.

[43] P. Coddington and R. Macian, "A Study of the Performance of Void Fraction Correlations used in the Context of Drift-Flux Two-Phase Flow Models," *Nuclear Engineering and Design,* pp. 199-216, 2002.

[44] J. Choi, E. Pereyra, C. Sarica, C. Park, and J. M. Kang, "An Efficient Drift-Flux Closure Relationship to Estimate Liquid Holdups of Gas-Liquid Two-Phase Flow in Pipes," *Energies,* pp. 5294-5306, 2012.

[45] Y. Taitel and A. E. Dukler, "A model for predicting flow regime transitions in horizontal and near horizontal gas-liquid flow," *AIChE Journal,* vol. 22, pp. 47-55, 1976.

[46] D. Barnea, "A Unified Model for Predicting Flow Pattern Transitions for the Whole Range of Pipe Inclinations," *Int. J. Multiphase Flow,* pp. 1-12, 1978.

[47] J. J. Xiao, O. Shoham, and J. P. Brill, "A Comprehensive Mechanistic Model for Two-Phase Flow in Pipelines," presented at the SPE 2063 1, 65th ATC&E of SPE, New Orleans, 1990.

[48] A. M. Ansari, N. D. Sylvester, C. Sarica, O. Shoham, and J. P. Brill, "A Comprehensive Mechanistic Model for Upward Two-Phase Flow in Wellbores," pp. 143-152, 1994/5/1/ 1994.

[49] N. Petalas and K. Aziz, "A Mechanistic Model for Multiphase Flow in Pipes," Calgary, Alberta, 1998.

[50] N. Petalas and K. and Aziz, "A Mechanistic Model for Multiphase Flow in Pipes," *Journal of Canadian Petroleum Technology,* pp. 43-55, 2000.

[51] K. V. Moore and W. H. Rettig, "RELAP4—A Computer Program for Transient Thermal-Hydraulic Analysis," N. R. T. S. Aerojet Nuclear Company, Ed., ed, 1973.

[52] S. R. Fischer, "Use of Vertical Slip and Flooding Models in LOCA Analysis," *Transactions of the American Nuclear Society,* p. 334, 1975.

[53] R. W. Lyczkowski, D. Gidaspow, C. W. Solbrig, and E. D. Hughes, "Characteristics and Stability Analyses of Transient One-Dimensional Two-Phase Flow Equations and Their Finite Difference Equations," presented at the ASME Winter Annual Meeting, 1975.

[54] C. W. Solbrig and E. D. Hughes, "Governing Equations for a Seriated Continuum: An Unequal Velocity Model for Two-Phase Flow," N. R. T. S. Aerojet Nuclear Company, Ed., ed, 1975.

[55] R. S. Cunliffe, "Prediction of Condensate Flow Rates in Large Diameter High Pressure Wet Gas Pipelines," *APEA Journal,* pp. 171-177, 1978.

[56] L. Modisette and R. S. Whaley, "Transient Two-Phase Flow," presented at the PSIG Annual Meeting, Detroit, 1883.

[57] K. Bendiksen, I. Brandt, P. Fuchs, H. Linga, D. Malnes, and R. Moe, "Two-Phase Flow Research at SINTEF and IFE: Some Experimental Results and a Demonstration of the Dynamic Two- Phase Flow Simulator OLGA," presented at the Offshore Northern Seas Conference, Stavanger, Norway, 1986.

[58] K. Bendiksen, I. Brandt, K. A. Jacobsen, and C. Pauchon, "Dynamic Simulation of Multiphase Transportation Systems," presented at the Multiphase Technology and Consequences for Field Development Forum, Stavanger, Norway, 1987.

[59] K. Bendiksen, D. Malnes, R. Moe, and S. Nuland, "The Dynamic Two-Fluid Model OLGA: Theory and Application," *SPE Production Engineering,* pp. 171-180, 1991.

[60] P. S. Black, L. C. Daniels, N. C. Hoyle, and W. P. Jepson, "Studying Transient Multiphase Flow using the Pipeline Analysis Code (PLAC)," *Journal of Energy Resources Technology,* pp. 25-29, 1990.

[61] C. Pauchon, H. Dhulesia, G. Binh-Cirlot, and J. Fabre, "TACITE: A transient Tool for Multiphase Pipeline and Well Simulation," presented at the SPE Annual Technical Conference, New Orleans, 1994.

[62] Y. Taitel, S. Ovadia, and J. P. Brill, "Simplified Transient Solution and Simulation of Two-Phase Flow in Pipelines," *Chemical Engineering Science,* pp. 353-359, 1989.

[63] O. Shoham, *Mechanistic modeling of gas-liquid two-phase flow in pipes*: Richardson, TX : Society of Petroleum Engineers, c2006., 2006.

[64] Q. Bai and Y. Bai, *Subsea Engineering Handbook*. Houston: Elsevier, 2010.

[65] F. M. Wood, "The Application of Heaviside's Operational Calculus to the Solution of Problems in Water Hammer," *TBANS. ASME,* pp. 707-713, 1937.

[66] J. T. Karam and M. E. Franke, "The Frequency Response of Pneumatic Lines," *ASME Journal of Basic Engineering,* pp. 371-378, 1967.

[67] M. E. Franke, A. J. Malanowski, and P. S. Martin, "Effects of Temperature, End Conditions, Flow and Branching on the Frequency Response of Pneumatic Lines," *ASME Journal of Dynamic Systems, Measurement, and Control,* pp. 15-20, 1972.

[68] V. K. Ravindran and J. R. Manning, "The Frequency Response of Pneumatic Lines with Branching," *ASME Journal of Dynamic Systems, Measurement, and Control,* pp. 194-196, 1973.

[69] D. N. Johnston, "Numerical Modelling of Unsteady Turbulent Flow in Tubes, Including the Effects of Roughness and Large Changes in Reynolds Number," *Proceedings of the Institution of Mechanical Engineers, Part C: Journal of Mechanical Engineering Science,* pp. 1874-1885, 2011.

[70] O. Bratland, *Pipe Flow 2: Multi-phase Flow Assurance*, 2010.

[71] C. F. Colebrook, "Turbulent Flow in Pipes, with Particular Reference to the Transition Region between Smooth and Rough Pipe Laws," *Journal of the Institution of Civil Engineers,* 1939.

[72] L. F. Moody, "Friction Factors for Pipe Flow," *Transactions of the ASME,* pp. 671–684, 1944.

[73] C. T. Goudar and J. R. Sonnad, "Comparison of the Iterative Approximations of the Colebrook–White Equation," Hydrocarbon Processing Fluid Flow and Rotating Equipment 2008.

[74] Z. Schmidt, J. P. Brill, and H. D. Beggs, "Experimental Study of Severe Slugging in a Two-Phase-Flow Pipeline - Riser Pipe System," 1980/10/1/ 1980.

[75] J. Colligan, "The Economics of Deep Water," ed: Society of Petroleum Engineers, 1999.

[76] M. T. Rubel and D. H. Broussard, "Flowline Insulation Thermal Requirements for Deepwater Subsea Pipelines."

[77] R. Tafreshi, Z. Khan, M. Franchek, and K. Grigoriadis, "Two-Phase Heat Transfer Modeling in Subsea Pipelines," in *Integrated Systems: Innovations and Applications*, M. Fathi, Ed., ed: Springer International Publishing, 2015, pp. 243-256.

[78] M. Mohammadzaheri, Z. Khan, R. Tafreshi, M. Francheck, and K. Grigoriadis, "Modelling of Petroleum Multiphase Fluids in ESPs: An Intelligent Approach," in *Offshore Mediterranean Conference*, ed. Ravenna, Italy, 2015.

[79] M. Mohammadzaheri, R. Tafreshi, Z. Khan, M. Francheck, and K. Grigoriadis, "An Intelligent Approach to Optimize Multiphase Subsea Oil Fields Lifted by Electrical Submersible Pumps," *Journal of Computational Science* 2015.

[80] K. S. Rezkallah, and Sims, G. E, "Examination of Correlations of Mean Heat Transfer Coefficients in Two-Phase Two-Component Flow in Vertical Tubes," *AIChE Symposium Series,* vol. 83, pp. 140-151, 1987.

[81] M. A. Aggour, "Hydrodynamics and Heat Transfer in Two-Phase Two-Component Flow," PhD, University of Manitoba, Winepeg, Canada, 1978.

[82] W. R. Dorresteijn, "Experimental Study of Heat Transfer in Upward and Downward Two-Phase Flow of Air and Oil through 70 mm Tubes," in *4th International Heat Transfer Conference*, 1970, pp. 1-10.

[83] C. D. G. King, "Heat Transfer and PressureDrop for an Air Water Mixture Flowing in a 0.737 Inch I.D. Horizontal Tube. ," M.S University of California, Berkeley, CA, 1952.

[84] M. M. Shah, "Generlized Prediction of Heat Transfer during Two Component Gas-Liquid Flow in Tubes and Other Channels," in *AIChE Symposium* 1981, pp. 140-151.

[85] R. F. Knott, R. N. Anderson, A. Acrivos, and E. E. Petersen, "An Experimental Study of Heat Transfer to Nitrogen-Oil Mixtures," *Industrial & Engineering Chemistry,* vol. 51, pp. 1369-1372, 1959/11/01 1959.

[86] W. T. Duesseau, "Overall Heat Transfer Coefficeint of Air Water Froth in a Vertical Pipe," M.S, Chemical Engineering, Vanderbilt University, Nashville, TN, 1968.

[87] G. Elamvaluthi and N. S. Srinivas, "Two-Phase Heat Transfer in Two-Component Vertical Flows," *International Journal of Multipahse Flow,* vol. 10, pp. 237-242, 1984.

[88] D. Kim, A. J. Ghajar, R. L. Dougherty, and V. K. and Ryali, "Comparison of 20 Two-Phase Heat Transfer Correlations With Seven Sets of Experimental Data, Including Flow Pattern and Tube Inclination Effects," *Heat Transfer Engineering,* vol. 20, pp. 15-40, 1999.

[89] C. Tang and A. Ghajar, "A Mechanistic Heat Transfer Correlation for Non-boiling Two-phase Flow in Horizontal, Inclined and Vertical Pipes," in *8th Thermal Engineering Joint Conference*, Honolulu, 2011.

[90] R. D. Kaminsky, "Estimation of Two-Phase Flow Heat Transfer in Pipes," *Journal of Energy Resources Technology,* vol. 121, pp. 75-80, 1999.

[91] M. M. Vijay, M. A. Aggour, and G. E. Sims, "A Correlation of Mean Heat Transfer Coefficients for Two-Phase Two-Component Flow in a Vertical Tube," in *7th Internaltional Heat Transfer Conference*, 1982, pp. 367-372.

[92] F. P. Incropera, D. P. DeWitt, T. L. Bergman, and A. S. Lavine, *Fundamentals of Heat and Mass Transfer*: Wiley, 2007.

[93] E. N. Sieder and G. E. Tate, "Heat Transfer and Pressure Drop of Liquids in Tubes," *Industrial & Engineering Chemistry (1923),* vol. 28, pp. 1429-1435, 12// 1936.

[94] H. Hausen, "ng des Warneuberganges un Rohren durch verallgeineinerte Potenzbeziebungen, Darstellu," *Z Ver. Dtsch. Ing. Beiheft Verfahrenstech,* vol. 4, pp. 91-134, 1943.

[95] V. Gnielinski, "New equations for heat and mass transfer in turbulent pipe and channel flow," *Int. Chem. Eng,* vol. 19, 1975.

[96] R. D. Kaminsky, "Estimation of Two-Phase Flow Heat Transfer in Pipes," *J. Energy Resour. Technol.,* vol. 121, pp. 75-80, 1999.

[97] R. Manabe, "A Comprehensive Mechanistic Heat Transfer Model for Two-Phase Flow with High-Pressure Flow Patetrn Validation," Ph.D., University of Tulsa, Tulsa, 2001.

[98] R. Manabe, Q. Wang, H.-Q. Zhang, C. Sarica, and J. P. Brill, "A Mechanistic Heat Transfer Model for Vertical Two-Phase Flow," 2003.

[99] D. J. Nicklin, J. O. Wilkes, and J. F. Davidson, "Two-Phase Flow in Vertical Tubes," *Trans. Institut. Chem. Eng,* vol. 40, pp. 61-68, 1962.

[100] D. T. Dumitrescu, "Strömung an Einer Luftblase im Senkrechten Rohr," *ZAMM - Journal of Applied Mathematics and Mechanics,* vol. 23, pp. 139–149, 1943.

[101] K. H. Bendiksen, "An Experimental Investigation of the Motion of Long Bubbles in Inclined Tubes," *International Journal of Multiphase Flow,* vol. 10, pp. 467-483, 1984.

[102] M. M. Vijay, "A Study of Heat Transfer in Two-Phase Two-Component Flow in a Vertical Tube," PhD, Department of Mechanical Engineering, University of Manitoba, Winnepeg, Manitoba, 1977.

[103] M. Sujumnong, "Heat transfer, pressure drop and void fraction in two phase two component flow in vertical tube," Ph.D. thesis, University of Manitoba, Manitoba, 1997.

[104] D. Kim, "An Experimental and Empirical Investigation of Convective Heat Transfer for Gas-Liquid TwoPhase Flow in Vertical and Horizontal Pipes," PhD, Oklahoma State University, Oklahoma, 2000.

[105] H.-Q. Zhang, Q. Wang, C. Sarica, and J. P. Brill, "Unified Model of Heat Transfer in Gas-Liquid Pipe Flow," *SPE Production & Operations,* 2006.

[106] A. Meziou, M. Chaari, M. Franchek, K. Grigoriadis, R. Tafreshi, and B. Ebrahimi, "Subsea Production Two-phase Modeling and Control of Pipes and Manifold Assemblies," in *ASME Dynamic Systems and Control Conference*, San Antonio, 2014.

[107] A. Meziou, T. Wassar, M. Chaari, M. Franchek, and R. Tafreshi, "Model-Based Design and Analysis of a Subsea High Integrity Pressure Protection System (HIPPS)," presented at the IEEE International Conference on Advanced Intelligent Mechatronics, Banff, Alberta, Canada, 2016.

[108] Y. W. Huang, "Lumped Parameter Modeling of Fluid Line Dynamics with Turbulent Flow Conditions," PhD, Mechanical Engineering, University of Texas, Arlington, Texas, 2012.

[109] E. B. Wylie and V. L. Streeter, *Fluid Transients*. New York: McGraw-Hill International Book Co., 1978.

[110] J. A. Fox, *Hydraulic Analysis of Unsteady Flow in Pipe Networks*: Halsted Press, 1977.

[111] H. E. Merritt, *Hydraulic Control Systems*: John Wiley & Sons, 1967.

[112] P. Frafjord, S. Corneliussen, and L. A. Adriaansen, "The development of a subsea High Integrity Pipeline Protection System (HIPPS)," presented at the Offshore Technology Conference, Houston, Texas, 1995.

[113] J. Davalath, B. H. Skeels, and S. Corneliussen, "Current State of the Art in the Design of Subsea HIPPS Systems," presented at the Offshore Technology Conference, Houston, Texas, 2002.

[114] I. E. Commission, "IEC 61508 Functional Safety of Electrical/ Electronic/Programmable Electronic Safety-Related Systems," ed, 2000.

[115] I. E. Commission, "IEC 61511 Functional safety – Safety instrumented systems for the process industry sector," ed, 2003.

[116] A. P. Institute, "API RP 14C Recommended Practice for Analysis, Design, Installation, and Testing of Basic Surface Safety Systems for Offshore Production Platforms, Seventh Edition," 2001.

[117] A. P. Institute, "API RP 17O Recommended Practice for Subsea High Integrity Pressure Protection System (HIPPS), First Edition," 2009.

[118] A. P. Institute, "API 6A: Specification for Wellhead and Christmas Tree Equipment," ed, 2004.

[119] A. S. o. M. Engineers, "ASME B31. 1-Power Piping," 2007.

Appendix A

Derivation of the Characteristic Impedance and Propagation Operator

Consider the pipeline representation given in Figure A.1.

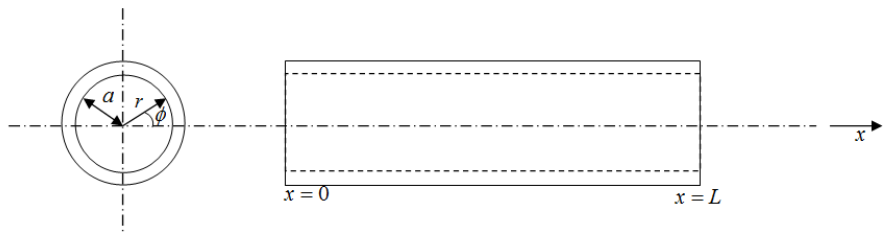

Figure A.1: Pipeline Schematic

The governing equations of the dissipative distributed parameter model are:

- Momentum equation in x-direction:

$$\rho_0\left[\frac{\partial u}{\partial t}+u\frac{\partial u}{\partial x}+v\frac{\partial u}{\partial r}\right]=-\frac{\partial p}{\partial x}+\mu\left[\frac{4}{3}\frac{\partial^2 u}{\partial x^2}+\frac{\partial^2 u}{\partial r^2}+\frac{1}{r}\frac{\partial u}{\partial r}+\frac{1}{3}\frac{\partial}{\partial x}\left(\frac{\partial v}{\partial r}+\frac{v}{r}\right)\right], \tag{A.1}$$

- Continuity equation:

$$\frac{\partial \rho}{\partial t}+\rho_0\left(\nabla.\vec{u}\right)=0\,, \tag{A.2}$$

- Energy equation:

$$\frac{\partial T}{\partial t}+T_0\left(\gamma-1\right)\left(\nabla.\vec{u}\right)=\frac{\mu_0\gamma}{\sigma_0}\left[\frac{\partial^2 T}{\partial r^2}+\frac{1}{r}\frac{\partial T}{\partial r}\right],\ and \tag{A.3}$$

- Liquid and gas state equations:

$$\frac{d\rho}{\rho} = \frac{dp}{\kappa} \ \ and \tag{A.4}$$

$$\frac{d\rho}{\rho} = \frac{dp}{\kappa} \, . \tag{A.5}$$

Using the assumption of long pipe and low Mach number the momentum equation in the x-direction can be written as

$$\rho_0 \frac{\partial u}{\partial t} = -\frac{\partial p}{\partial x} + \mu \left[\frac{\partial^2 u}{\partial r^2} + \frac{1}{r}\frac{\partial u}{\partial r} \right] . \tag{A.6}$$

The average velocity in the *x*-direction and pressure across the pipe cross-section are

$$\pi a^2 \overline{p}(x,t) = \int_0^a 2\pi r p(x,t) dr = \pi a^2 p(x,t) \ \ and \tag{A.7}$$

$$\pi a^2 \overline{u}(x,r,t) = \int_0^a 2\pi r u(x,r,t) dr \, . \tag{A.8}$$

The Laplace transforms of those variables are

$$\overline{P}(x,s) = L\left[\overline{p}(x,t)\right] \ \ and \tag{A.9}$$

$$U(x,r,s) = L\left[\overline{u}(x,r,t)\right] . \tag{A.10}$$

Using (A.6), (A.9) and (A.10) the Laplace transform of the momentum equation is written as

$$\frac{\partial^2 U}{\partial r^2} + \frac{1}{r}\frac{\partial U}{\partial r} - \frac{s}{\nu_0}\left[U + \frac{1}{\rho_0 s}\frac{\partial \overline{P}}{\partial x}\right] = 0 \ . \tag{A.11}$$

The following change of variable is used

$$V = U + \frac{1}{\rho_0 s}\frac{\partial \overline{P}}{\partial x} \ . \tag{A.12}$$

Hence, equation (A.11) becomes

$$\frac{\partial^2 V}{\partial r^2} + \frac{1}{r}\frac{\partial V}{\partial r} - \frac{s}{\nu_0} V = 0. \tag{A.13}$$

The solution of equation (A.13) is of the form

$$V = f(x,s)\left\{J_0\left[jr\left(\frac{s}{\nu_0}\right)^{\frac{1}{2}}\right]\right\}, \tag{A.14}$$

where *J0* is the zero order Bessel Function of first kind.

The Laplace transform of the liquid velocity is then given by

$$U = f(x,s)\left\{J_0\left[jr\left(\frac{s}{\nu_0}\right)^{\frac{1}{2}}\right]\right\} - \frac{1}{\rho_0 s}\frac{\partial \overline{P}}{\partial x} \ . \tag{A.15}$$

Using the boundary condition at the pipe internal wall

$$U\big|_{r=a} = 0\,, \tag{A.16}$$

the Laplace transform of the liquid velocity becomes

$$U = f(x,s)\left\{J_0\left[jr\left(\frac{s}{\nu_0}\right)^{\frac{1}{2}}\right] - J_0\left[ja\left(\frac{s}{\nu_0}\right)^{\frac{1}{2}}\right]\right\}. \tag{A.17}$$

The mass flow rate is given by

$$Q_m = \frac{1}{2}2\pi\rho_0 a^2 f(x,s)\left\{\frac{2}{ja\left(\frac{s}{\nu_0}\right)^{\frac{1}{2}}}J_1\left[ja\left(\frac{s}{\nu_0}\right)^{\frac{1}{2}}\right] - J_0\left[ja\left(\frac{s}{\nu_0}\right)^{\frac{1}{2}}\right]\right\}. \tag{A.18}$$

Recalling the transmission line equation

$$Z(s)Q(x,s) = -\frac{\partial P(x,s)}{\partial x}\,, \tag{A.19}$$

the series impedance per unit length will be

$$Z(s) = \frac{\dfrac{\rho_0 s}{\pi a^2}}{1 - \dfrac{2J_1\left[ja\left(\frac{s}{\nu_0}\right)^{\frac{1}{2}}\right]}{ja\left(\frac{s}{\nu_0}\right)^{\frac{1}{2}}J_0\left[ja\left(\frac{s}{\nu_0}\right)^{\frac{1}{2}}\right]}}. \tag{A.20}$$

The Laplace transform of the energy equation is of the form

$$\frac{\partial^2\Theta}{\partial r^2}+\frac{1}{r}\frac{\partial\Theta}{\partial r}-\frac{\sigma_0}{\nu_0}s\Theta=-\frac{(\gamma-1)T_0\sigma_0}{\gamma\nu_0 p_0}sP. \tag{A.21}$$

The simplest forcing function P is

$$P=-\frac{\Theta_0\gamma p_0}{(\gamma-1)T_0}J_0\left[ja\left(\frac{\sigma_0 s}{\nu_0}\right)^{\frac{1}{2}}\right]. \tag{A.22}$$

The solution of equation (I.21) will be then

$$\Theta=\Theta_0\left[J_0\left(jr\left(\frac{\sigma_0 s}{\nu_0}\right)^{\frac{1}{2}}\right)-J_0\left(ja\left(\frac{\sigma_0 s}{\nu_0}\right)^{\frac{1}{2}}\right)\right], \tag{A.23}$$

where Θ_0 is any constant with proper unit.

The average temperature across the pipeline is

$$\bar{\Theta}=\frac{\int_0^a r\Theta\,dr}{\int_0^a r\,dr}=\Theta_0\left[J_0\left(ja\left(\frac{\sigma_0 s}{\nu_0}\right)^{\frac{1}{2}}\right)+\frac{2J_1\left(ja\left(\frac{\sigma_0 s}{\nu_0}\right)^{\frac{1}{2}}\right)}{ja\left(\frac{\sigma_0 s}{\nu_0}\right)^{\frac{1}{2}}}\right]. \tag{A.24}$$

Recalling the continuity principle of the gradient of the mass flow rate in the Laplace domain gives

$$\frac{\partial Q}{\partial x} = -\pi a^2 \left(\frac{\rho_0}{p_0} sP - \frac{\rho_0}{T_0} s\bar{\Theta} \right). \tag{A.25}$$

The shunt admittance per unit length is defined as

$$Y(s)P(x,s) = -\frac{1}{\rho_0} \frac{\partial Q_m(x,s)}{\partial x} = -\pi a^2 \left(\frac{1}{p_0} sP - \frac{1}{T_0} s\bar{\Theta} \right). \tag{A.26}$$

Simplifying (A.26) gives

$$Y(s) = \underbrace{\frac{\rho_0 \pi a^2}{p_0 \gamma}}_{C_0} s \left[1 + 2(\gamma - 1) \frac{J_1\left(ja \left(\frac{\sigma_0 s}{\nu_0} \right)^{\frac{1}{2}} \right)}{ja \left(\frac{\sigma_0 s}{\nu_0} \right)^{\frac{1}{2}} J_0 \left[ja \left(\frac{\sigma_0 s}{\nu_0} \right)^{\frac{1}{2}} \right]} \right]. \tag{A.27}$$

The characteristic impedance of the line, Z_c, and the propagation operator Γ are finally determined using

$$Z_c = \sqrt{\frac{Z}{Y}} \quad and \tag{A.28}$$

$$\Gamma = \sqrt{ZY}\ . \tag{A.29}$$

Equations (2.16) and (2.17) are then obtained.